UNIVERSITÀ DEGLI STUDI DI TORINO
Facoltà di Scienze M.F.N.
Dipartimento di Fisica Generale dell'Università di Torino

Tesi di dottorato di Ricerca in Fisica
ciclo XIX
a.a. 2003-2006

Study of semi-inclusive processes using the COMPASS spectrometer with a transversely polarized target

Candidato:
Maxim Alekseev

Tutor:
Prof. Daniele Panzieri

Contro-relatore: Prof. Philip G. Ratcliffe

Settore Scientifico-disciplinare: FIS/04

Contents

1 Outlook of the work

The work on my thesis was split in two parts. One part of the work concerns the participation in the development, testing and commissioning of the new Rich Wall detector(all the tests were performed on the prototype) and in all related areas. More precisely the areas are: electronics test, hardware itself, software for both, the reconstruction of the events and the support of the test (like data acquisition and storage), and the integration of the detector into the COMPASS experimental setup DAQ framework. This work was divided in time in three separate steps that took place during the end of the year 2004, in the summer of 2005 and in the 2006. The testing of the detector was successfully performed and then the Rich Wall detector was successfully integrated into the COMPASS experimental setup.

Another part of the work concerns the study of the Λ-hyperon polarization. The main goal is to have access to the transverse spin distribution function $\Delta_T q(x)$ exploiting the properties of the self-analyzing decay of the Λ-hyperon and the COMPASS polarized target. For that one needs to extract the polarization from the experimental data, and by making the analysis on an event by event basis, with the knowledge of the target polarization, one may extract the transverse spin distribution function $\Delta_T q(x)$. The main specifics of the analysis is that it is based on the use of the fact that the target has two separate cells, each in turn having opposite polarization orientation. This gives us the possibility to extract polarization not only without the use of the MonteCarlo simulation, but also without any assumption on the apparatus symmetries. The main difficulty arise only from the background (K^0 decays, γ conversion, wrong tracking) suppression.

Actually the background suppression is the point where the installation of the Rich Wall detector will contribute in a positive way. This detector will be the first precise tracker after the RICH(Ring Imaging CHerenkov) detector that will give the possibility to have a precise point for the "ring" reconstruction, also an additional track segment will help for a better tracking. Apart of this the Rich Wall detector will be used to distinguish between charged/neutral particles (eventually γ/e separation) and also for better shower reconstruction in the Rich Wall+ECAL1 detectors system.

Moreover, as a steel/lead convertor is installed in the RW structure, it will act as a preshower, increasing the spatial resolution of the electromagnetic calorimeter and further enhancing the separation between electromagnetic and hadronic components, that is also useful for the physical analysis.

2 INTRODUCTION

The scattering of polarized lepton beams off polarized nucleon targets has been used by several experiments, starting from 1974 up to nowadays, to probe the structure of the nucleon and to measure the partonic and gluonic contribution to the total nucleon spin. Leptons provide an extremely clean probe of the nucleon substructure, since they are transparent to the strong interaction inside the nucleon. The measurement of polarized lepton-nucleon deep-inelastic scattering (DIS) shows that the spin structure of the nucleons is much more complicated than what is described by the parton model. The parton model prediction that the nucleon spin is entirely carried by the three valence quarks is clearly contradicted by the experimental results, which show that the sea-quarks, gluons and the angular momentum contributions are significant. Independent measurement of polarized distribution functions for gluons and the different light quarks, which require semi-inclusive measurement, is of primary importance. It is now clear that a complete knowledge of the spin structure of the nucleon requires not only the helicity-averaged and helicity-dependent quark and gluon distributions, but also transverse spin distributions,which can be accessed only through two-hadron interactions or semi-inclusive hadron lepto-production. The counterpart for the helicity-dependent structure function $g_1(x)$ for transversely polarized nucleons, called transversity and denoted as $h_1(x)$, is still almost unknown, and represents one of the key measurements of the COMPASS experiment. In this chapter the introduction to the field of polarized DIS and the description of the measurement are given with an emphasis on the semi-inclusive Λ leptoproduction.

3 THE COMPASS EXPERIMENT

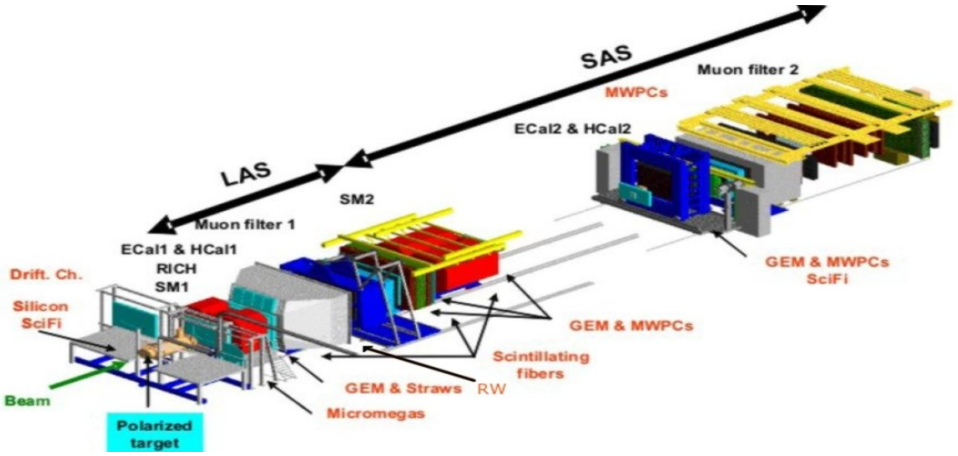

Figure 1: *Layout of the COMPASS experiment at the CERN SPS.*

The COMPASS experiment [1] at the CERN SPS is a modern 2-stage magnetic spectrometer with a flexible setup to allow for a variety of physics programs to be performed with different beams (Fig.1). Common to all measurements is the requirement for high beam intensity and interaction rates with the needs of a high readout speed. The spectrometer is equipped with tracking systems based on silicon detectors for high precision tracking in the target region, micromega and GEM detectors for small area and wire/drift chambers as well as straw tubes for large area tracking. Particle identification is performed in a large acceptance ring imaging cherenkov detector downstream of the first spectrometer magnet and in hadronic (HCAL) and electromagnetic (ECAL) calorimeters in both parts of the spectrometer. The calorimeters are also used for the energy reconstruction of neutral particles. Both parts of the spectrometer are also equipped with muon detectors. For measurements with a polarized nucleons a polarized target is installed about 3m upstream of the first magnet. It consists of two independent target cells filled with ${}^6LiD$ crystals mounted inside a very homogeneous solenoidal field of 2 Tesla. Using the technique of dynamic nuclear polarization 50% of the nucleons could be polarized with a degree polarization of more than 50%. The two target cells are thereby operated with opposite polarization to reduce systematic effects on asymmetry measurements owing to time dependent performance of the apparatus. The study of exclusive reactions using hadron beams requires a short solid target inside a veto-detector surrounded by silicon telescopes. The veto-detector is sensitive to charge and neutral particles with small openings in forward and backward direction. The trigger system is mostly based on scintillator hodoscopes mounted in front of the target and downstream of the second magnet. Using a muon beam deep inelastic scattering (DIS) at large Q^2 is selected as well as low Q^2 events (quasi-real photons) with accompanying hadrons observed in HCAL. For diffractive and Primakoff scattering with hadron beams the target is surrounded by a veto box and small multiplicity events are selected by means of a scintillator and within an online event filter operated inside the event building computers.

4 Lepton-nucleon scattering process

4.1 Kinematics

The lepton-nucleon DIS kinematics is usually described by the following Lorentz-invariant variables:

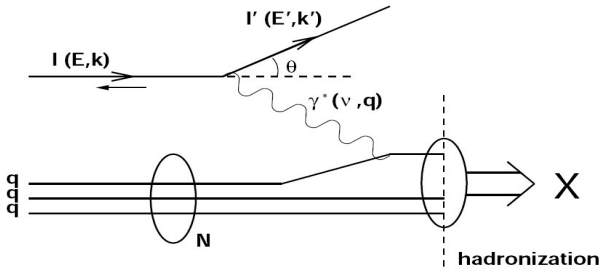

Figure 2: *Deep-inelastic lepton-nucleon scattering process. The photon (γ^*) is exchanged between the lepton (l) and one of the quarks(q) in the nucleon(N). The struck quark and the target remnants fragment into hadrons in the final state(X).*

- The squared four-momentum transfer,

$$Q^2 = -q^2 = -(l - l^{'})^2 = 4EE^{'} \sin^2 \Theta; \tag{1}$$

- the energy transfer to the hadronic system,

$$\nu = p \cdot q/M = E - E^{'}; \tag{2}$$

- the Bjorken scaling variable (the fraction of nucleon momentum carried by the parton in an infinite-momentum frame),

$$x = Q^2/2p \cdot q = Q^2/2M\nu; \tag{3}$$

- the scaling variable,

$$y = p \cdot q/p \cdot k = \nu/E. \tag{4}$$

In these equations $\boldsymbol{l}$, $\boldsymbol{l^{'}}$, $\boldsymbol{p}$ and $\boldsymbol{q}$ are the four-vectors of the incoming and scattered lepton, the target nucleon and the exchanged boson. M is the mass of the target nucleon, whereas the lepton mass is not considered. E,$E^{'}$ are the energies of the incident and scattered lepton, and θ is the lepton scattering angle in the laboratory frame.

4.2 Unpolarized lepton-nucleon scattering

The lowest order interaction of the charged leptons with nucleons can be mediated either by virtual photon or Z boson exchange. At the energies accessible in the COMPASS experiment, the interaction is dominated by virtual photon exchange and the Z-exchange contribution can be neglected.

The elementary lepton-nucleon DIS process can be described as the interaction of the lepton and one of the nucleon partons via the virtual photon exchange. When deriving the cross-section for the lepton-nucleon scattering process, the internal structure of the nucleon is parameterized by two unpolarized structure functions $F_1(x, Q^2)$ and $F_2(x, Q^2)$ so that the differential cross-section can be written, in the Born approximation:

$$\frac{d^2\sigma}{dQ^2dx} = \frac{4\pi\alpha^2}{Q^2}\frac{1}{x}\left[xy^2F_1(x,Q^2) + \left(1 - y - \frac{Mxy}{2E}\right)F_2(x,Q^2)\right] \tag{5}$$

where α is the electromagnetic coupling constant.

The structure functions $F_1(x)$ and $F_2(x)$ have a simple interpretation in the Quark Parton Model (QPM):

$$F_1(x) = \frac{1}{2}\sum_i e_i^2[q_i(x) + \overline{q}_i(x)] \tag{6}$$

$$F_2(x) = \sum_i e_i^2 x[q_i(x) + \overline{q}_i(x)], \tag{7}$$

where $q_i(x)$ and $\overline{q}_i(x)$ are the quark and antiquark densities, i is the quark flavor and e_i is the respective quark charge. The two structure functions are related by the so-called Callan-Gross relation [2], which holds at leading twist for spin-$\frac{1}{2}$ quarks:

$$F_2(x) = 2xF_1(x). \tag{8}$$

4.3 Polarized lepton-nucleon scattering

When the polarized lepton-nucleon scattering is considered, the differential cross-section additionally depends on the direction off the spin quantization axis. It is useful to introduce two planes, the scattering plane and the spin plane, defined respectively by the directions of the incoming and scattered lepton, and the incoming lepton and the spin axis (Fig. 3). The corresponding cross-section can be decomposed into an unpolarized part σ_0 and a polarized part $\Delta\sigma$:

$$\frac{d^3\sigma(\beta)}{dQ^2dxd\phi} = \frac{d^3\sigma_0}{dQ^2dxd\phi} - \frac{d^3\Delta\sigma(\beta)}{dQ^2dxd\phi}. \tag{9}$$

The unpolarized part $\frac{d^2\sigma_0}{dQ^2dx}$ is given by eq. 5, while the polarized part depends on two new structure functions $g_1(x, Q^2)$ and $g_2(x, Q^2)$ which present the same scaling properties as $F_1(x, Q^2)$ and $F_2(x, Q^2)$.

The structure function $g_1(x)$ has a simple interpretation in the QPM:

$$g_1(x) = \frac{1}{2}\sum_i e_i^2\Delta q_i(x), \tag{10}$$

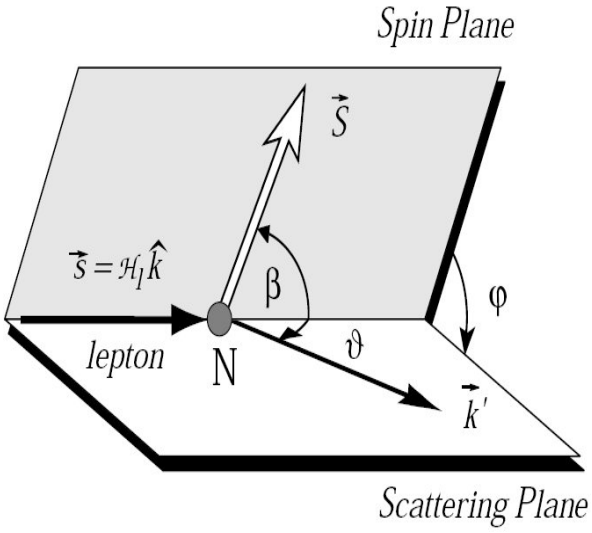

Figure 3: *Kinematics of polarized deep-inelastic lepton-nucleon scattering.*

where

$$\Delta q_i(x) = q_i^+(x) + \overline{q}_i^+(x) - q_i^-(x) - \overline{q}_i^-(x) \tag{11}$$

and where $q_i^+(x)$ ($q_i^-(x)$) is the density of quarks of flavor i with helicity aligned (anti-aligned) to the longitudinal nucleon spin. The function g_2 has no simple interpretation in QPM.

4.4 Sum rules

4.4.1 Bjorken sum rule

Let us consider the first moments of spin-dependent structure functions,

$$\Gamma_1^N = \int_0^1 g_1^N(x)dx, \tag{12}$$

where the superscript N denotes the nucleon type. The most fundamental of these relations is the so-called Bjorken sum rule [3], which predicts the difference of the Γ_1 moments for the neutron:

$$\Gamma_1^p - \Gamma_1^n = \frac{1}{6}\left|\frac{g_A}{g_V}\right|, \tag{13}$$

where g_A and g_V are the axial and vector weak coupling constants of the neutron β-decay. The Bjorken sum rule does not rely on a particular model of the internal structure of the nucleons, since it has been originally derived only from light cone current algebra and isospin invariance.

4.4.2 The nucleon spin and the Ellis-Jaffe sum rules

In the simple quark model, the spin of the proton is carried by its three valence quarks, and the total quark contribution to the nucleon spin is given by:

$$\Delta\Sigma = \Delta u + \Delta d = 1; \quad \Delta s = 0, \tag{14}$$

where

$$\Delta q_i = \int_0^1 [q_i^+(x) - q_i^-(x)]dx = \int_0^1 \Delta q_i(x)dx \tag{15}$$

are the first moments of the spin-dependent parton distribution in the nucleon.

More generally, one writes the spin equation for the proton (or the neutron) as:

$$\frac{1}{2} = \frac{1}{2}\Delta\Sigma + L_q + \Delta G + L_G, \tag{16}$$

where $\Delta\Sigma$ and ΔG are the intrinsic quark and gluon contributions respectively, L_q and L_G are the quark and the gluon angular momenta contributions.

Polarized DIS experiments allows to extract the information about the proton and the neutron spin from the measurement of the structure function $g_1(x)$. A straightforward integration of the equation 10 gives for the three quark flavors(Δc is suppressed due to the fact that charm quark mass is not negligible, so we consider only light quarks),

$$\Gamma_1^p = \frac{1}{2}\left(\frac{4}{9}\Delta u + \frac{1}{9}\Delta d + \frac{1}{9}\Delta s\right), \tag{17}$$

from the isospin invariance,

$$\Gamma_1^n = \frac{1}{2}\left(\frac{1}{9}\Delta u + \frac{4}{9}\Delta d + \frac{1}{9}\Delta s\right). \tag{18}$$

Linear combinations of the Δq_i moments are related to the weak axial-vector couplings a_0, a_3 and a_8 by [4]:

$$a_0 = \Delta u + \Delta d + \Delta s = \Delta\Sigma \tag{19}$$

$$a_3 = \Delta u - \Delta d = \left|\frac{g_A}{g_V}\right| \tag{20}$$

$$a_8 = \Delta u + \Delta d - 2\Delta s, \tag{21}$$

and eq. 17,18 can be rewritten as

$$\Gamma_1^{p(n)}(Q^2) = +(-)\frac{1}{12}a_3 + \frac{1}{36}a_8 + \frac{1}{9}a_0. \tag{22}$$

In flavor-SU(3) symmetry, a_3 and a_8 are related to the symmetric and antisymmetric weak $SU(3)_f$ couplings F and D of the baryon octet:

$$a_3 = \left|\frac{g_A}{g_V}\right| = F + D \tag{23}$$

$$a_8 = 3F - D \tag{24}$$

Under the assumption that the strange sea in the nucleon is unpolarized (i.e. $\Delta s = 0$), $a_0 = a_8$ and eq. 22 takes the form

$$\Gamma_1^{p(n)}(Q^2) = +(-)\frac{1}{12}(F+D) + \frac{5}{36}(3F-D). \tag{25}$$

These are the Ellis-Jaffe sum rules [5]. The ratio F/D was estimated in Refs. [7,8] using hyperon semi-leptonic decay data and exploiting general arguments of SU(3) symmetry breaking. The ratio was found to be $F/D = 0.57 \pm 0.01$.

4.5 The EMC results

The experimental value of the $\Delta\Sigma$ can be calculated from a_3, a_8 and the measured value of the Γ_1 coming from polarized DIS (see eq. 22). The EMC result [9], obtained using high energy muon beam of the CERN SPS, was in complete contradiction with the QPM predictions. The naive constituent quark model would suggest $\Delta\Sigma \simeq \Delta d + \Delta u \simeq 1$, and $\Delta s = 0$. The experimental data allow to extract the separate contributions of u, d and s quarks [10]:

$$\Delta u = 0.83 \pm 0.03, \tag{26}$$

$$\Delta d = -0.43 \pm 0.03, \tag{27}$$

$$\Delta s = -0.10 \pm 0.03, \tag{28}$$

The most surprising result is that $\Delta s < 0$, i.e. the strange sea-quarks are negatively polarized with respect to the proton spin.

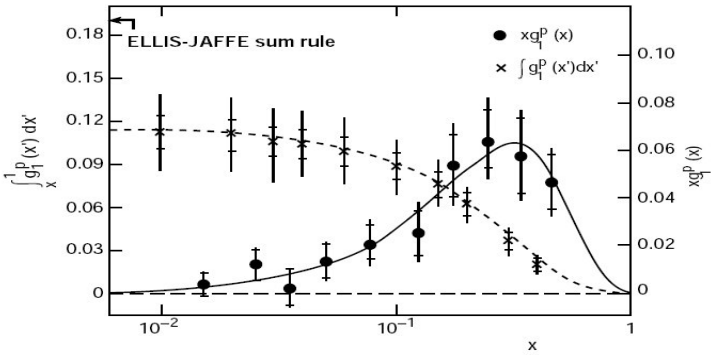

Figure 4: *The EMC result for the Ellis-Jaffe sum rule: solid line is the measured structure function $xg_1^p(x)$, dashed line is the integral $\int_x^1 g_1^p(x')dx'$. The measured $\Gamma_1^p = \int_0^1 g_1^p(x)dx$ is compared with the Ellis-Jaffe prediction. Curves are plotted as a function of x.*

The EMC result, confirmed later by SMC and E154 experiments, invoked vivid interest of theorists([11]). The structure function g_1 depends not only on the polarized quark distribution functions Δq_i, but also on ΔG. Indeed as stated in [6] experimentally one measures not $\sum_i q_i$ but rather a combination $\sum_i (q_i - (\alpha_s/2\pi)\Delta G)$. That is why the smallness of $\Delta\Sigma$ can be explained by a big value of ΔG.

4.6 Gluon polarization $\Delta G/G$ and COMPASS

A possible solution of the "proton spin crisis" can be given by a large polarization of the gluon sea. It is therefore mandatory to perform precise measurements of the polarized gluon distribution function $\Delta G(x)$, where x is the fraction of the nucleon momentum carried by the gluon. Existing estimates of $\Delta G(x)$ imply a value of $\Delta G/G = 0.5$ around $x \simeq 1$, where ΔG has a maximum, and an integral $\int \Delta G(x)dx \simeq 2$ at $Q^2 = 4\ GeV^2$ [1] [12]. This corresponds to a value of $\Delta\Sigma \simeq 0.30$ if the violation of the Ellis-Jaffe sum rule is entirely due to the gluon contribution.

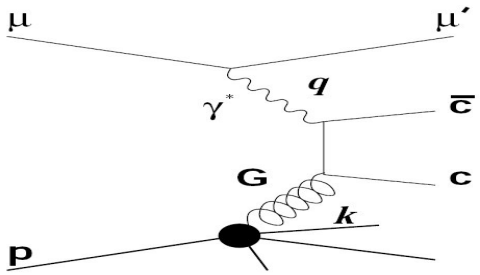

Figure 5: *The photon-gluon fusion diagram. The incoming muon emits a virtual photon which is absorbed by a gluon in the nucleon, through an intermediate state, that fragments into charmed hadrons in the final state.*

The measurement of $\Delta G/G$ distribution is one of the key programs of the COMPASS experiment. Among the various suggestions to measure the gluon distribution functions , the most promising for COMPASS is the longitudinal spin asymmetry of open charm leptoproduction. At leading order, heavy quarks are produced via photon-gluon fusion(PGF) process shown in fig(5). The helicity dependent and helicity averaged cross-section for the process can be expressed as the convolution of the elementary photon-gluon cross-section with the gluon distributions, ΔG and G. The ratio of the two cross-sections represents the virtual photon asymmetry $A_{\gamma N}^{c\bar{c}}$, which is related to the asymmetry for charm muonproduction by the depolarization factor $D(y) = y(2-y)/1+(1-y)^2$:

$$A_{\mu N}^{c\bar{c}} = D \cdot A_{\gamma N}^{c\bar{c}}. \tag{29}$$

The gluon polarization ΔG is accessed through the measurement of the spin dependent asymmetry, A^{exp}, given by [1]:

$$A^{exp} = \frac{N_{c\bar{c}}^{\uparrow\downarrow} - N_{c\bar{c}}^{\uparrow\uparrow}}{N_{c\bar{c}}^{\uparrow\downarrow} + N_{c\bar{c}}^{\uparrow\uparrow}} = P_{Beam} \cdot P_L \cdot f \cdot A_{\mu N}^{c\bar{c}}(y), \tag{30}$$

where $N_{c\bar{c}}^{\uparrow\downarrow(\uparrow\uparrow)}$ are the number of charm events for anti-parallel(parallel) muon and target spin orientations, P_{Beam} and P_L are the beam and target longitudinal polarizations and f is the fraction of polarized material in the target.

4.7 Transverse Hyperon Polarization

Hyperons are an ideal probe to measure polarization effects in high energy reactions. Due to the parity violation of their weak decay, the polarization of the hyperons is reflected in the angular distribution of their decay daughters. This eminent property of the hyperons, referred to as their self-analyzing weak decay, allows a direct extraction of their polarization from the asymmetry of the angular distribution of one of its daughter particles.

If the hyperon H is produced in an unpolarized inclusive reaction like $AB \to H^{\uparrow}X$ and if the interaction in the production process is parity conserving, the hyperon can only be polarized parallel to the normal $\hat{n}$ of the production plane, created by the incoming beam particle and the outgoing hyperon $\hat{n} = \frac{\vec{p}_{beam} \times \vec{p}_H}{|\vec{p}_{beam} \times \vec{p}_H|}$ (see Fig. 6). This is called transverse polarization.

The Λ for example is the lightest hyperon and has a non-leptonic decay mode into two charged particles $\Lambda \to p\pi^-$ with a branching ration of 64%. In the rest frame of the Λ with the z - axis along its spin direction ($J_\Lambda = 1/2, m_\Lambda = +1/2$) angular momentum conservation allows two waves to contribute to the decay amplitude Ref. [13]: a parity violating s-wave, where proton and pion have no relative angular momentum l and where proton and Λ-spin are parallel ($m_\Lambda = m_p = +1/2$), and a parity conserving p-wave, where proton and pion have a relative angular momentum of one unit ($l = 1$). The p-wave consists of two components: One with $m_l = +1$, where the spins of proton and Λ are anti-parallel ($m_\Lambda = -m_p = +1/2$), and another with $m_l = 0$, where the spins are parallel. Hence the total wave function is given by

$$\phi = \phi_s + \phi_p \quad \text{with} \quad \phi_s = A_s Y_0^0 \chi^+ \quad \text{and} \quad \phi_p = A_p \left[\sqrt{\frac{2}{3}} Y_1^1 \chi^- - \sqrt{\frac{1}{3}} Y_1^0 \chi^+ \right] \tag{31}$$

where Y_l^m are the spherical harmonics, $A_{s,p}$ the complex amplitudes, and $\chi^\pm$ the spin wave function of the two possible spin states of the decay proton with respect to the Λ spin.

Eq. 31 together with the orthonormality of the spin wave functions and the definition of the spherical harmonics gives the angular distribution:

$$\frac{dN}{d\cos\Theta} \propto \phi\phi^* = \frac{1}{4\pi} \left[|A_s|^2 + |A_p|^2 - \left(A_s^* A_p + A_s A_p^* \right) \cos\Theta \right] \tag{32}$$

where Θ is the polar angle of the proton with respect to the quantization axis in the hyperon's rest frame. Without loss of generality one of the complex phases can be chosen to be real: $A_s \in \mathbb{R}$. This simplifies the interference term in eq. 32 and gives

$$\frac{dN}{d\cos\Theta} \propto (1 + \alpha \cos\Theta) \quad \text{with} \quad \alpha \equiv -\frac{2A_s \Re(A_p)}{|A_s|^2 + |A_p|^2} \tag{33}$$

The interference of the s- and p-waves, which due to parity violation are both allowed in the weak decay, causes the decay baryon to be preferentially emitted either along or opposite to the spin direction of the hyperon, depending on the sign of α. α is the so called decay asymmetry parameter and describes the details of the weak decay process. In order to have a non-vanishing asymmetry parameter, both amplitudes A_s and A_p have

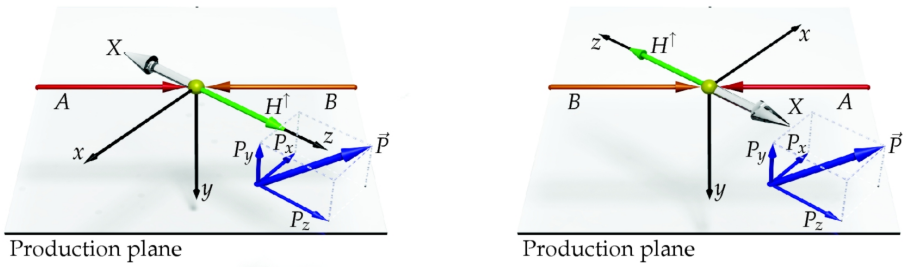

(a) **(b)**

Figure 6: Prod. plane(a) Production of a polarized hyperon in the unpolarized inclusive reaction $AB \to H^\uparrow X$. The coordinate system is defined by the reaction and chosen such, that the y-axis is along the normal of the production plane and the z-axis along the hyperon direction. The polarization $\vec{P}$ of the hyperon is assumed to have an arbitrary orientation with components P_x, P_y, and P_z with respect to the coordinate axes. (b) The same process after the parity operator P was applied: It is evident, that, if the coordinate system is chosen in the same way as in (a), the x and z-components of the polarization flip sign, whereas the y-component stays unchanged, because the production plane normal still points in the same direction. If the process is parity conserving, both P_x and P_z average to zero, so that the polarization is always transverse to the production plane.

to be non-zero. Tab. 4.7 summarizes the decay asymmetry parameters of some hyperon decays.

Hyperon	Decay channel	Branching ratio	Asymmetry parameter α
Λ^0	$p\pi^-$	63.9±0.5 %	0.642±0.013
Λ^0	$n\pi^0$	35.8±0.5 %	0.65±0.05
Σ^+	$p\pi^0$	51.57±0.30 %	−0.980±0.017
Σ^+	$n\pi^+$	48.31±0.30 %	0.068±0.013
Σ^-	$n\pi^-$	99.848±0.005 %	−0.068±0.008
Ξ^0	$\Lambda\pi^0$	99.522±0.032 %	−0.411±0.022
Ξ^-	$\Lambda\pi^-$	99.887±0.035 %	−0.458±0.012
Ω^-	ΛK^-	67.8±0.7 %	−0.026±0.023
Ω^-	$\Xi^0\pi^-$	23.6±0.7 %	0.09±0.14

Eq. 32 describes the angular distribution in a frame, where the axis, with respect to which the angle Θ is defined, was chosen to be always along the spin of the hyperon. In a measurement such a frame is not possible to realize, instead an analyzer direction $\hat{n}$ is chosen, along which the polarization P is measured. For a spin-1/2 particle the polarization is defined as

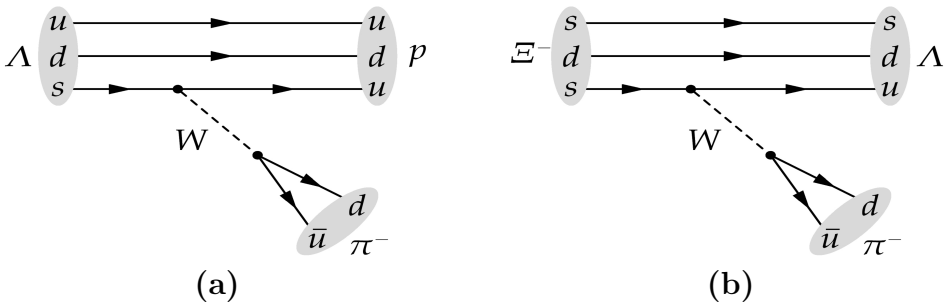

Figure 7: (a) Decay of the Λ hyperon into proton and pion and (b) that of the Ξ^- hyperon into Λ and pion both via exchange of a W boson.

$$P \equiv < \vec{\sigma} \cdot \hat{n} > = \frac{N^{\uparrow} - N^{\downarrow}}{N^{\uparrow} + N^{\downarrow}} \tag{34}$$

where $\vec{\sigma}$ is the spin operator and $N^{\uparrow(\downarrow)}$ the number of particles with spin along (opposite) to the quantization axis. In this analysis the production plane normal is used as the analyzer to measure the transverse hyperon polarization P_T^H. Redefining the angle Θ to be taken with respect to the production plane normal $\hat{n}$ gives the measurable angular distribution, that now includes the transverse polarization:

$$\frac{dN}{d\cos\Theta} = \frac{N_0}{2}\left(1 + \alpha_H P_T^H \cos\Theta\right) \tag{35}$$

Due to the self-analyzing weak decay, a possible transverse polarization of the hyperon manifests itself as an up-down asymmetry of the distribution of the daughter particles with respect to the production plane.

The production of polarized hyperons in the reaction $a + b \to \Lambda + X$ can be described in terms of spin-flip ($ab\bar{c}_\lambda \to ab\bar{c}_{-\lambda}$, there $\lambda = \pm$) and spin-non-flip ($ab\bar{c}_\lambda \to ab\bar{c}_\lambda$, there λ is the same on the both sides) forward amplitudes A_F and A_N Ref. [14]. According to the generalized optical theorem the polarization is given by eq. 36.

$$P_T^H = \frac{\mathrm{Im}(A_N A_F^*)}{|A_N|^2 + |A_F|^2} \tag{36}$$

Hence a polarization different from zero requires both amplitudes to be non-vanishing and to have moreover a non-zero phase difference. At high energies, however, a large number of possible reaction channels contribute to the production cross section with comparable magnitudes and various relative phases. Therefore the polarization in inclusive high energy processes is expected to be small, since in the weighted mean over all contributing channels the relative phases interfere randomly.

Let us first shortly summarize the experimental results on hyperon polarization, gathered so far, and then introduce two of the models, that are proposed to explain the data.

4.7.1 Hyperon Polarization Data - A brief Overview

The story of hyperon polarization in high energy reactions started over 30 years ago at Fermilab where Λ hyperons, produced by a 300 GeV/c proton beam in the unpolarized

inclusive reaction $pBe \rightarrow \Lambda X$, were found to have a sizeable polarization opposite to the normal of the production plane Ref. [15]. Considering the arguments given in the previous section, this discovery came as a surprise. It was the first indication, that the spin seems to be an important factor in high energy hadronic reactions.

The bulk of data on hyperon and anti-hyperon polarization was collected in proton-beam experiments, where it was found that the various hyperons show a similar behavior: The absolute value of the hyperon polarization rises approximately linearly with the transverse momentum p_T of the hyperon, starting at zero for $p_T = 0\ GeV/c$, as required by rotational symmetry, and reaching a plateau at $p_T \approx 1\ GeV/c$. Up to the highest measured transverse momenta of $p_T \approx 3.5\ GeV/c$ no drop of the polarization, as expected by pQCD, was seen. In the plateau region the polarization rises almost linearly with the Feynman variable[1] x_F of the hyperon. The polarization is virtually independent of the beam energy and shows only a weak dependence on the atomic mass number A of the target.

In particular the polarization of the Λ hyperon was studied in great detail in the current fragmentation region by proton-beam experiments at Fermilab Ref. [15–18] and at CERN Ref. [19–21], which measured a negative polarization. Other proton beam experiments showed that nearly all hyperons are produced polarized with a comparable magnitude of the polarization of about 20% at large x_F in the plateau region, where $p_T > 1\ GeV/c$ (see Fig. 8a).

For the anti-hyperons the picture is less clear: Whereas the $\overline{\Lambda}$ is produced unpolarized Ref. [16–18,21,22], $\overline{\Sigma}^-$ and $\overline{\Xi}^+$ exhibit a polarization with the same sign as the respective hyperons: $P_T^{\overline{\Sigma}^-} \approx 10\%$ Ref. [23] and $P_T^{\overline{\Xi}^+} \approx -10\%$ Ref. [24] (see Fig. 8b).

$\overline{\Lambda}$s produced by anti-protons Ref. [25] as well as Λs produced by a neutron beam Ref. [26] show a similar behavior like Λs from proton induced reactions. The same is true for the exclusive diffractive process $pp \rightarrow p(\Lambda K^+)$, except that the Λ exhibits a remarkably strong negative polarization below -60% Ref. [27].

The behavior of the hyperon polarization changes, if the strange quark content of the outgoing hyperon is not produced from the sea, like in proton induced reactions, but is instead brought in by the beam particle: Λs produced by a K^- beam show a sizeable positive polarization in the current fragmentation region, opposite to the one observed in proton data Ref. [25, 29, 30]. $\overline{\Lambda}$s from a K+ beam Ref. [31] behave similarly. The same phenomenon was observed for Λs from a Σ^- beam, where in addition a first possible hint for the breakdown of the polarization at large p_T was seen Ref. [32]. Whereas Ξ^- hyperons from proton beams have a sizeable negative polarization, they were found to be unpolarized, if produced by a beam consisting mainly of n, Λ, and Ξ^0 Ref. [33]. In the same beam the Ω^- showed a small positive polarization. If produced by a Σ^- beam, the Ξ^- polarization on the other hand exhibits a behavior very similar to that of the proton data Ref. [34], whereas Ξ^-s produced by K^-s have a large positive polarization Ref. [35].

[1]The Feynman variable x_F is the fraction of the incident beam momentum $p_{z,max}$ carried by the hyperon in the beam direction $x_F = p_z/p_{z,max}$. x_F is not Lorentz-invariant and usually defined in the center-of-mass system of beam and target. In this system x_F is given by $x_F \approx 2p_{z,cm}/\sqrt{s}$, where $\sqrt{s}$ is the center-of-mass energy. x_F may range from -1 to 1, where positive values mean that the hyperon goes into the forward hemisphere and thus probably stems from the beam particle. Therefore this kinematical domain is called current or beam fragmentation region. In a similar way negative x_F indicate, that the hyperon production is dominated by the target and is thus called target fragmentation region.

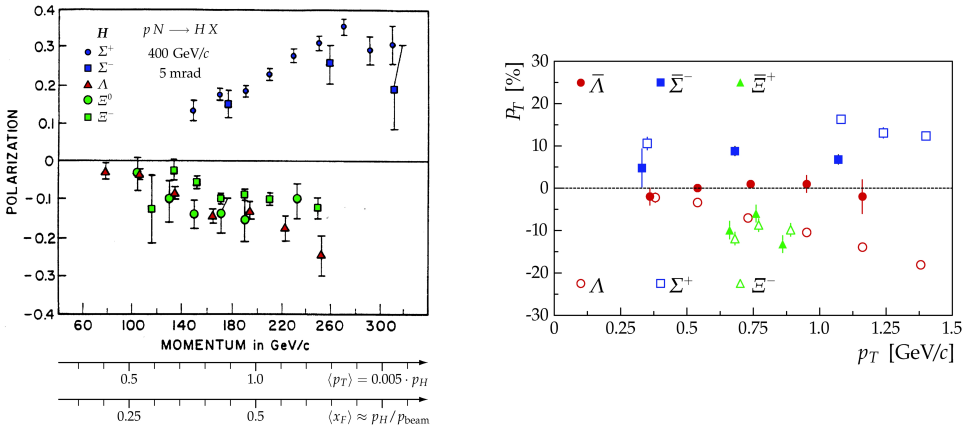

(a) (b)

Figure 8: Polarization of various hyperons and anti-hyperons measured in proton induced inclusive reactions: (a) Polarization of hyperons from a 400 GeV/c proton beam as a function of their momentum, which, due to the fixed scattering angle, is proportional to their transverse momentum p_T as well as to their longitudinal momentum fraction x_F. (b) Polarization of anti-hyperons in dependence of p_T. For comparison the hyperon polarizations measured by the same experiments are shown as well. (from [28])

Λs from pion beams exhibit a small negative polarization Ref. [36] and $\overline{\Lambda}$s Ref. [37] are produced unpolarized.

Two older experiments Ref. [38, 39] studied the Λ and $\overline{\Lambda}$ polarizations in photoproduction with photon energies between 20 and 70 GeV. Both experiments are limited by statistics and measured polarizations compatible with zero. Nevertheless they seem to indicate a small positive Λ polarization. This was confirmed by a HERMES measurement Ref. [40–42] in quasi-real photo-production, which resulted an average Λ polarization of $+5.5\%$ and an $\overline{\Lambda}$ polarization of -4.3%.

4.7.2 Theoretical Models

The previous section showed that the transverse polarization of hyperons is a complex phenomenon. Within the current framework of perturbative QCD the polarization cannot be calculated from first principles, because the hyperon production in proton induced reactions in the current fragmentation region at small transverse momenta is a soft process. A number of models try to explain the experimental data using different polarization mechanisms: Ref. [16] proposes that polarized $s\overline{s}$ pairs are created by polarized gluon bremsstrahlung. In Ref. [43] the $s\overline{s}$ pairs originate from the breaking of a stretched color flux tube. Since the s quark has a transverse momentum the $s\overline{s}$ pair has to have angular momentum, which is balanced by the quark spins. In analogy to multiple Coulomb scattering Ref. [44] considers the polarization of massive s quarks by multiple scattering in quark-gluon matter. Ref. [45] developed a model that explains the polarization with the Thomas precession of the participating quark spins.

Beside these semi-classical models there are also some, that are based on Regge theory. In the triple-Regge model Ref. [46] the Λ production is described by three processes: direct

production, intermediate baryon dissociation via Σ and Σ^*, and electromagnetic decay of Σ^0. The one pion exchange model Ref. [47] is based on the dominance of the pion exchange in hadronic amplitudes and reduces the Λ production to the reaction $\pi p \to K\Lambda$ with reggeized off-shell pions.

None of the proposed theoretical models is able to describe all observed polarization phenomena in a consistent way. Up to now the details of the mechanism, that creates the polarization, are not understood. A more in-depth discussion of the proposed models and the current theoretical developments is given in Ref. [14, 48].

The following subsection is introduced the recombination model by DeGrand and Miettinen as a typical example for a semi-classical model. Notwithstanding its simplicity, it is able to predict at least on a qualitative level many observed hyperon polarizations. Section 4.7.4 presents a recent phenomenological approach to describe the Λ polarization in deeply inelastic scattering by applying pQCD factorization schemes, that separate the non-perturbative polarizing process into a measurable quantity.

4.7.3 Parton Recombination Model by DeGrand and Miettinen

In the parton recombination model developed by DeGrand and Miettinen Ref. [45, 49, 50] the polarization in inclusive baryon fragmentation is reduced to the polarization in the underlying partonic subprocess. The model considers the scattering of a baryon B with momentum p_B on a target, thereby producing baryon $B^{'}$ with momentum $p_{B'}$. $B^{'}$ carries a longitudinal momentum fraction x_F with respect to B and has a small transverse momentum p_T. The polarization is measured along the normal $\hat{n}$ of the production plane, that is also the scattering plane and is spanned by the two baryons $\hat{n} \propto \vec{p}_B \times \vec{p}_{B'}$.

The beam baryon is considered in an infinite momentum frame, where its wave function can be decomposed into partonic wave functions. The three valence partons determine the flavor quantum numbers and carry the major part of the baryon momentum, whereas the numerous sea partons contribute only a small part to the momentum and possess no net quantum numbers. The B and B' share the maximum possible number of valence quarks and these valence quarks have the same wave functions in the fragmenting and in the outgoing baryon. The production of $B^{'}$ via baryon resonances is neglected, so that the predictions are valid only for "promptly" produced baryons.

There are three classes of recombination processes: If two valence partons from the beam baryon B recombine with one sea parton to form $B^{'}$, as it is the case for the Λ production by a proton beam, where the *ud* diquark of the beam proton recombines with an *s* quark from the sea, this is called VVS recombination. In VSS recombination B and $B^{'}$ share only one valence parton like in the Ξ^- production by protons, where the *d* quark from the proton recombines with an *ss* diquark from the sea. The case, where B and $B^{'}$ have no valence quarks in common, so that all valence partons of the outgoing baryon have to be created from the sea, is called SSS recombination, which applies to all anti-baryons produced by baryons.

The sea partons are supposed to be unpolarized. The polarization is built up in the process of recombination, where certain spin directions are preferred. It turns out that nearly all polarization data can be explained at least qualitatively by a simple rule: *Slow (sea) partons recombine preferentially with their spin down with respect to the production plane, while fast (valence) partons recombine with their spin up.* DeGrand and Miettinen

propose that this correlation of spin and momentum is caused by the change of the parton momentum during the recombination process, which is not collinear to the parton momentum and therefore leads to a Thomas precession of the parton's spin.

Considering the structure of the VVS and VSS recombination processes it is convenient to represent the baryons as a combination of quark and diquark, where the internal diquark interaction is neglected.

In the VVS recombination process one valence quark q of the beam baryon's wave function is replaced by a different quark q' from the sea. The model assumes, that there exists a **T**-matrix amplitude for this process, which can be factorized in a valence quark term **V** and a sea quark term **S** with $\mathbf{T} = \mathbf{VS}$.

The cross section is calculated as the incoherent sum of the squared amplitudes over all possible spin states of q and $q^{'}$:

$$\sigma(B \to B^{'}) \propto \sum_{s_D=0,1} \sum_{m_q^{'}+m_D=m_B^{'}} \left|(Ds_D m_D q^{'} m_{q^{'}}|B^{'} s_{B^{'}} m_{B^{'}}) V^D_{s_D m_D} S^{q^{'}}_{m_{q^{'}}}\right|^2 \tag{37}$$

The interference terms are assumed to be negligible, because the outgoing spectator valence quarks have different spin states, that do not overlap.

To describe the data the amplitudes are parameterized:

$$|S_{\uparrow\downarrow}|^2 = A(1 \mp \epsilon), \quad |V_{00}| = B, \quad |V_{1m_D}|^2 = B(1 + m_D\delta) \tag{38}$$

where ϵ and δ are small parameters, which depend on x_F and p_T of the outgoing baryon. The experimental data suggest that $\epsilon \approx \delta$. In the parameterization the signs of ϵ and δ are chosen such, that the cross section is enhanced, if the valence partons from the beam particle's wave function recombine with spin up and the sea partons with spin down.

The simplest example is that of $p \to \Lambda$ (Fig. 9a): Since the valence ud diquark in the Λ is in a spin-0 singlet state, the spin of the Λ is determined by the spin of the s quark(39).

$$\begin{array}{l} P_T^\Lambda = \frac{\sigma(p\to\Lambda^\uparrow)-\sigma(p\to\Lambda^\downarrow)}{\sigma(p\to\Lambda)} \quad \text{with} \quad \sigma(p \to \Lambda^{\uparrow(\downarrow)}) \propto |V_{00}^{ud}|^2 |S^s_{\uparrow(\downarrow)}|^2 \\ P_T^\Lambda = -\eta \end{array} \tag{39}$$

The VSS recombination can be described in the same way by exchanging the roles of quark and diquark. The outgoing baryon is produced by replacing the valence diquark D of the beam baryon by the diquark $D^{'}$ from the sea, which recombines with the valence quark, that is shared by B and $B^{'}$.

The cross section is again calculated as the incoherent sum of the squared amplitudes over all spin states of D and $D^{'}$.

$$\sigma(B \to B^{'}) \propto \sum_{s_{D^{'}}=0,1} \sum_{m_{D^{'}}+m_q=m_{B^{'}}} \left|(D^{'} s_{D^{'}} m_{D^{'}} q m_q|B^{'} s_{B^{'}} m_{B^{'}}) V^q_{m_q} S^{D^{'}}_{s_{D^{'}} m_{D^{'}}}\right|^2 \tag{40}$$

The same parameterization as in the VVS case is used, but the signs of ϵ and δ are reversed in order to comply with the recombination rule, that sea quarks recombine as a matter of preference with spin down and valence quarks with spin up. The process $p \to \Xi^-$ is an example for a VSS recombination (see Fig. 9b).

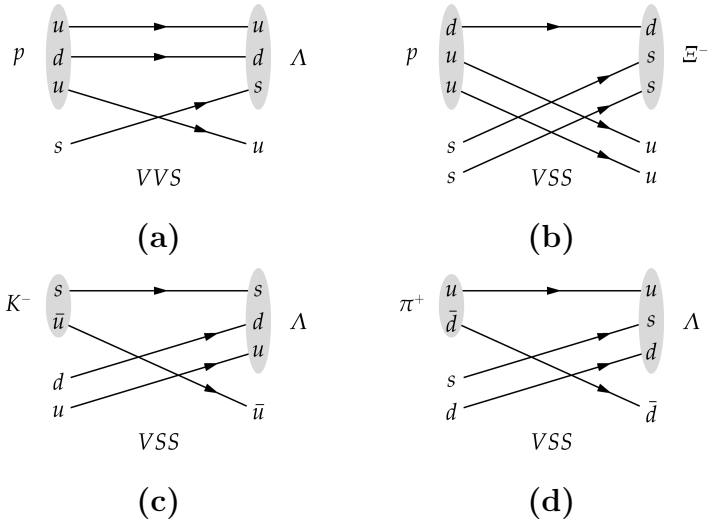

Figure 9: Schematic illustration of some VVS and VSS recombination processes.

For SSS recombination processes like $p \to \overline{L}$ the model predicts zero polarization, because the involved sea partons do not exhibit a strong momentum hierarchy. There are equally many configurations in which the same parton is both faster and slower than the diquark, so that the effect cancels on the average.

The same scheme also predicts the polarization of leading baryons in meson fragmentation. The reaction $K^- \to \Lambda$ can be described as a VSS recombination of the valence s quark from the kaon with a spin-0 singlet ud diquark from the sea (see Fig. 9c). In analogy to eq. 39 the Λ polarization is calculated to be $P_T(K^- \to \Lambda) = +\epsilon$. The same polarization is expected in the reaction $K^+ \to \overline{\Lambda}$. Both predictions are in agreement with the experimental findings. The VSS recombination scheme also applies to the production of leading Λs by pion and K^+ beams, where the valence quark is a u or d quark, respectively (cf. Fig. 9d), and predicts in all three cases a negative polarization of $P_T(\pi^\pm \to \Lambda) = P_T(K^+ \to \Lambda) = -\delta/2$.

The above results are universal in the sense, that no assumption on the actual polarization mechanism, that determines the two parameters ϵ and δ, is made. Table 4.7.3 compares some predictions with experimental results and shows that for the considered reactions at least the sign of the polarizations is predicted correctly. For part of the processes also the relative magnitudes are reproduced.

Transition	Predicted P_T^H	Observed P_T^H	Energy [GeV]
$p \to \Lambda$	$-\epsilon$	$-0.1 \ldots -0.2$	$24 \ldots 2000$
$p \to \overline{\Lambda}$	0	0	$24 \ldots 2000$
$p \to \Sigma^+$	ϵ	$0.1 \ldots 0.2$	400
$p \to \Sigma^-$	$\epsilon/2$	$0.15 \ldots 0.3$	400
$p \to \Xi^0$	$-\epsilon$	$-0.1 \ldots -0.2$	400
$p \to \Xi^-$	$-\epsilon$	$-0.1 \ldots -0.2$	400
$K^+ \to \overline{\Lambda}$	ϵ	$> 0.4 \; for \; x_F > 0.3$	32, 70
$K^- \to \Lambda$	ϵ	0.4	14
$\pi^- \to \Lambda$	$-\epsilon/2$	-0.05	18

In order to explain the rule, that fast partons recombine preferentially with spin up and slow partons with spin down, which was used to derive the results discussed above, DeGrand and Miettinen propose a simple semi-classical model. The simplest case is again that of Λ production by a proton beam ($p \to \Lambda$): The recombining s quark stems from the sea of the beam proton and has thus only a small momentum fraction of $x_B^s \approx 0.1$. During the recombination process this quark becomes a valence quark of the outgoing Λ in which it carries a large momentum fraction of about 1/3. Because the Λ carries a large longitudinal fraction x_F of the beam proton momentum p_B, the s quark experiences an increase of its longitudinal momentum from $x_B^s p_B$ to $1/3 x_F p_B$. The transverse momentum $k_\perp$ of the s quark on the other hand remains approximately unchanged during the recombination process $k_\perp^p \approx k_\perp^\Lambda$ and is roughly parallel to the transverse momentum p_T of the outgoing Λ. This means that the change of momentum of the s quark is not collinear to its momentum which, due to the fermion nature of the quark causes a Thomas precession of the s quark's spin (see Fig. 10).

It is assumed that the recombination process can be described by equations of motion in a confining scalar force field. The evolution of the rest frame of the s quark can be expressed as a series of infinitesimal Lorentz boosts without rotation. The infinitesimal boosts are not collinear and, since the product of two non collinear boosts is equivalent to a boost plus a rotation (also known as Wigner rotation), the rest frame experiences an additional rotation - the Thomas precession.

Despite its simplicity the model of DeGrand and Miettinen is able to predict the relative signs of various hyperon polarizations and for part of the transitions also the relative magnitudes. It fails to explain the non-vanishing polarizations of the $\overline{\Sigma}^-$ and $\overline{\Xi}^+$ antihyperons. Whereas the p_T dependence of the polarization is at least qualitatively reproduced by the semi-classical Thomas precession model, this is not true for the observed x_F behavior. Yamamoto et al. Ref. [51] have extended the model using a relativistic formulation of the parton-parton interaction, that describes the relativistic quark kinematics including the dynamics of the spin polarization. Based on experimentally extracted momentum distribution functions for quarks and diquarks, the so-called Quark ReCombination (QRC) model is able to describe the p_T as well as the x_F dependence for various transitions.

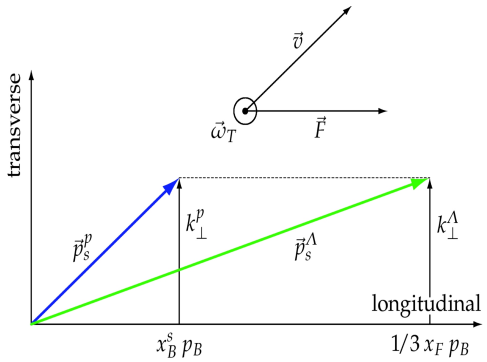

Figure 10: Thomas precession in the semi-classical parton recombination model for $p \to \Lambda$: In the initial state of the beam proton the s quark has the momentum $\vec{p}_s^{\,p}$ with a small longitudinal component $x_B^s p_B$. In the final state of the outgoing Λ hyperon the quark momentum $\vec{p}_s^{\,\Lambda}$ has a larger longitudinal component $1/3 x_F p_B$. Since the transverse momentum components $k_\perp^p$ and $k_\perp^\Lambda$ of the s quark remain unchanged, the total change of the s quark momentum and thus the accelerating force $\vec{F}$ is along the longitudinal direction and is not collinear to $\vec{p}_s^{\,p}$ or $\vec{p}_s^{\,\Lambda}$. The angular velocity of the resulting Thomas precession is parallel to $\vec{F} \times \vec{v}$ and points in direction of the production plane normal.

4.7.4 Polarizing Fragmentation Functions

Anselmino et al. propose a phenomenological approach to the problem of transverse Λ polarization in the current fragmentation region of deeply inelastic scattering, that is based on pQCD and factorization schemes and includes effects from spin and from intrinsic transverse momentum $\vec{k}_\perp$ Ref. [52–56]. The central idea is the introduction of a new kind of fragmentation function, the so-called polarizing fragmentation functions (pFF), that were first described by Mulders and Tangerman Ref. [57] and that are thought to describe a universal feature of the hadronization process, which makes them independent of the nature of the hadronic target. The pFFs have an interpretation in the parton picture, a formal definition, and are free of ambiguities concerning initial-state interactions.

The basic assumption is that the Λ polarization is built up during the fragmentation of an unpolarized quark, which is described by the polarizing fragmentation functions. In order to not violate the rotational invariance of the pFFs, the Λ has to have a non-zero transverse momentum $\vec{k}_\perp$ with respect to the fragmenting quark. Due to the above simplifications the fragmenting quark is collinear to the virtual photon and the kinematics is limited to the beam fragmentation region, where $x_F > 0$. The intrinsic transverse momentum $\vec{k}_\perp$ of the Λ is equal to the transverse momentum $\vec{p}_T$ of the Λ with respect to the virtual photon (see Fig. 11).

The fragmentation of an unpolarized quark q with momentum $\vec{p}_q$ into an unobserved rest X and a polarized Λ with momentum $z_h \vec{p}_q + \vec{k}_\perp$, where $\vec{p}_q \cdot \vec{k}_\perp = 0$, and polarization direction $\uparrow$ is described by the fragmentation function $\hat{D}_{\Lambda^\uparrow/q}(z_h, \vec{k}_\perp)$.

Anselmino et al. obtained qualitative and generic numerical estimates for the transverse Λ and $\overline{\Lambda}$ polarization using a Gaussian model for the explicit $k_\perp$ dependence of the fragmentation functions (see Ref. [55]). shows the numerical results for P_T^Λ and $P_T^{\overline{\Lambda}}$ as a function of z_h, averaged over p_T. The polarization is in both cases negative and increases strongly with z_h.

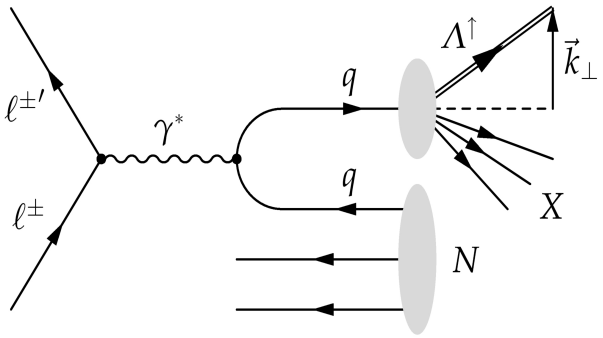

Figure 11: Illustration of the Λ production in SIDIS at leading order and leading twist: In this approximation the intrinsic transverse momentum $\vec{k}_\perp$ of the Λ is equal to its transverse momentum $\vec{p}_T$, which is a directly measurable quantity.

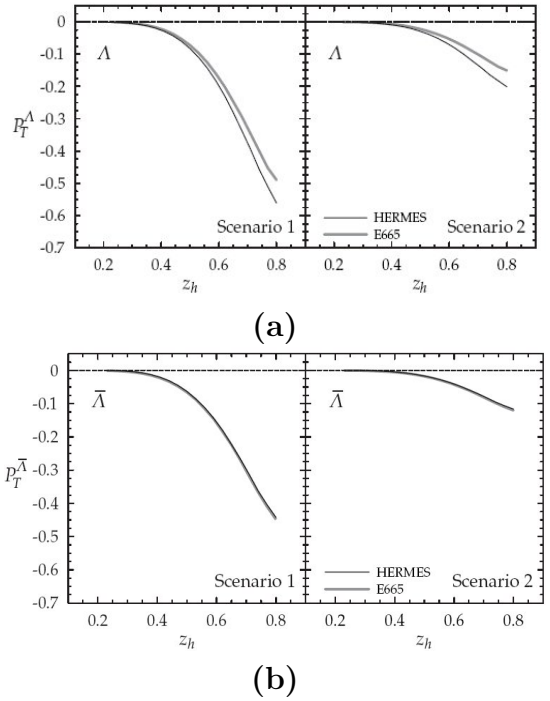

Figure 12: (a) Numerical results for the p_T-averaged transverse Λ polarization P_T^Λ as a function of z_h for the HERMES and E665 kinematics in two different scenarios described in the text. (b) shows the same for the $\bar{\Lambda}$. [55]

5 The transverse spin of the nucleon

The quark structure of the nucleon at twist-two level is fully specified by three distribution functions: the momentum distributions $q(x)$, the helicity distributions $\Delta q(x)$ and the transverse spin distributions $\Delta_T q(x)$,

$$\Delta_T q(x) = q^{\uparrow}(x) - q^{\downarrow}(x), \tag{41}$$

where $q^{\uparrow(\downarrow)}(x)$ is the probability to find a quark q with its spin parallel (antiparallel) to the transverse spin of the nucleon, and carrying a fraction x of the nucleon momentum.

In the nonrelativistic case the transversity and the helicity distributions exactly coincide, however in the relativistic case a difference arises. That is why we speak about three fundamental distributions of quarks inside the nucleon.

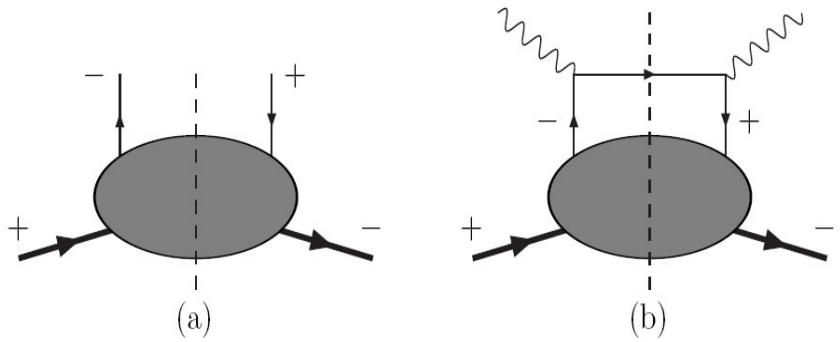

Figure 13: (a) Representation of the chirally-odd distribution $\Delta_T q(x)$. (b) A handbag diagram forbidden by chirality conservation.

Transversity distributions are not observable in fully inclusive DIS. Indeed the $\Delta_T q$ is a chirally-odd quantity (see Fig. 13a). Fully inclusive DIS can be described by the so-called handbag diagram which cannot flip the chirality of the probed quark (see Fig. 13b). In order to measure $\Delta_T q$ the chirality must be flipped twice, so one needs either two hadrons in the initial state (hadron-hadron collisions), or one hadron in the initial state and one in the final state (semi-inclusive leptoproduction), and at least one of these two hadrons must be transversely polarized.

The "golden channels" for the measurement of $\Delta_T q(x)$ are the azimuthal asymmetries in pion production (Collins effect) [58] and the Drell-Yan scattering [60]. The problem of the proposed measurement through the Drell-Yan process was that it in not an easily available reaction in the experiments. A possible alternative approach, based on the measurement of the spin transfer to the Lambda hyperons produced in the semi inclusive deep inelastic scattering on transversely polarized targets, has been originally suggested in [61–63], and more recently by Anselmino et al. [64].

The measurement is based on the following idea: when a lepton interacts with one of the valence quarks of a transversely polarized nucleon, the scattered quark leaves the nucleon within a polarization state that is completely determined by its transverse spin distribution function inside the nucleon ($\Delta_T q(x)$) and the kinematics of the lepton-photon vertex. In particular, if the struck quark was initially in the same polarization state as the parent nucleon, then after the scattering the quark will be polarized along an axis

that is obtained by reflecting the target polarization axis with respect to the normal to the lepton scattering plane. The final quark polarization is also reduced by the so-called virtual photon depolarization factor, originating from the lepton-photon QED vertex and given by $D_{NN}(y) = 2(1-y)/[1+(1-y)^2]$, where y is the fraction of the incoming lepton energy carried by the exchanged virtual photon.

The struck quark has a certain probability to fragment into a Lambda hyperon. If at least part of its polarization is transferred in the fragmentation process, then the angular distribution in the weak $\Lambda^0 \to p\pi^-$ decay can provide information on the initial polarization state of the quark in the nucleon. On the Fig.14 one can see the reflection with respect to the normal (y) to the lepton scattering plane $(\mu - \mu^{'})$ and dilution by the depolarization factor of the initial quark polarization vector (T).

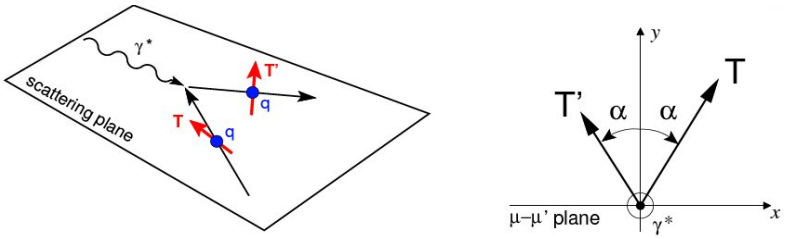

Figure 14: *Lepton-photon vertex.*

The lambda polarization measured experimentally is given by:

$$P_\Lambda^T = \frac{d\sigma^{lp^\uparrow \to \Lambda^\uparrow X} - d\sigma^{lp^\uparrow \to \Lambda^\downarrow X}}{d\sigma^{lp^\uparrow \to \Lambda^\uparrow X} + d\sigma^{lp^\uparrow \to \Lambda^\downarrow X}} = f P_T D_{NN}(y) \cdot \frac{\sum_q e_q^2 \Delta_T q(x) \Delta_T D_{\Lambda/q}(z)}{\sum_q e_q^2 q(x) \Delta_T D_{\Lambda/q}(z)}, \qquad (42)$$

where the T-axis is the polarization vector of the struck quark as described before, P_T and f are the target transverse polarization and dilution factor respectively, and $\Delta_T D_{\Lambda/q}(z)$ is the polarized fragmentation function that describes the spin transfer from the quark to the final state hyperon.

6 Λ polarization in deep inelastic lepton scattering

The strange quark content of the nucleon is currently of great theoretical and experimental interest. A constituent quark model has been proposed, in which a valence quark core may be accompanied by a spin triplet $s\overline{s}$ pair in which both quarks are negatively polarized. The effect of the polarized strange sea-quarks would be an effective "screening" of the valence quark spin, which would explain the small measure value of $\Delta\Sigma$ [65].

The Λ hyperons produced in polarized deep inelastic lepton scattering are of special interest for the measurement of the strange sea-quarks properties. In the simple parton model representation of hadrons, the Λ hyperon contain a ud pair in a singlet state, and an s quark carrying all the spin of the hyperon. The Λ hyperon undergo a weak decay in $p\pi^-$ in 60% of the cases, a fact that makes them act as natural polarimeters for strange quark polarization. If the produced Λ has a net polarization P_Λ along a certain direction $\hat{n}$, the decay proton distribution is given by

$$W(\Theta_p^*) = \frac{1}{4\pi}[1 + P_\Lambda \cos(\Theta_p^*)], \tag{43}$$

where Θ_p^* is the polar angle between the proton direction and the polarization axis $\hat{n}$, measured in the Λ helicity rest frame.

When discussing the production of the Λ hyperons in polarized lepton-nucleon DIS, it is fundamental to distinguish between the target fragmentation region and the current fragmentation region, according to the sign of the x-Feynman(x_F) kinematical variable, defined as a ratio between the measured and the maximum allowed Λ longitudinal momenta, in the $\gamma^* N$ center of mass frame:

$$x_F = \frac{p_L^\Lambda}{p_{L_{MAX}}^\Lambda} \approx \frac{2p_L^\Lambda}{\sqrt{W^2}}, \tag{44}$$

where $W^2 = (p+q)^2$. Λ produced with negative x_F originate from the hadronization of the nucleon fragments which did not interact with the virtual photon, while the struck quark gives rise to Λ in the $x_F > 0$ region.

6.1 Target fragmentation region

The polarization of Λ hyperons produced in deep-inelastic scattering of longitudinally polarized muons on a longitudinally polarized target is expected to give clean information on the nucleon spin structure. The argument is based on the fact that the electromagnetic interaction of longitudinally polarized leptons has different cross-section for different quark longitudinal polarization states [65]. The struck quark (anti-quark) in the target has non-zero net longitudinal polarization, and the intrinsic strange sea-quark polarization model predicts an opposite sign for the polarization of the remnant s quark (see Fig 15-a). If s-quark polarization is transfered to the Λ in the target fragmentation region, the observation of the distribution of the decay proton with respect to the direction of the virtual photon gives information on the strange sea-quark polarization.

It is interesting to note that the polarized-gluon model leads to an opposite prediction of the Λ polarization sign(see Fig. 15-b). In this case the gluon, and hence the s-quark in the produced Λ, is expected to be correlated with the struck quark [65].

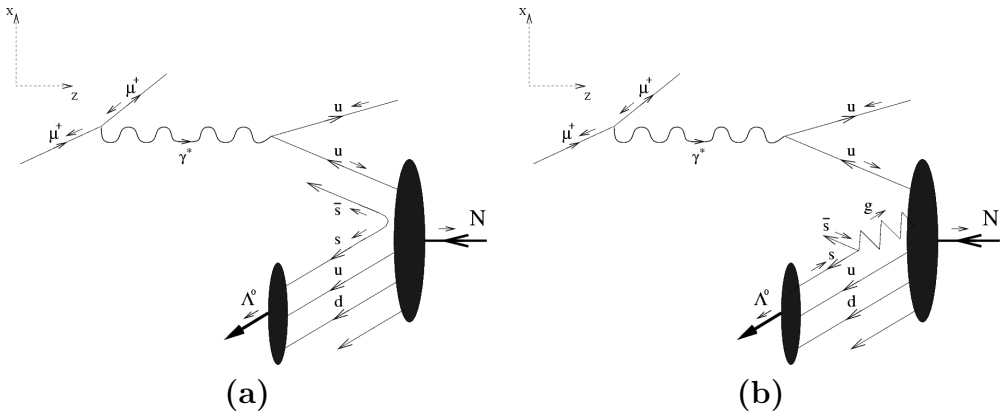

Figure 15: Expected Λ polarization for deep-inelastic μN scattering on a valence u quark. The polarization sign is opposite in the two hypotheses of strange sea-quarks polarization (a) and gluon polarization (b).

6.2 Current fragmentation region

Let us examine the case in which the virtual photon interacts with a strange sea-quark in a longitudinally polarized target. The s quark extracted from the nucleon will fragment into a strange baryon plus something else. If the s quarks are negatively polarized as suggested by the intrinsic strange sea-quark polarization model, such polarization should be reflected in the final state. The photon-quark interaction conserves the quark helicity and thus the s-quark polarization should be left unchanged in the final state, and can be inherited, at least partially, by the inclusively detected spin-half baryons in its fragmentation products [66]. Among all produced hyperons, Λ are chosen since they have the largest production cross-section and their polarization is self-analyzing from the weak decay $\Lambda \to p\pi^-$ properties.

From a general point of view the triple differential cross-section for Λ production in polarized μN DIS is given by [64, 67]:

$$\frac{d\sigma^{H_h}_{\lambda,\mu}}{dx\ dy\ dz} = \sum_{q,\lambda_q} e_q^2 q^{\mu}_{\lambda_q}(x) \frac{d\hat{\sigma}_{\lambda,\lambda_q}}{dy} D^{H_h}_{q_{\lambda_q}}(z), \tag{45}$$

where λ and μ represent the helicities of the incoming lepton and of the target nucleon, H_h is the helicity of the outgoing hadron, λ_q is the helicity of the quark of flavor q inside the nucleon. The distribution $q^{\mu}_{\lambda_q}(x)$ denotes the probability of finding, inside a nucleon of helicity μ, a quark of flavor q, helicity λ_q and carrying a fraction x of the nucleon momentum. Finally the fragmentation function $D^{H_h}_{q_{\lambda_q}}(z)$ represents the probability for a quark q with helicity λ_q to fragment into a hadron h with helicity H_h and carrying a fraction z of the quark momenta.

In the case of longitudinally polarized lepton and/or target, it is possible to build four different observables depending on the spin configuration. One is the unpolarized cross section $d\sigma^H$, while the other three, denoting with $+/-$ respectively the positive and negative helicity states, are given by

$$A_{||}^H = \frac{d\sigma_{++}^H - d\sigma_{+-}^H}{2d\sigma^H} \quad \text{(double-spin asymmetry)}, \tag{46}$$

$$P_{+0}^H = \frac{d\sigma_{+0}^{H_+} - d\sigma_{+0}^{H_-}}{d\sigma^H} \quad \text{(spin transfer from l)}, \tag{47}$$

$$P_{0+}^H = \frac{d\sigma_{0+}^{H_+} - d\sigma_{0+}^{H_-}}{d\sigma^H} \quad \text{(spin transfer from the nucleon)}, \tag{48}$$

where 0 stands for unpolarized particle. The elementary photon-quark cross sections $d\hat{\sigma}_{\lambda,\lambda_q}$, are given by

$$d\hat{\sigma}_{++} = d\hat{\sigma}_{--} = \frac{4\pi\alpha^2}{sxy^2} \tag{49}$$

$$d\hat{\sigma}_{+-} = d\hat{\sigma}_{-+} = \frac{4\pi\alpha^2}{sxy^2}(1-y)^2, \tag{50}$$

and the helicity-averaged and helicity-dependent fragmentation functions,

$$D_q(z) = D_{q+}^{H_+}(z) + D_{q+}^{H_-}(z) \tag{51}$$

$$\Delta D_q(z) = D_{q+}^{H_+}(z) + D_{q+}^{H_-}(z), \tag{52}$$

it is possible to rewrite eq. 46-48 as

$$A_{||}^H = D(y)\frac{\sum_q e_q^2 \Delta q(x) D_q^H(z)}{\sum_q e_q^2 q(x) D_q^H(z)}, \tag{53}$$

$$P_{+0}^H = D(y)\frac{\sum_q e_q^2 q(x) \Delta D_q^H(z)}{\sum_q e_q^2 q(x) D_q^H(z)}, \tag{54}$$

$$P_{0+}^H = \frac{\sum_q e_q^2 \Delta q(x) \Delta D_q^H(z)}{\sum_q e_q^2 q(x) D_q^H(z)}. \tag{55}$$

The possibility of measuring the strange sea-quark polarization Δs from Λ hyperons produced in the current fragmentation region strongly depends on the fragmentation process, described by the functions $D_q^H(z)$ and $\Delta D_q^H(z)$. In the non-relativistic parton model, where the whole spin of the Λ is carried by the s quark, we have

$$\Delta D_s(z) \neq 0, \tag{56}$$

$$\Delta D_u(z) = \Delta D_d(z) = 0. \tag{57}$$

In this case eq. 55 reduces to

$$P_{0+}^H = \frac{e_s^2 \Delta s(x) \Delta D_s^H(z)}{e_s^2 s(x) D_s^H(z)}. \tag{58}$$

The Λ polarization measurement can thus only indirectly give information on the spin-dependent quark distribution function $\Delta s(x)$, through the product with the fragmentation function $\Delta D_s(z)$. However, one could naively expect that the probability for a fragmented Λ to have the same helicity as the fragmenting s-quark is larger than for opposite helicities, and thus the sign of the Λ polarization coincides with that of $\Delta s(x)$.

The results of polarized DIS experiments on nucleon structure functions, when applied to Λ baryons, lead however to the conclusion that the s quark carries only a fraction of the Λ spin, and that u and d quarks are anti-correlated with the s-quark spin [68].

6.3 Λ production with a transversely polarized target

Longitudinal muon and target configuration, described in the previous section, allows to access the helicity distributions of quarks in the nucleon. Using transversely polarized target gives access to the transversity $\Delta_T q(x)$ which couples to transverse fragmentation function. We introduce the transverse fragmentation functions $\Delta_T D_q^H(z)$ as:

$$\Delta_T D_q^H(z) = D_{q^\uparrow}^{H^\uparrow}(z) - D_{q^\uparrow}^{H^\downarrow}(z), \tag{59}$$

where $D_{q^\uparrow}^{H^{\uparrow(\downarrow)}}(z)$ represents the probability for a quark q to fragment into an hadron carrying a fraction z of the quark momentum and with the spin aligned (anti-aligned) with the transverse spin of the quark.

Equation 45, written for the case of unpolarized incoming lepton and transversely polarized nucleon, leads to the following expression for the transverse polarization of the outgoing Λ:

$$P_\Lambda^T = P_T D_{NN}(y) \frac{\sum_q e_q^2 \Delta_T q(x)\ \Delta_T D_q^H(z)}{\sum_q e_q^2 q(x)\ D_q^H(z)}, \tag{60}$$

where P_T is the target transverse polarization. The factor $\hat{D}_{NN}(y)$ takes into account the spin dependence of the elementary photon-quark interaction:

$$D_{NN}(y) = \frac{d\hat{\sigma}^{lq^\uparrow \to lq^\uparrow} - d\hat{\sigma}^{lq^\uparrow \to lq^\downarrow}}{d\hat{\sigma}^{lq^\uparrow \to lq^\uparrow} + d\hat{\sigma}^{lq^\uparrow \to lq^\downarrow}} = \frac{2(1-y)}{1+(1-y)^2}. \tag{61}$$

In the polarized SIDIS, the quantities $\Delta_T q(x)$ can only be measured together with the transversity fragmentation functions $\Delta_T D_q^H(z)$. For this reason, additional informations on the $\Delta_T D_q^H(z)$ functions are needed in order to extract the $\Delta_T q(x)$ distribution functions. Such information can be extracted from the data coming from the $pp^\uparrow \to \Lambda^\uparrow X$ reaction, and the combined measurements of the $pp^\uparrow$ and μN interactions can lead to the $\Delta_T q(x)$ measurement.

7 Extraction of the Λ^0 polarization

The measurement of the transverse spin quark distribution functions $\Delta_T q(x)$ is an important part of the physics program of the COMPASS experiment at CERN. The transversity distributions, being chiral-odd objects, are only accessible in semi-inclusive deep inelastic scattering. The most promising channels for the measurement of the transversity distributions are the Collins effect, the Drell-Yan scattering and the spin transfer to the Lambda hyperons. Here will be adopted the semi-inclusive Lambda production mechanism, showing the connection between the measured polarization and the $\Delta_T q(x)$ functions. An expression for the experimental $\Lambda^0 \to p\pi^-$ angular distribution that is at first order independent of the experimental acceptance will be derived, and the preliminary results for the Lambda polarization as a function of the x Bjorken variable will be presented. The analysis is based on the available 2002-2004 COMPASS data with transverse spin target configuration.

A very important part for the analysis is the structure of the COMPASS target, the design of which gives us the possibility for applying the acceptance canceling method.

7.1 COMPASS spectrometer target description

The measurement program requires both a polarized beam and a polarized target. The data used in this analysis were taken using solid ^6LiD as target material. The smallness of the nuclear magneton does not allow to polarize the nucleons directly by Zeeman splitting, because even for strong magnetic fields of several Tesla the interaction energy of the hyperfine splitting is much lower than the thermal energy at temperatures realizable at moderate cost, which are in the order of some hundred mK. In COMPASS the target material is polarized via Dynamic Nuclear Polarization (DNP) [69] using two separate microwave systems.

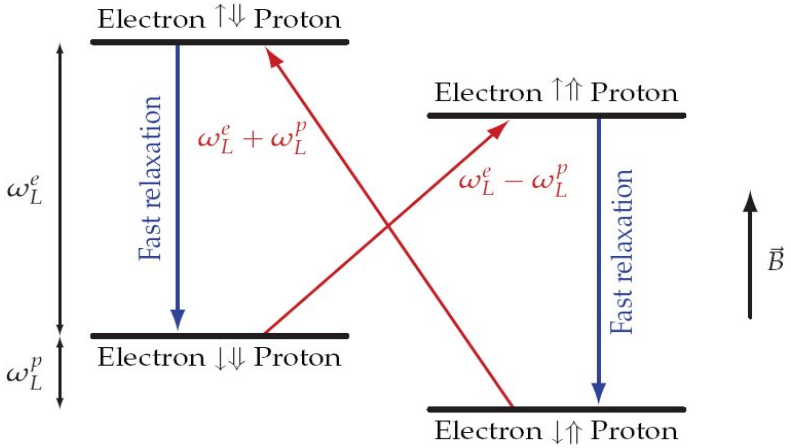

Figure 16: Dynamic nuclear polarization in an electron-proton spin system: In a strong external magnetic field B the energy level of the electron splits into four levels, which correspond to the different possible spin alignments of the electron (↑) and the proton (⇑). (from [70])

The simplest possible system that may be subject to dynamic nuclear polarization

consists of an electron spin $\uparrow$ and a proton spin $\Uparrow$. In a strong external magnetic field the energy level of the electron is split into two pairs of levels (see fig. 16). The separation of the two pairs is given by the Larmor frequency of the electron's magnetic moment w_L^e ,which is nearly three orders of magnitude larger than the splitting of the two upper and lower levels, that is determined by the Larmor frequency w_L^p of the magnetic moment of the proton. At temperatures below 1 K only the lower two states, in which the electron spin is aligned opposite to the external magnetic field, are populated. By irradiating the material with resonant microwaves of the frequency $w_L^e + w_L^p(w_L^e - w_L^p)$ transitions $|\downarrow\Uparrow\rangle \rightarrow |\uparrow\Downarrow\rangle$ ($|\downarrow\Downarrow\rangle \rightarrow |\uparrow\Uparrow\rangle$) can be induced in which both spins are flipped. The electron spin relaxes after a short period of the order of milliseconds, whereas the relaxation time of the proton is about 10^6 times larger. This leads to an increased population of one of the lower energy levels and thus to a negative (positive) polarization of the proton.

The simplified scenario described above does not explain why the actually forbidden double spin-flip transitions are feasible. The reason is, that due to a dipole-dipole interaction of the protons and the electrons, the so-called "solid effect", the pure states are mixed, so that each level contains contributions from both proton spin alignments.

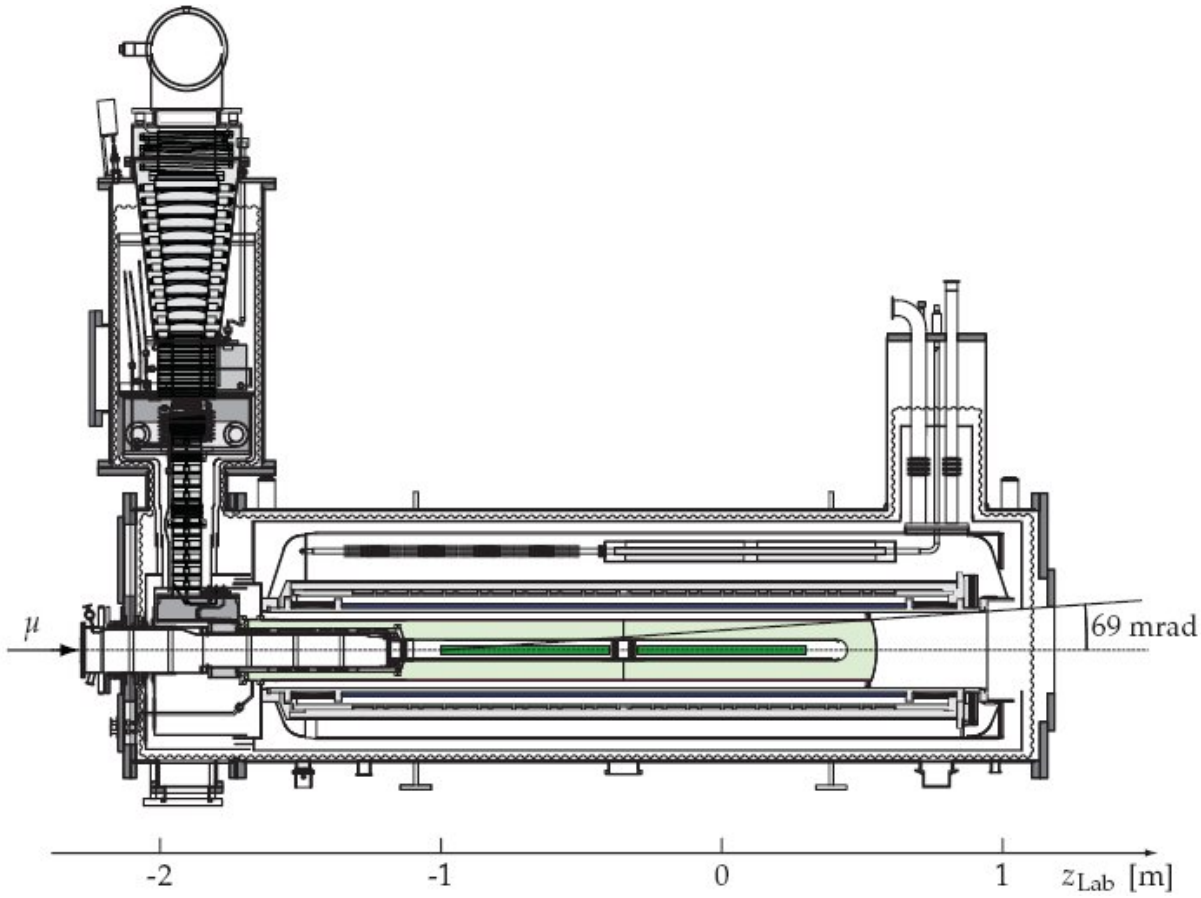

Figure 17: Side view of the COMPASS polarized ^6LiD target. The components relevant for this analysis are colored: the two target cells in green, surrounded by the microwave cavity in light green and the solenoid in blue plus the dipole magnet in red. (from [71])

Until 2004 COMPASS used the target magnet system of the SMC experiment (see fig. 17). The microwaves polarize paramagnetic centers[3] in the target material, which

transfer their polarization with the help of the DNP mechanism to the polarizable nucleons. The nucleons of the atoms around the paramagnetic centers are polarized by spin diffusion, due to spin-spin interactions of the nuclei.

To build up and sustain the polarization, the target material is surrounded by a superconductive solenoid which creates a very homogeneous field of 2.5 T. Thermal relaxation is avoided by cooling the ^6LiD down to temperatures of 80 to 100mK using a $^3He - ^4He$ dilution refrigerator. At this low temperatures the target operates in the so-called frozen spin mode with relaxation times larger than 1000 h. The polarization is measured by means of Nuclear Magnetic Resonance (NMR) and it usually exceeds the design value of 50%. The target is split up into two cylindrical cells each 60 cm long with a diameter of 3 cm (see fig. 17). The cells are polarized in opposite directions, so that both relative alignments of target and beam polarization are measured at the same time. To neutralize the effect of different acceptances of the up and downstream target cells, the target polarization is inverted every 8 h. Additional systematic influences of the solenoid field are suppressed by reversing the orientation of the target cell polarization with respect to the direction of the solenoid field in larger time intervals, which is done by exchanging the microwave frequencies in the two cells. The data taking is organized in a way that all possible combinations of polarization and field direction are of equal statistics. In order to be able to invert the direction of the polarization an additional dipole magnet with a maximum transverse field of 0.5 T in vertical direction is integrated into the target. The fields of the solenoid and the dipole magnet are ramped in a coordinated way, so that the total field vector is slowly rotated by 180° taking along the target spins. The dipole magnet is also used to keep the target in transverse polarization, which is needed for the transversity measurements.

In future measurements with NH_3 as target material (proton target) are planned, which in combination with the ^6LiD data (deuteron target) will allow to extract information about the neutron spin structure.

7.2 The selection cuts

The event selection is based on the requirement to have a scattering with large momentum transfer ($Q^2 > 1GeV^2/c^2$) in the ^6LiD target material, together with a two-body charged decay of a neutral particle downstream of the target. The reconstructed position of the primary interaction vertex must be within the geometrical volume occupied by the target material. In order to ensure an equal beam flux in both target cells, the extrapolated beam trajectory must not intersect the cylindrical surfaces of the cell volumes.

The Λ hyperons undergo the decay $\Lambda^0 \to p\pi^-$ in about 63% of the cases. The decay is detected as a V-shaped vertex in the reconstructed events, with the two oppositely charged decay particles bent in opposite directions by the spectrometer magnets. The typical decay length at the COMPASS energies is about 250 cm.

The main sources of background in the Λ^0 sample come from K^0 decays, photon conversion and fake vertices from accidental track associations. The background is significantly reduced when the longitudinal position of the decay vertex is restricted to a region between the target exit window and the first MicroMega station. This corresponds to an average separation between the Lambda production and decay vertices of about 70

[3]Impurities with a single valence electron.

cm. The contamination of e^+e^- pairs from photon conversions is significantly reduced by requiring a minimal transverse momentum $p_T > 23$ MeV/c of the decay proton with respect to the decaying hyperon. All the contributions to the background may be seen on the Armenteros plot(Fig.18). Here the abscissa value is $\alpha = \frac{p_+ - p_-}{p_+ + p_-}$ and the ordinate is p_T, where p_+ and p_- are the momentums of the positively and negatively charged products of the Λ^0 decay and p_T is the component perpendicular to the Λ^0's momentum direction in the Lab frame. One can clearly see the K^0_S decays and the band on the bottom from the photon conversion.

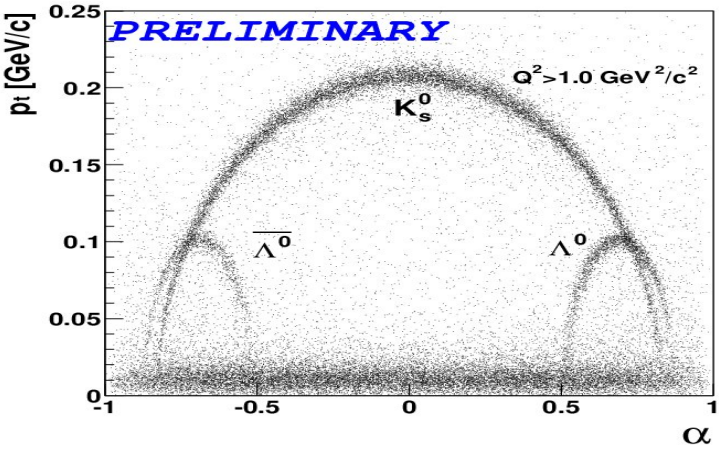

Figure 18: *The Armenteros plot.*

The background is further reduced when a cut on the collinearity between the Lambda momentum vector and the line connecting the primary and decay vertex is applied. The angle between the two vectors must be lower than 10 mrad.

Only events with a reconstructed Lambda invariant mass between $M_\Lambda^{PDG} - 0.35$ and $1.35 - M_\Lambda^{PDG}$, where M_Λ^{PDG} is the PDG value of the Lambda mass, are kept in the final event sample used for the polarization calculation. The number of Lambda decay events in the sample are estimated by fitting the invariant mass distribution with a Gaussian peak combined with a 3rd degree polynomial for the background parameterization. The mass range includes a significant fraction of the background on both sides of the Lambda peak.

The overall number of detected Lambda decays in the sample used in the analysis, corresponding to the full transversity data collected by the experiment in the years 2003 and 2004, is about 20000.

Summarizing once more time the cuts applied to the data sample are:

- The cut on the primary vertex position is $-100 < z_v < -40$ cm, $-30 < z_v < 30$ cm, with the radial distance from the beam line $r < 1.4$ cm.
- To ensure in first approximation an equal flux through the two target cells one selects event where the beam track go through both cells.
- To have a good kinematics reconstruction and to be sure about the primary vertex position one asks that the scattered particle(μ') go traverses at least $30X_0$. This also

gives the additional assurance that there was no mistake in the track association and the outgoing particle is effectively a muon.

- We select a V^0 vertex of the Λ^0 that is out of the target material and is before the first trackers to ensure a good precision in the reconstruction and avoid a possible multiple scattering of the products in the target material.

- The collinearity of the Λ^0 to the direction of the virtual photon is to be better than 10 mrad. This cut is performed by the reconstruction of the four momentum of the Λ^0 and of the virtual γ.

- To have a secure separation by charge and a good measurement of the impulses of the decay products from the V^0 vertex we applied a cut on the position of the last detected point of theirs tracks to be after the first spectrometer magnet. So $z_{last} > 350$ cm for both decay particles.

- To be in the "sensitive" range of impulses of the COMPASS spectrometer we ask that the impulses of both decay particles to be > 1 GeV.

- We have the possibility to cut off the background contribution from the $\gamma \to e^+e^-$ conversion by cutting out $p_T < 1$ GeV in the Armenteros plot (see Fig. 18).

- To further higher the quality of the data we apply the cut $0.1 < y < 0.9$ where $y = \frac{\nu}{E}$ is the part of the initial μ transfered to the virtual γ.

- For the 2004 year data it was possible to implement a bad spill selection.

7.3 The method

The angular distribution of the decay proton in the Lambda rest frame, measured in the experiment, is given by:

$$\frac{dN}{d\Theta_T^*} = N_0 \cdot (1 + \alpha P_T^\Lambda \cos(\Theta_T^*)) \cdot Acc(\Theta_T^*) \tag{62}$$

The $Acc(\Theta_T^*)$ function represents the distortion of the theoretical angular distribution introduced by the experimental apparatus. This distortion is usually corrected by combining real data and MonteCarlo (MC) simulations. This approach is however quite sensitive to the accuracy of the MC description of the experiment, and requires huge MC data samples to get a good statistical accuracy.

Also one can use the usual acceptance correction methods for a single sell target. In the polarization extracting experiments one could rely on the assumption of some apparatus symmetry. It can be illustrated by the use of an up/down spectrometer symmetry assumption for Λ polarization extraction.

If we consider the situation depicted on Fig. 19 and one want to extract the decay asymmetry $\epsilon_n(\Theta^*) = \alpha P_n \cos\Theta^*$ where the axis n is defined as $\vec{n} = \vec{p}_{\gamma^*} \times \vec{p}_\Lambda$. We see that there is a correspondence between a decay to the upper acceptance region and a decay in the lower one that are exprimed by eq. 63, where subscripts U are for the up acceptance and D for the down one correspondingly.

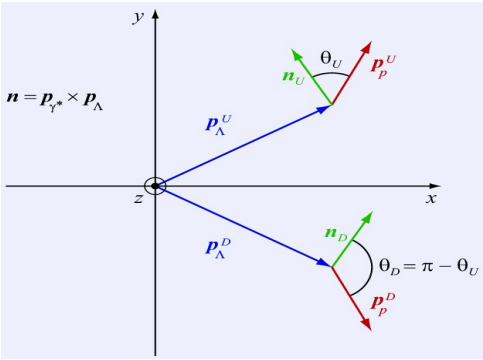

Figure 19: *Standard acceptance symmetry.*

$$A_U \cos\Theta^* = A_D \cos(\pi - \Theta^*) \tag{63}$$

If we consider the mentioned hypothesis of the up/down acceptance equivalence and assume the counting rates as shown in the eq. 64 and eq. 65. We can compose an acceptance canceling relation.

$$U_\pm = \frac{N_0^U}{2} A_U(\pm\cos\Theta^*)(1 \pm \alpha P_n \cos\Theta^*) \tag{64}$$

$$D_\pm = \frac{N_0^D}{2} A_D(\pm\cos\Theta^*)(1 \pm \alpha P_n \cos\Theta^*) \tag{65}$$

The main point of such a relation will be to cancel A_U and A_D acceptance contributions using the assumption of eq. 63. The obtained equation would be:

$$\epsilon_n(\Theta^*) = \frac{\sqrt{U_+ D_+} - \sqrt{U_- D_-}}{\sqrt{U_+ D_+} + \sqrt{U_- D_-}} = \alpha P_n \cos\Theta^* \tag{66}$$

This method is effective but it is hard to realize an exact equivalence of acceptance in an experimental environment.

In the analysis presented here we used a technique based only on real data samples, exploiting some of the symmetries of the experimental apparatus. The technique is based on the combination of two data taking periods, in the same experimental conditions but in our case having a two cell target setup we can use opposite target cell polarization orientations. Under general assumptions on the existing symmetries, the acceptance functions are canceled and only the terms proportional to the true polarization of the Λ will remain.

We will denote with $Acc_{1(2)}^{+(-)}(\Theta_T^*)$ the acceptance for Λ coming from the target cell with spin orientation +(-), data taking period 1(2), and emitting a proton with an angle Θ_T^* in the Lambda rest frame. We can draw schematically the target cells and theirs polarizations during different data taking periods (see Fig.20).

We can write the number of Λ emitting the proton during the decay at an angle Θ_T^* with respect to its spin vector S in the Λ rest frame as is given in the eq. 67.

$$N_{1(2)}^{+(-)}(\Theta_T^*) = \Phi_{1(2)}^{+(-)} \cdot \left(\frac{d\sigma}{d\Omega}\right)^0 \cdot \left(1 + \alpha P_\Lambda^{+(-)} \cos(\Theta_T^*)\right) \cdot Acc_{1(2)}^{+(-)}(\Theta_T^*) \tag{67}$$

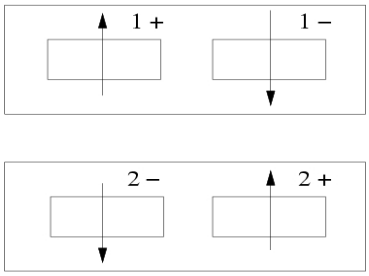

Figure 20: *Cells during different time periods.*

The equation 67 is depicting the four possible configurations that will be used in the acceptance canceling method. The main point is to define the minimum amount of strong symmetry criterion, that are necessary for the method. First we will assume that the target polarization is constant through the time(eq. 68), that is due to the fact that the spin rotations are done on a much smaller time scale than the target cell polarization decay.

$$P_T^1 = P_T^2 \tag{68}$$

Then we need to make the assumption on the invariance of the experimental acceptance for each target cell during the different time periods. In our case we require only the simply equivalence without any assumption about the spectrometer symmetry. So we have the eq. 69 and eq. 70 for our target cells.

$$Acc_1^+(\Theta_T^*) = Acc_2^-(\Theta_T^*) \tag{69}$$

$$Acc_1^-(\Theta_T^*) = Acc_2^+(\Theta_T^*) \tag{70}$$

The last needed assumption is on the muon flux. We have the beam flux relations as shown in eq. 71.

$$\Phi_1^+ \cdot \Phi_2^+ = \Phi_1^- \cdot \Phi_2^- = \Phi_1 \cdot \Phi_2 \tag{71}$$

Under the mentioned quite general assumptions we can construct the following counting rate asymmetry (eq. 72). That will cancel out the apparatus acceptance effects.

$$\epsilon_T(\Theta_T^*) = \\ = \frac{\left[\sqrt{\frac{N_1^+(\Theta_T^*)}{\Phi_1^+}\cdot\frac{N_2^+(\Theta_T^*)}{\Phi_2^+}} + \sqrt{\frac{N_1^-(\pi-\Theta_T^*)}{\Phi_1^-}\cdot\frac{N_2^-(\pi-\Theta_T^*)}{\Phi_2^-}}\right] - \left[\sqrt{\frac{N_1^+(\pi-\Theta_T^*)}{\Phi_1^+}\cdot\frac{N_2^+(\pi-\Theta_T^*)}{\Phi_2^+}} + \sqrt{\frac{N_1^-(\Theta_T^*)}{\Phi_1^-}\cdot\frac{N_2^-(\Theta_T^*)}{\Phi_2^-}}\right]}{\left[\sqrt{\frac{N_1^+(\Theta_T^*)}{\Phi_1^+}\cdot\frac{N_2^+(\Theta_T^*)}{\Phi_2^+}} + \sqrt{\frac{N_1^-(\pi-\Theta_T^*)}{\Phi_1^-}\cdot\frac{N_2^-(\pi-\Theta_T^*)}{\Phi_2^-}}\right] + \left[\sqrt{\frac{N_1^+(\pi-\Theta_T^*)}{\Phi_1^+}\cdot\frac{N_2^+(\pi-\Theta_T^*)}{\Phi_2^+}} + \sqrt{\frac{N_1^-(\Theta_T^*)}{\Phi_1^-}\cdot\frac{N_2^-(\Theta_T^*)}{\Phi_2^-}}\right]} \tag{72}$$

The counting rate asymmetry (eq. 72) is in our case proportional to the Λ^0 polarization P_T.

$$\epsilon_T(\Theta_T^*) = \alpha P_\Lambda^S \cos\Theta_T^*, \tag{73}$$

The eq. 73 tells us that if we construct the counting rate asymmetry distribution $\epsilon(\cos\Theta_T^*)$ for different $\cos(\Theta^*)$ points it will have a slop fitting which one can extract the Λ polarization value P_T.

To demonstrate the procedure one can have a look at the fig. 22 and fig. 21 that represent the Λ invariant mass distribution respectively for 2 and 8 bins in $\cos(\Theta_T^*)$ the fit of the mass spectrums is used to extract the quantity's entering then-after in the polarization calculation.

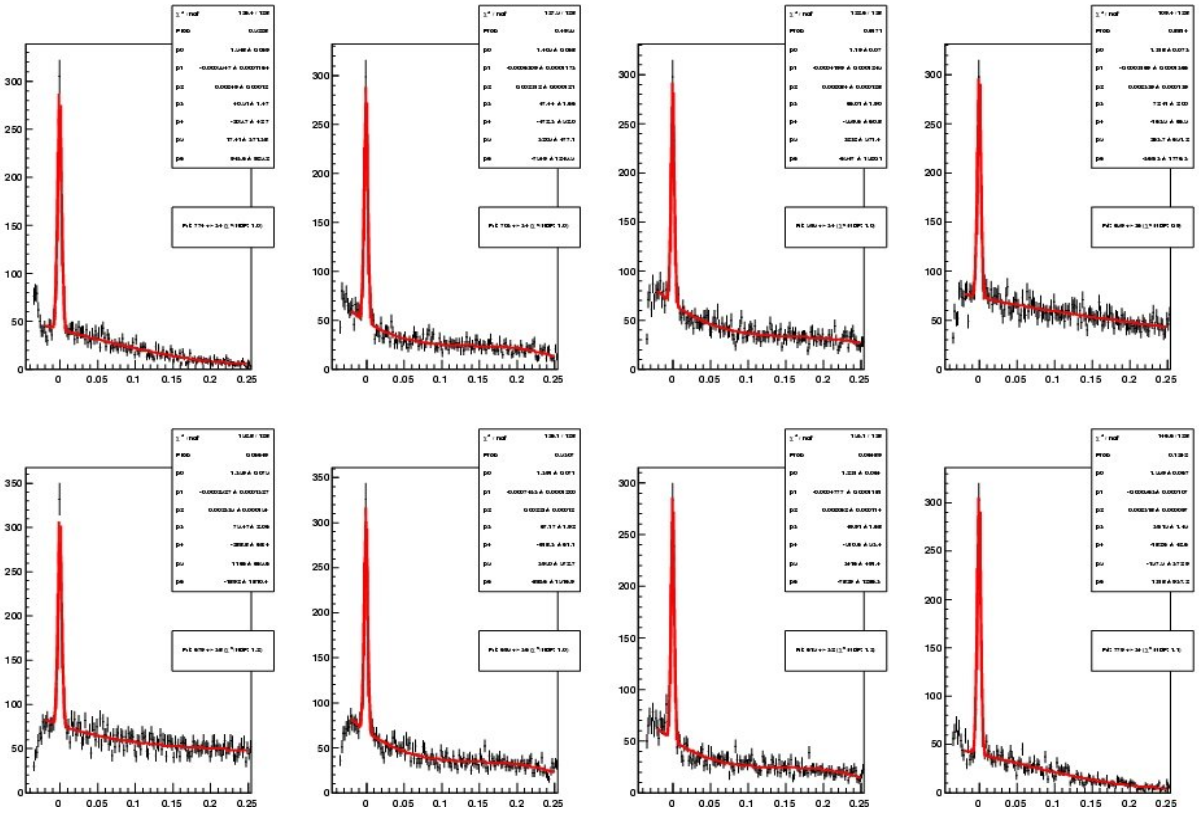

Figure 21: *8 Bins in* $\cos(\Theta_T^*)$ *plot.*

From the statistical fluctuation of the bins content in the figures 22 and 21 we clearly see that the event numbers decrease drastically with the shrinking of the binning. For all the presented results was used the approximation of two bins in the $\cos\Theta_T^*$ space as shown in the fig. 23.

If only two bins in the proton decay angle Θ_T^* distributions are considered we will have a simplification in the equations 67. We can now write the number of Λ emitting the proton during the decay at an angle Θ_T^* for different cells and periods as in eq. 74-77.

$$N_{1(2)}^{+}(D) = \int_{-1}^{0} \frac{N_{Tot}^{1(2),+}}{2}(1 + \alpha P_\Lambda^S \cos\Theta_T^*) \cdot Acc_{1(2)}^{+}(\cos\Theta_T^*) d\cos\Theta_T^* =$$

$$= \frac{N_{Tot}^{1(2),+}}{2}(1 - \frac{\alpha P_\Lambda^S}{2}) Acc_{1(2)}^{+}(D) \tag{74}$$

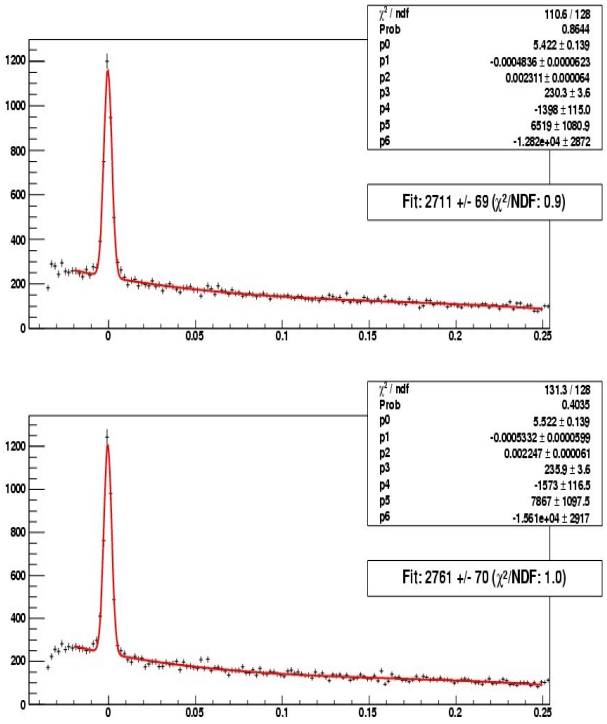

Figure 22: *2 Bins in cos(Θ^*_T) plot.*

$$N^{+}_{1(2)}(U) = \int_0^1 \frac{N^{1(2),+}_{Tot}}{2}(1 + \alpha P^S_\Lambda \cos\Theta^*_T) \cdot Acc^{+}_{1(2)}(\cos\Theta^*_T) d\cos\Theta^*_T = \\ = \frac{N^{1(2),+}_{Tot}}{2}(1 + \frac{\alpha P^S_\Lambda}{2}) Acc^{+}_{1(2)}(U) \quad (75)$$

$$N^{-}_{1(2)}(D) = \int_{-1}^0 \frac{N^{1(2),-}_{Tot}}{2}(1 - \alpha P^S_\Lambda \cos\Theta^*_T) \cdot Acc^{-}_{1(2)}(\cos\Theta^*_T) d\cos\Theta^*_T = \\ = \frac{N^{1(2),-}_{Tot}}{2}(1 + \frac{\alpha P^S_\Lambda}{2}) Acc^{-}_{1(2)}(D) \quad (76)$$

$$N^{-}_{1(2)}(U) = \int_0^1 \frac{N^{1(2),+}_{Tot}}{2}(1 - \alpha P^S_\Lambda \cos\Theta^*_T) \cdot Acc^{-}_{1(2)}(\cos\Theta^*_T) d\cos\Theta^*_T = \\ = \frac{N^{1(2),-}_{Tot}}{2}(1 - \frac{\alpha P^S_\Lambda}{2}) Acc^{-}_{1(2)}(U) \quad (77)$$

In this case we see that the equation 72 simplifies to $\epsilon_T = \alpha P_T/2$ and we gain a direct access to the extraction of the polarization without the necessity to perform a fitting procedure and having a better statistical filling of the analyzed bins.

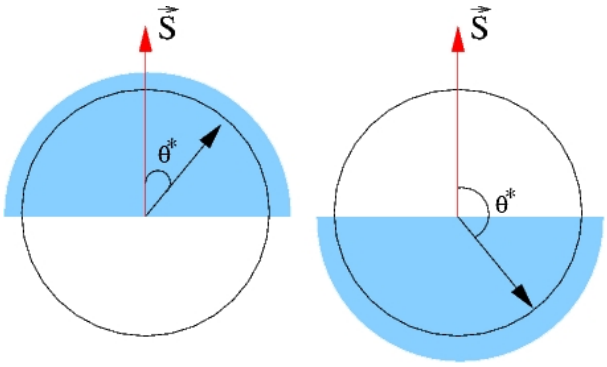

Figure 23: *2 Bins division of the* Θ_T^*.

7.4 Cross-check

To guarantee the good data quality and a major security of the results a complete cross-check of the analysis procedure was performed on the whole analyzed data. At the present state the data sample that was cross-checked was divided in two subsamples in Q^2, one for all Q^2 and the other or $Q^2 > 1$ GeV.

For both samples a bin by bin difference between the invariant Λ mass histograms of the two analysis was calculated. The resulting difference was found to be less than 10 events on the whole spectra so an agreement between the analysis is clear.

The resulting bin by bin differences for all Q^2 data sample are summarized in the Fig. 24 where the results for different data taking periods are given.

The same resulting bin by bin differences summary for the $Q^2 > 1$ data sample over all the analyzed periods are presented in Fig. 25.

After the invariant mass spectra cross-check in different $\cos\Theta_T^*$ bins was performed and it was concluded that in the data selection(application of the various cut over the initial data sample) part of the analysis giving a same output in both independent approach is correct. Was decided to cross-check the Λ polarization extraction part. For that purpose once again two situations were examinated. In one case the data sample consisted of events with all Q^2, and in the other a cut of $Q^2 > 1$ GeV was applied. The resulting figures for some data taking periods and the summarizing one for the whole statistic of the uncut all Q^2 data sample are shown in Fig. 26.

Those results of the cross-check shows that we effectively have a very good agreement between the two independent analysis on the whole data sample and it can be concluded that the application of the cuts to the data and the implementation of the Λ polarization extraction method through the counting rate asymmetry $\epsilon_T = \alpha P_T/2$ that is realized in the analysis are correct.

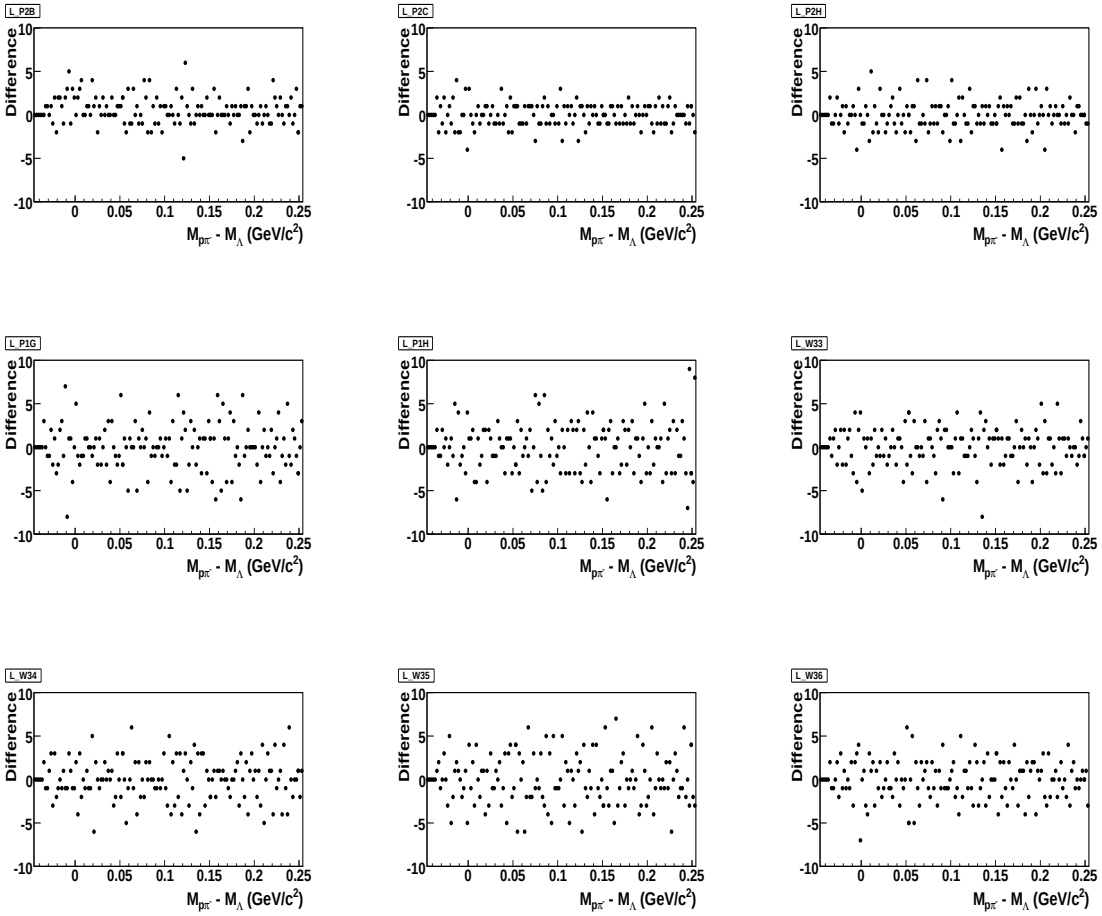

Figure 24: All Q^2 invariant mass cross-check.

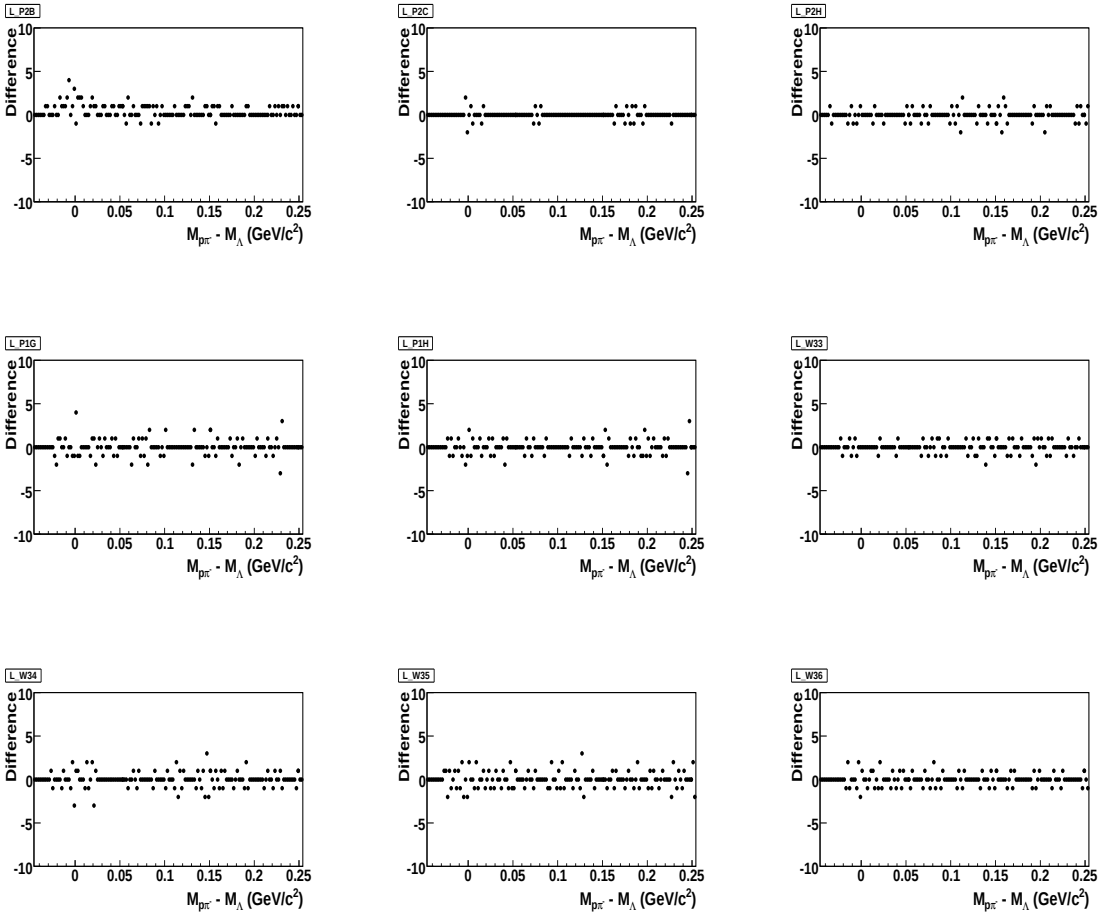

Figure 25: $Q^2 > 1$ GeV invariant mass cross-check.

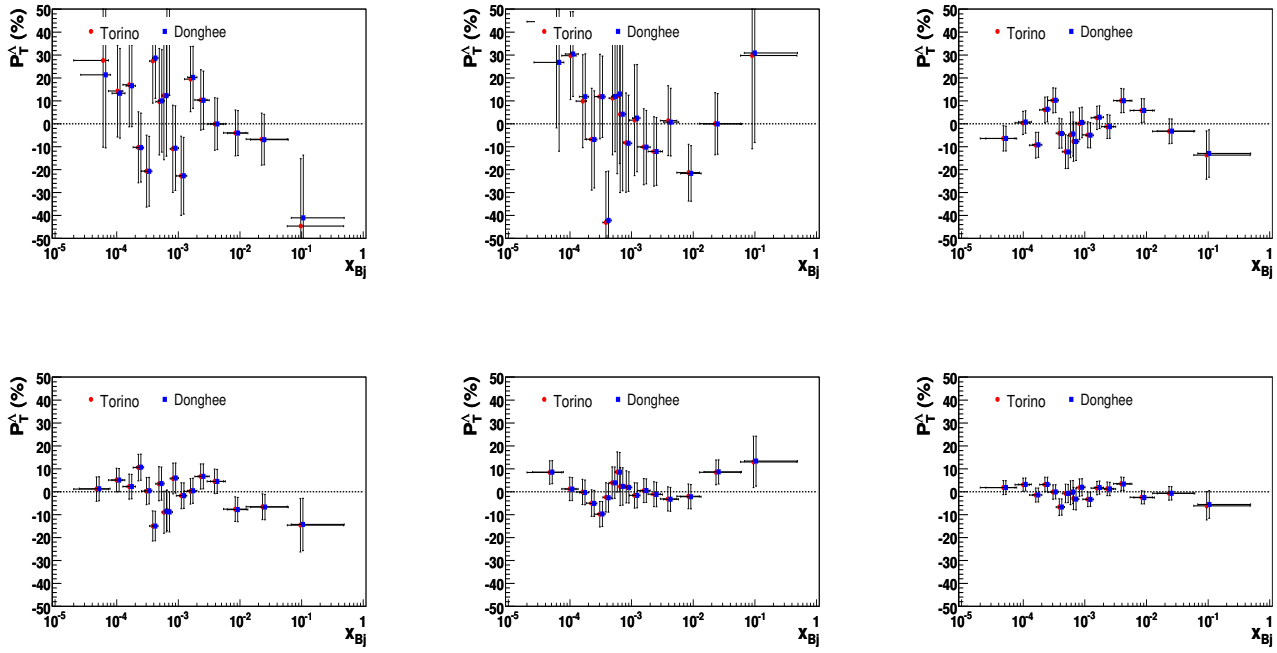

Figure 26: All Q^2 polarization cross-check.

7.5 Estimation of the systematic error

A very difficult question is the correct estimation of the systematic error in our present measurements. To do such an estimation we applied several different methods of analysis. All of them address different possible configurations where the extracted Λ polarization after the extraction should result to be zero. Then analyzing the results of the application of our polarization extraction method, we can evaluate possible systematic error contribution. The studied configurations for the present analysis are:

- Random polarization axis (R). In this case at each event analysis instead of selecting the proper target polarization axis we choose one randomly, such a selection should produce resulting null polarization after the extraction.
- The polarization axis rotated by 90 degree with respect to the beam axis. This will introduce in the analysis a polarization that is perpendicular to the real one, and should therefor produce a null extracted polarization.
- Analysis of one target cell divided in to two parts instead of the two target cells with opposite polarization. This approach uses the fact that in our analysis procedure it is intended that we use two cell with opposite polarization, and the analysis of two cells(two parts of one cell) should give null result
- Analysis of one data taking period divided in to two parts instead of two data taking periods. This assumption as the previously mentioned method uses the fact that the present analysis to avoid acceptance issues always uses two data taking periods with different cell polarization. So dividing one period(where the polarization of the cells is constant) in to two parts should also produce a null result of the polarization extraction method.

The "Random polarization axis" analysis result is shown in the Fig. 27 where the P_R coordinate shows the extracted polarization value. We see that being mainly in agreement with zero some of the points are nevertheless off by a value bigger than the expected statistical error for the corresponding bin.

For the analysis with the polarization axis being rotated by 90 degree with respect to the beams real one, we will call this axis S-axis, the resulting extracted polarization is presented in the Fig. 28. Here also we have the majority of the data points compatible with zero polarization but there are also points that will contribute in our estimation of the systematic error.

The analysis of the configuration with one target cell with the same polarization splinted into two part and given to the analysis algorithm as being two cell with different polarizations is also a good probe for eventual systematic deviations in our polarization extraction approach. If we look at the results on the Fig. 29 it is clear that even the presence of some deviated from zero data points does not indicate signs of an systematic asymmetry.

The last performed check of the method implementation by "input tweaking" in the search for an evaluation of the systematic errors was the analysis of one single data taking period in which the target sells polarizations were the same divided in two. In this case the analysis chain receive a completely wrong input. The alternative data taking period

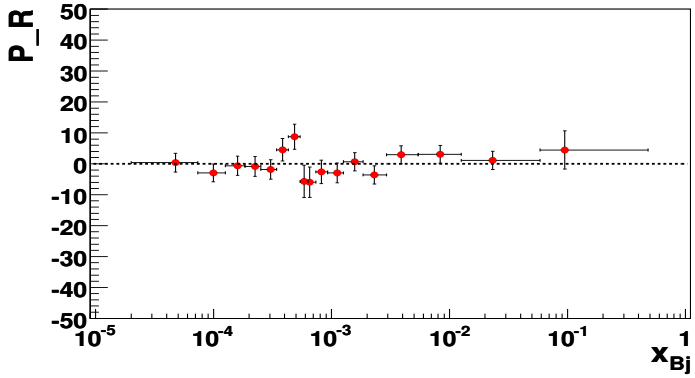

Figure 27: *R axis analysis.*

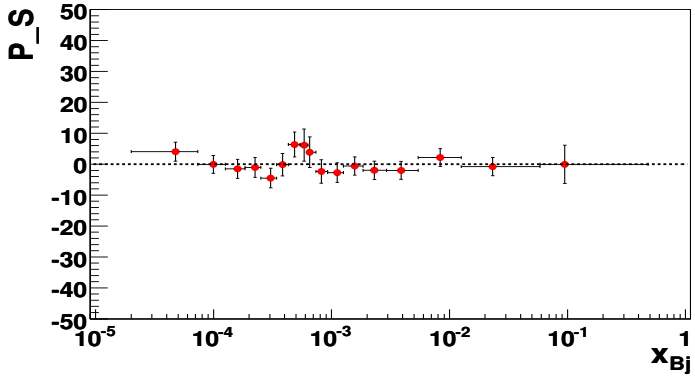

Figure 28: *S axis.*

analysis result is presented in the Fig. 30. Once again we can conclude that the data does not present indications of a systematic effect but some points will contribute to our evaluation.

Summarizing this analysis of the systematic error contribution of our polarization extraction method we can plot the sum of all observed deviation from zero in our polarization figures as a histogram. We could expect it to have a gaussian form centered over zero and the variance of the distribution should gives us an first approximation estimate of the systematic error present in the analysis. This histogram is shown on the Fig. 31. We see that as it was expected it is effectively centered on zero with the $\sigma \approx 1$.

Ultimately to estimate the errors that may be introduced by the analysis method internal realization, we also have checked the influence of a different $\cos\Theta^*_T$ binning in the procedure. For that purpose we did the analysis dividing the $\cos\Theta^*_T$ space in 4 bins instead of the standard 2 bins. The outcome of this comparison is presented in the Fig. 32. Some discrepancy is mainly due to the fact that as it was already mentioned the 2 bin method does not require any fitting, but the 4 bin approach need it and due to a reduced

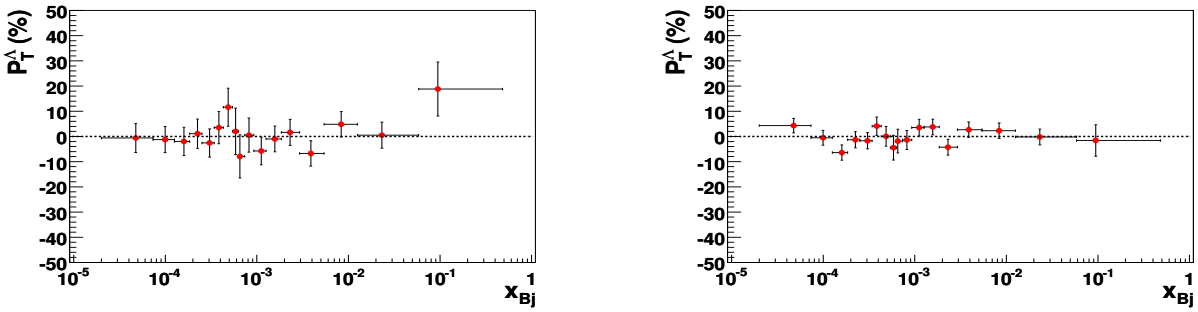

(a) (b)

Figure 29: Polarization extraction for the upper cell division(a), and for the downstream cell division(b).

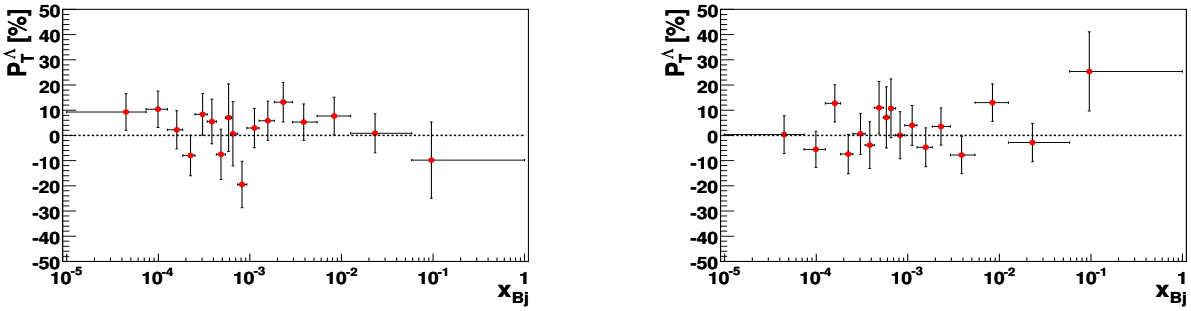

(a) (b)

Figure 30: Polarization extraction for the W33 period(a), and for the W34 period(b).

statistic such a fitting procedure introduce itself some uncertainty to the result.

The conclusion is that our present systematic error is still less that the present statistic error. The Fig. 33 demonstrate that result where the statistical error is given by the error bars on the points and our systematic error estimation is shown as a bar on the bottom of the picture.

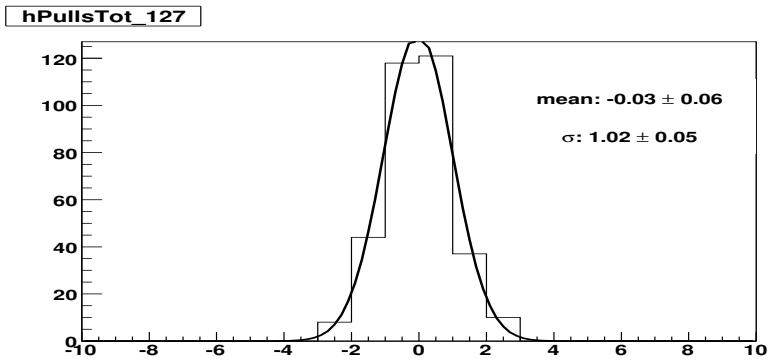

Figure 31: *Pulls from null polarization value.*

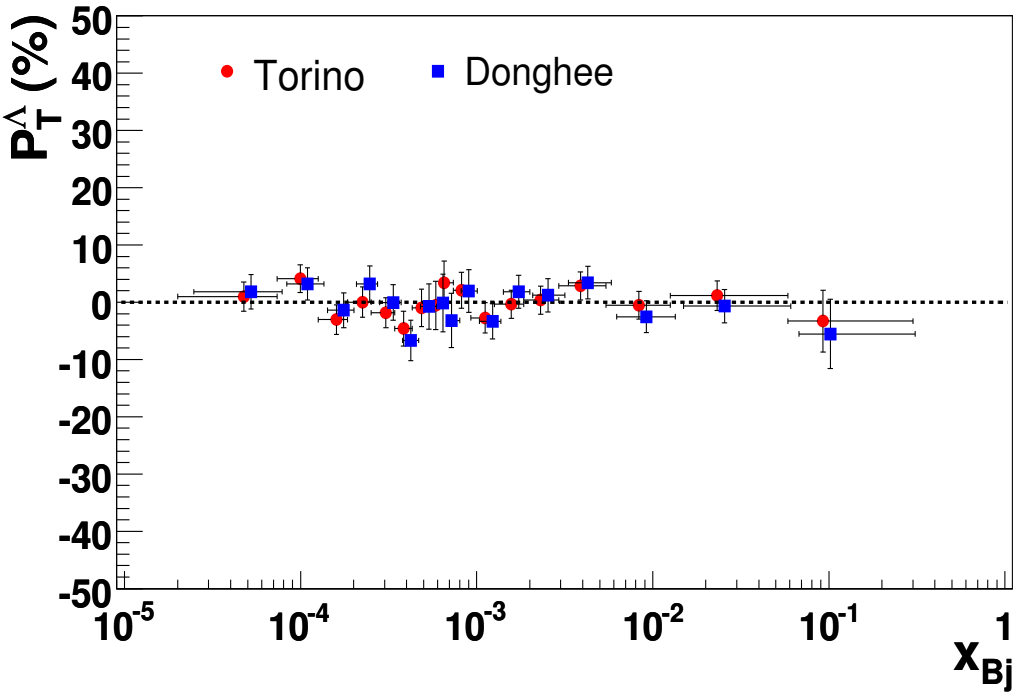

Figure 32: *2 bin vs 4 bin configuration.(Torino-4 bins, Dongee-2 bins).*

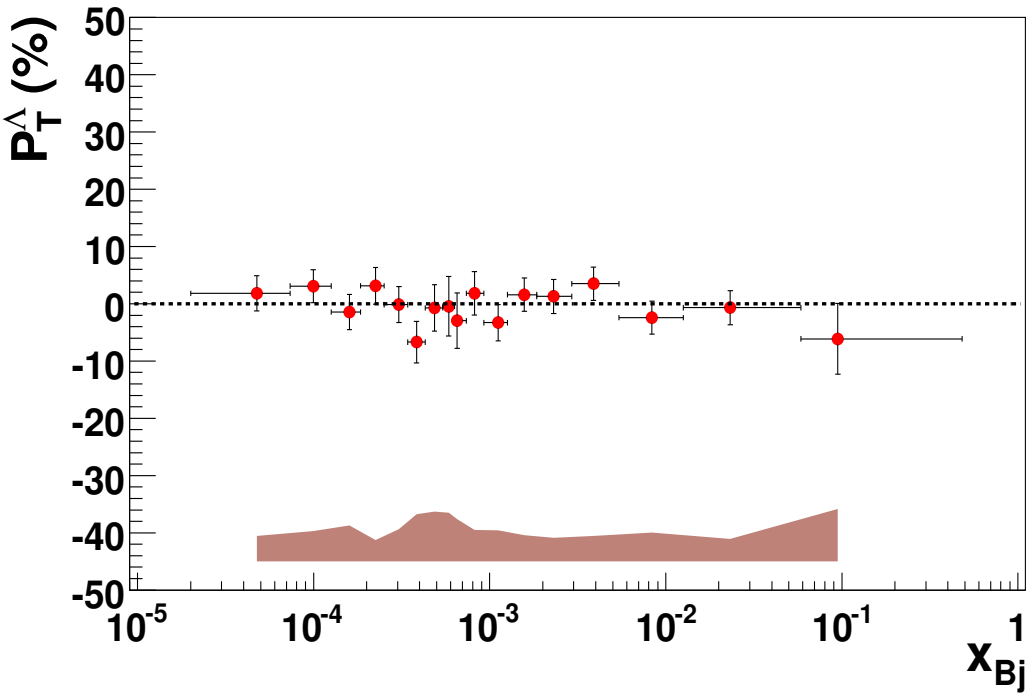

Figure 33: *The systematic error estimation superimposed to the extracted polarization.*

7.6 Theoretical estimates

Some estimates of Λ polarization were made in [72]. For Λ production in the current fragmentation region along the virtual photon direction, the transverse spin transfer to the to the transversely polarized Λ is written as

$$\hat{A}^{\Lambda}(x,z) = \frac{\sum_q e_q^2 \Delta_T q(x) \Delta_T D_{\Lambda/q}(z)}{\sum_q e_q^2 q(x) \Delta_T D_{\Lambda/q}(z)} \tag{78}$$

for charged lepton DIS on a transversely polarized nucleon target. Using model estimates for Λ hyperon fragmentation function and transvetsity distribution function the estimated upper limit from Ref. [72] for COMPASS kinematics ($x \approx 0.1$) reads:

$$\frac{1}{2}(\hat{A}_p^{\Lambda} + \hat{A}_n^{\Lambda}) \simeq 0.075 \tag{79}$$

Thus using the P_{Λ}^T definition (see eq. 42) the expected transverse Λ polarization for COMPASS conditions is

$$P_{\Lambda}^T = f P_T D_{NN}(< y >) \cdot \frac{1}{2}(\hat{A}_p^{\Lambda} + \hat{A}_n^{\Lambda}) \simeq 1\% \tag{80}$$

where $f = 0.45$ is the target dilution factor, $P_T = 0.5$ is the target transverse polarization and the depolarization factor $D_{NN}(< y >) = 0.8$ for the COMPASS kinematics with $< y >= 0.48$.

7.7 Results

The multiplicative factors appearing on the right side of eq.(42) all contribute to reduce the polarization that is measurable experimentally. In the COMPASS case, the mean target polarization is about 50% and the dilution factor is ~ 0.45. The $D(y)$ depends on the lepton scattering kinematics; the mean value of y in the event sample used in this analysis is $< y > \simeq 0.48$, giving a mean depolarization factor of $< D_{NN}(y) > \simeq 0.8$. That means that the experimentally measurable polarization is not significantly reduced by the typical COMPASS trigger acceptance.

In addition, eq.(42) is only valid in the case that the Lambda originates from the scattered quark (current fragmentation region). In the real case, the reconstructed Lambda sample contains also a fraction of Lambdas originating from the fragmentation of the target remnants (target fragmentation region). Nevertheless, the small acceptance of the COMPASS spectrometer for events at $x_F < 0$ and $z < 0.2$ naturally suppresses the contamination of Lambdas produced in the target fragmentation.

The number of Lambda decay events available in the sample allowed not only to extract the overall transverse polarization, but also to investigate its dependence over the Bjorken x kinematical variable. The measured P_T as a function of x is shown in Fig.34 for the full data sample and in Fig.35 for the DIS region ($Q^2 > 1 GeV^2/c^2$). The measured values are compatible with zero in all the accessible x range. The data points at $x \sim 0.1$, were the transversity distribution function is expected to be peaked, still have a poor statistical accuracy, therefore no conclusion can be drawn yet on the spin transfer from the target to the final state Lambdas.

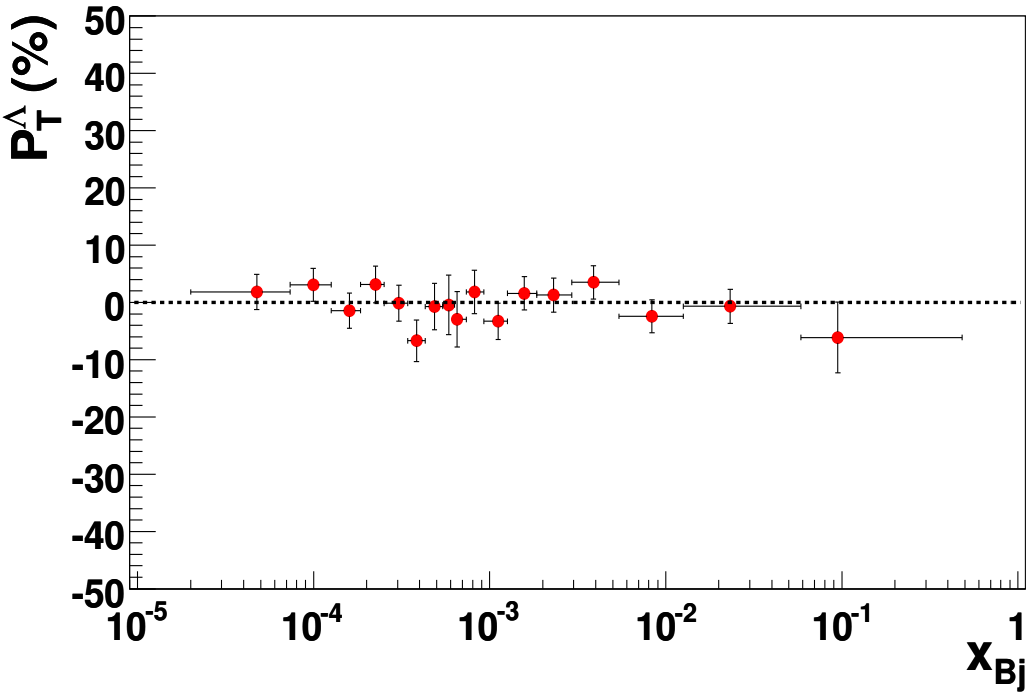

Figure 34: *Measured Λ^0 polarization as a function of x_{Bj}, for all Q^2.*

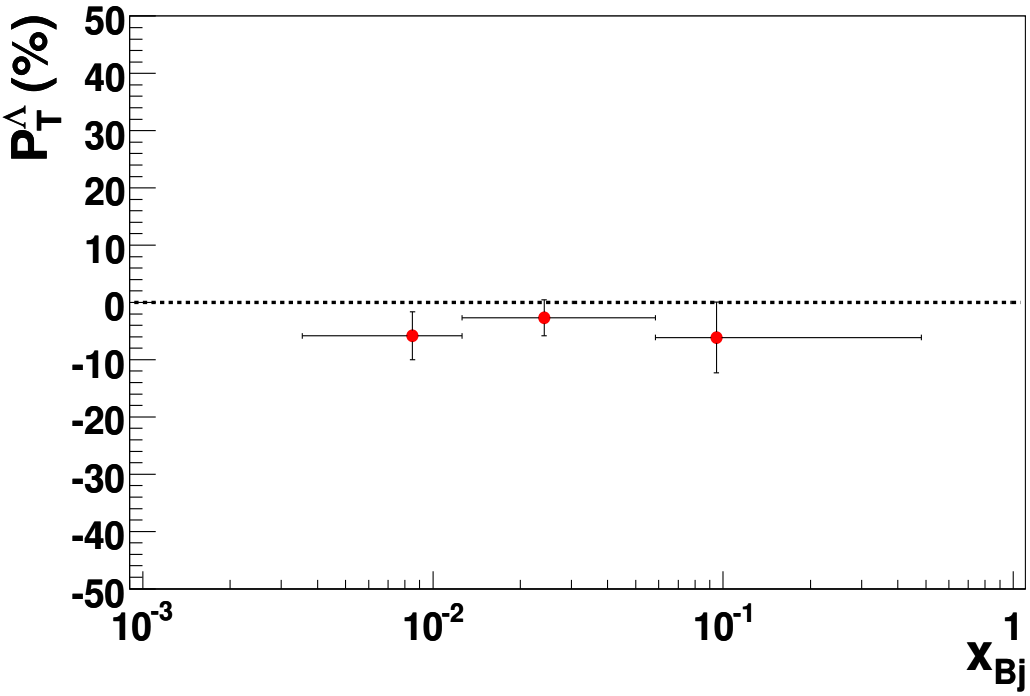

Figure 35: *Measured Λ^0 polarization as a function of x_{Bj}, for $Q^2 > 1GeV^2/c^2$.*

8 The Rich Wall detector

According to the scheme of the complete COMPASS spectrometer set-up described in the COMPASS Experiment Proposal [1] and COMPASS Memorandum of Understanding the full acceptance of RICH 1 detector should have been covered by the large area high resolution tracking detectors. In order to fulfill the complete hadron and muon program with the planned performances, it was proposed to build such a detector called Rich Wall (RW), which would provide important tracking information in the region just behind the RICH 1. The overall responsibility of the RW project was assigned to INFN-Torino group of COMPASS. According to the project [73] the JINR(Dubna) group was in charge for the design and the production of the RW detector(based on Iarocci like Mini Drift Tubes(MDT)) and of its mechanical support structure and convertor plates system. The readout electronics was designed(together with JINR) and produced in Torino.

The motivations to have a tracking detector downstream the RICH 1 can be summarized as following:

- Ameliorate the resolution of Cherenkov ring. The center of the ring is given by reconstructed particle trajectories. One additional space point downstream the RICH 1 with a good resolution $(0.20 - 0.25mm)$ and large lever arm $(4m)$ improves the resolution in spite of multiple scattering due to radiator gas of the RICH 1;

- The registration of muons deflected at large angles, (kinematical region of particular interest for the spin asymmetry measurements in polarized DIS or very large Q^2) will be improved;

- Resolution of D^0 measured by its decaying products (π and K) is also improved thanks again to the large lever arm of this detector;

- To facilitate the tracks matching in different parts of the spectrometer with high intensity beam, either for RICH 1 or for MW1; in particular for RICH 1 where it allows to disentangle the centers of rings belonging to different particles;

- Increase the redundancy and then the efficiency of pattern recognition.

- To better distinguish between charged/neutral particles (eventually γ/e separation). This will be used for better shower reconstruction in the Rich Wall+ECAL1 system

- The presence of the steel/lead convertor in the structure of the RW detector make it working as a preshower for the ECAL1 electromagnetic calorimeter. This as shown in [76] can significantly enhance the calorimeter spatial resolution.

The detector is very useful for the measurement of different kinds of asymmetries that gives us a possibility to extract individual polarized quark and antiquark distribution functions. It can also improve the overall resolution of the first spectrometer.

The requirements to this tracking detector can be formulated as following:

- Very large area of the detector, according to the Proposal [1] $5,27 \times 3,91m^2$, determined by RICH 1 acceptance and results of the Monte Carlo [73];

- Good space resolution ($0.4 - 0.5mm$ *r.m.s.*) per plane or up to $0.25mm$ for the whole system after internal alignment;
- Relatively slim design along the beam axis, in order to fit in the existing setup between RICH 1 and the first electromagnetic calorimeter;
- Maximum possible number of planes to increase the space resolution and to decrease the geometrical inefficiencies;
- Optimize the steel/lead convertor configuration (in aperture) for the best possible electromagnetic shower coordinate measurements.
- Readout compatible with COMPASS-DAQ;
- Fulfill the CERN safety rules and work with non-flammable and fast enough gas mixture;
- Large detector like this one should be based on solid and robust technology, already used in the COMPASS setup (Muon Wall 1).

8.1 Mechanical structure

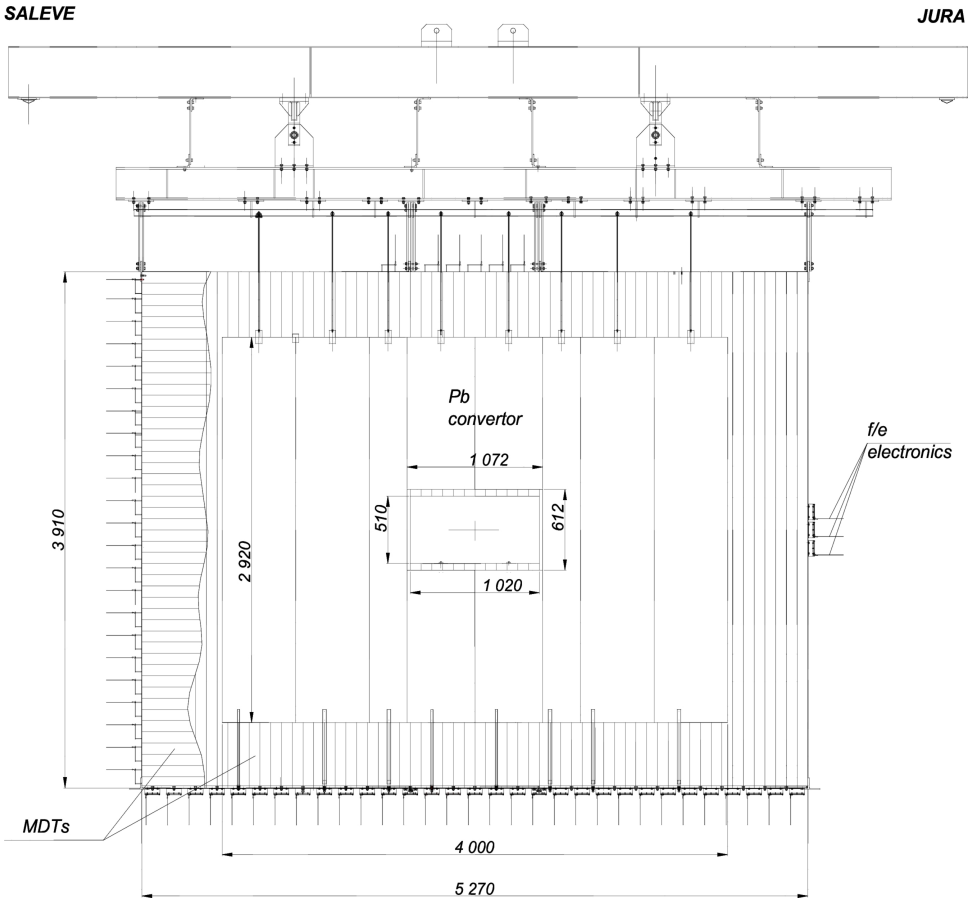

Figure 36: *The front view of the Rich Wall.*

Mechanically the Rich Wall detector is a single big module that has the cross dimensions of $5,27m \times 3,91m$ ($5,14m \times 3.78m$ of active area) with a central hole with the cross dimension of $1.02m \times 0.51m$ see Fig. 36. This big module is made of four sub-modules that have the same cross dimensions. Two of the sub-modules are used for the X coordinate measurement and the other two for the Y coordinate.

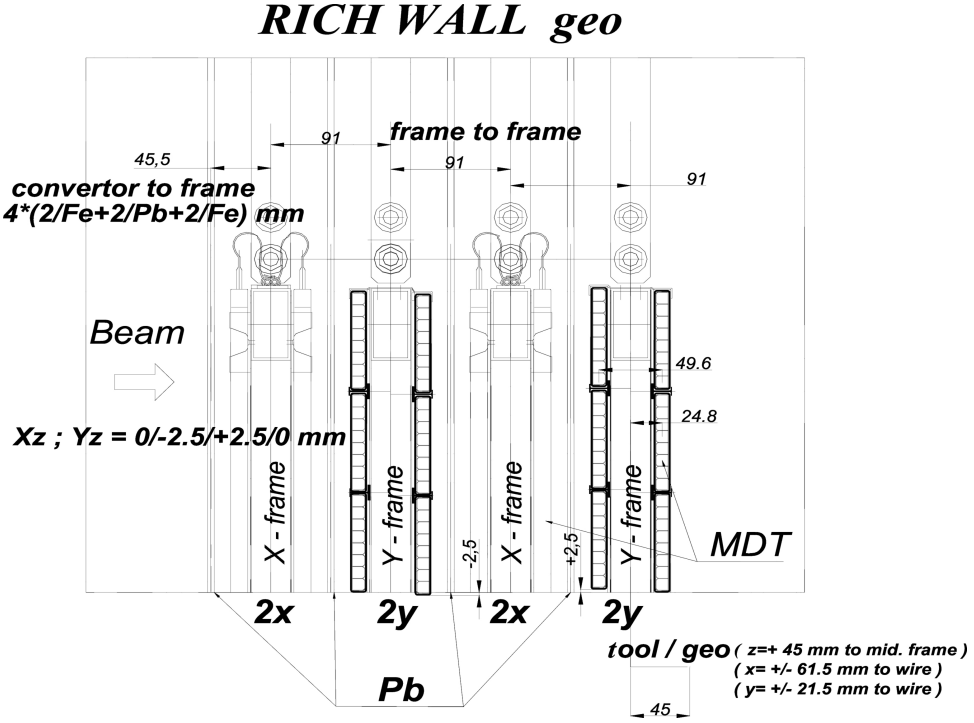

Figure 37: *Structure of the RW module (side view).*

The sub-module in its turn consists of four rigid frames connected together that serves as support for the MDTs that are fixed on both sides of them by means of special brackets, see Fig. 37. Those rigid frames that compose the sub-module are different for the X and for the Y coordinates. To illustrate it one can look at Figs. 38 and 39 where the frontal projection of the X and Y coordinates sub-modules are shown (together with orientation of the MDTs, seen as the strips).

We see that in the X sub-module we have two large pieces of the cross dimensions $2,125m \times 3,91m$ that are situated on both sides of the central hole. The other two pieces with the cross dimensions of $1,02m \times 1,7m$ are positioned on top and under the central hole.

The structure of the Y sub-module is different, see Fig. 39.

We see that here the two big pieces with the cross dimensions $5,27m \times 1,7m$ are positioned horizontally over the cental hole and under it. In their turn the two smaller pieces of the frame with cross dimesions of $2,125m \times 0,51m$ are placed on the both sides of the central hole. In both designs the bigger pices of the structure are used to support the longer MDT tubes and the smaller ones for the support of the short MDT tubes.

After final assembly of all the sub-modules into the RW module we will have the possibility to provide up to 8 points per track in two projections arranged as 2X+2Y+2X+2Y. The module should be hanged up onto a suspension cross bar (see Fig. 36) by two "free

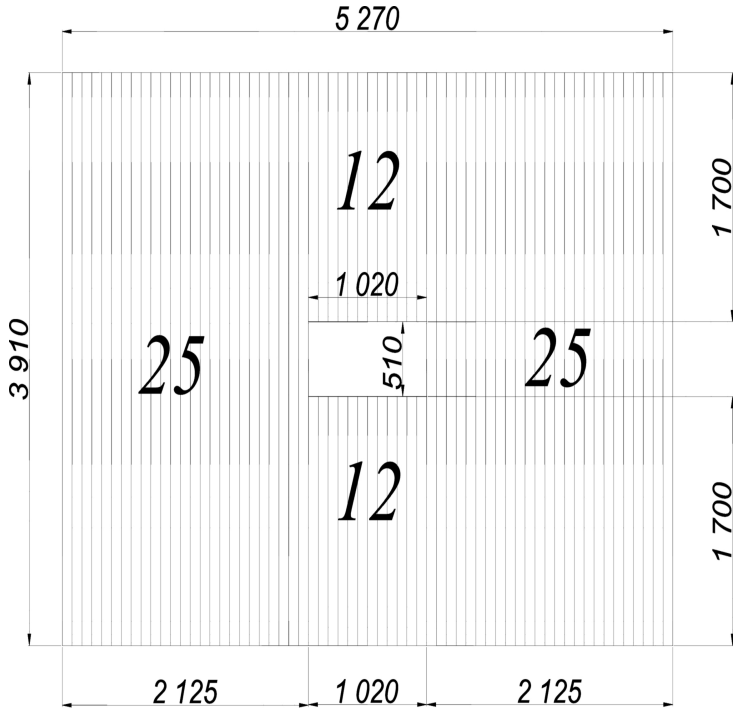

Figure 38: *Frontal view of the X sub-module.*

rotating" joints, which provides minimal stress to assembled module package. This cross bar in turn is positioned at its ends on some structure in a region behind the RICH 1 detector.

Also one needs to mention that the convertor is inserted into the structure of Rich Wall detector as may be seen on Fig. 37 where the 4 layers of the convertor are shown. We see that the first layer is appended before the first sub-module and the three remaining are positioned in between the sub-modules. The cross dimensions of the convertor are shown on the Fig. 36, those dimensions were chosen to cover the whole aperture of the electromagnetic calorimeter (ECAL1) positioned next behind the Rich Wall detector and for which the convertor will serve as a preshower. The design of the convertor is such that in the case of necessity it can be removed as a whole or by parts. This is realized by the the use of special rails on the support bar to which the convertor plates are appended.

8.2 Readout electronics

It consists of two cards: the analog front-end card (AFE) fixed on a detector frame and a digital card (DG). The final view of the cards are shown in the picture taken during the test in the COMPASS Clean Area(Fig.40).

Taking advantage of the RW detector low occupancy (in the outer part), we have developed and use a new front-end module called Hot-Link multiplexer.

The final version of the readout electronics is schematically shown in Fig. 41.

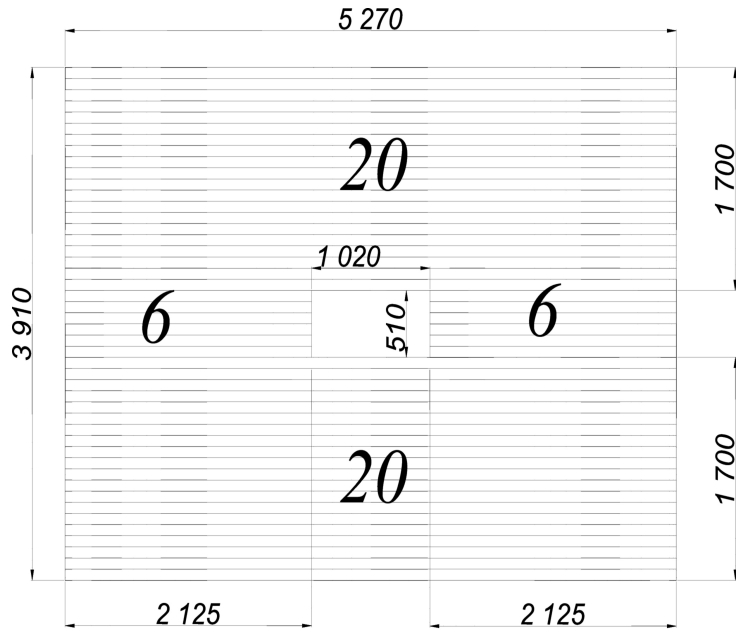

Figure 39: *Frontal view of the Y sub-module.*

8.2.1 Analog and digital readout

The AFE cards are connected to the MDT signal wires by short screened cables. Each AFE houses 16 MAD4 chips, two threshold DAC (Digital to Analog Convertor) chips, the test circuit and power supply filters and voltage regulators. The MAD4 preamplifier/discriminator chip [74] has been developed by the INFN section of Padua for the CMS muon chambers and extensively used for COMPASS MWPC and W4/5 detectors. The stability and performance of this chip has been fully tested during the 2002 COMPASS run. The AFE card is connected to the digital card through a high-speed card edge connector. The connectors bring the LVDS signal of MAD4 and the control signals for the thresholds and the test pulse generator.

The DG card houses 8 F1-TDC [75] chips, the high-speed (40 MHz) Hot-Link chip (40 MB/s input converted to 400 Mb/s output rate) and the initialization circuits. The card is designed to readout 64 TDC channels in parallel.

The F1-TDC is a 8-channel TDC or a 32-channel latch developed in Freiburg for the COMPASS experiment.

8.2.2 Data multiplexing and transfer to the COMPASS DAQ

In order to save money, and to decrease the number of S-links, spill-buffers, and readout PC, taking advantage of the low occupancy of the RW detector, we plan to use a new module called the Hot-Link multiplexer for the final Rich Wall setup. Each Hot-Link multiplexer (HL-MUX) collects and records the data of 8 F1-TDC cards, dispatches the front-end set-up data, and sends the data to the Catch. The module, designed by our group in collaboration with the Munich-TUM group, is based on a single FPGA and will be used also by Silicons and GEM detectors.

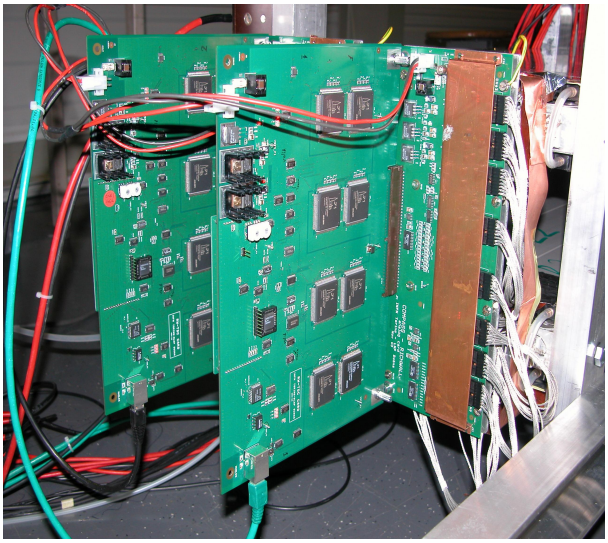

Figure 40: *The final RW readout cards.*

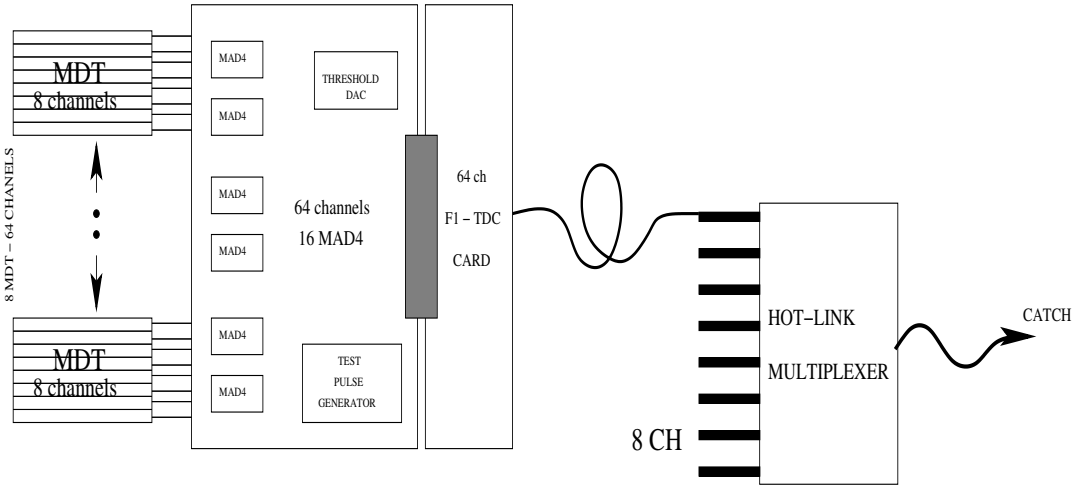

Figure 41: *RW readout electronics scheme.*

9 Tests of the Rich Wall detector prototype

According to the complete set-up of the COMPASS spectrometer described in detail in the COMPASS Proposal [1] and shown in Fig. 42, the full acceptance of RICH 1 detector should be covered by the large area high resolution tracking detector. Such a detector, the so-called Rich Wall, was proposed by the Dubna and Torino groups and approved by the collaboration. As it was then shown by the Monte Carlo standard COMPASS simulation program Comgeant [76] this large area detector, if instrumented with a convertor, can give a substantial improvement in the coordinate resolution for the ECal1 electromagnetic calorimeter of COMPASS (up to an order of magnitude).

According to the contract signed between the INFN-Torino[2] and JINR-Dubna[1], the delivery of the Rich Wall Mini Drift Tubes was scheduled for May 2005, which was too late to have a possibility to test at least a fraction of the detector in real beam conditions, as there was no beam envisaged at CERN during the whole 2005. To be on the safe side and

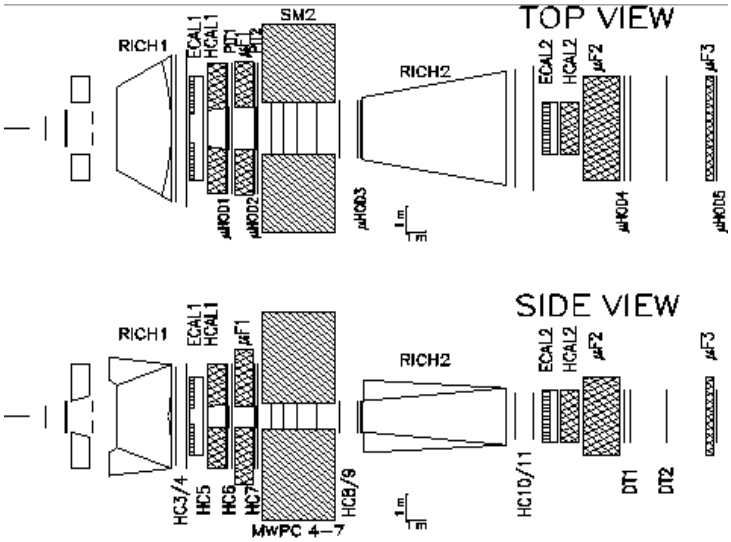

Figure 42: *Layout of the COMPASS apparatus described in the proposal.*

to be well prepared for the year 2006 data taking run, the decision was taken to construct a Rich Wall Full Size Prototype and to test it together with the final electronics during the last 3 weeks of the 2004 data taking period.

The test of major features of the Rich Wall detector can be divided into two separate parts. At the first stage it was necessary to test the system as a whole in the real COMPASS environment, since it was never tested like that before - the final front-end electronics together with the close to final detector configuration and standard COMPASS DAQ system. Such a test could have been carried out only in the 2004 data taking period because this was the only opportunity to work with a real hadron beam before the 2006 running. As a second step the idea was to test the system with two different gas mixtures, Ar/CO_2 (70%/30%) and $Ar/CO_2/CF_4$ (74%/6%/20%). This, due to the time limit, could have been done only in 2005 with cosmic rays.

For those two tests the Rich Wall detector Full Size Prototype(RW FSP) was constructed.

[1]V.M. Abazov, G.D. Alexeev, A.M. Kalinin, Yu.N. Kharzheev, E.V. Komissarov, V.L. Malyshev, A.G. Samartsev, A.A. Shishkin, N.I. Zhuravlev. Reference person G.D. Alexeev alexeev@nusun.jinr.ru

[2]M. Alekseev, A. Amoroso, F. Balestra, R. Bertini, M.P. Bussa, M. Chiosso, M. Colantoni, S. Costa, O. Denisov, A. Ferrero, L. Ferrero, V. Frolov, R. Garfanini, A. Grasso, A. Kotzinian, A. Maggiora, M. Maggiora, D. Panzieri, G. Piragino, S. Sosio. Reference person D.Panzieri panzieri@to.infn.it

9.1 The Rich Wall detector Full Size Prototype

The general structure of the RW FSP is completely determined by the goals of the test listed above. The RW FSP is composed of 8 planes of Mini Drift Tubes (MDT), 4 layers in both projections, 4 tubes per plane (32 channels). The length of the X-plane MDTs is 3 metre, the Y-plane MDTs are shorter - 0.40 metre, which makes RW FSP readily movable and serviced (see Fig.43). The tubes are based on aluminum profile Iarocci [77] like tubes, each tube consists of 8 drift cells. In the center of each cell a 50μm gold plated tungsten anode wire is stretched, each wire is readout individually, see Fig.44.

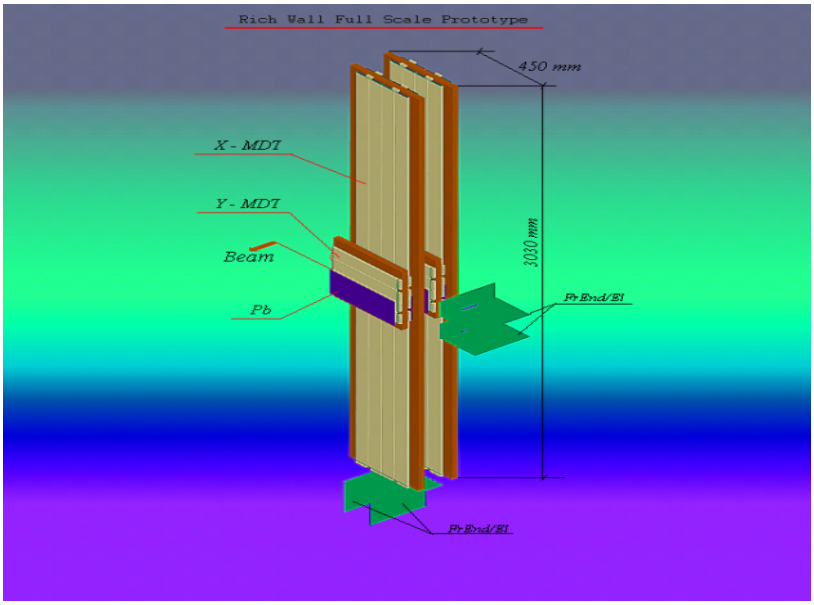

Figure 43: *Layout of the Rich Wall Full Size Prototype.*

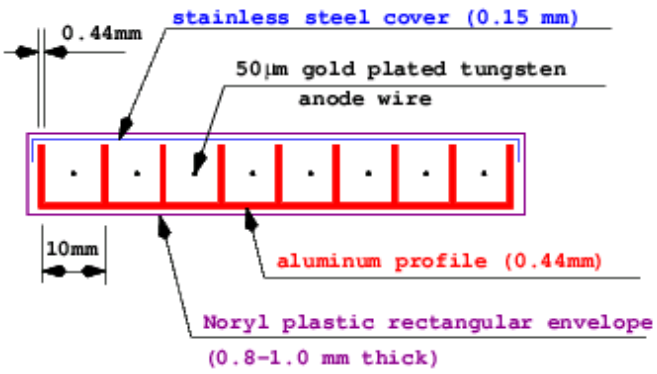

Figure 44: *Schematic view of RW Mini Drift Tube.*

Four layers of the steel/lead convertor are inserted into the RW FSP structure. The convertor covers half of the Y-aperture of the detector ($3X_0$ in total) and is used to

compare the RW FSP features with/without *Pb* at equal conditions. The RW FSP is equipped with a self-supported structure in order to be able to install it vertically on the floor at practically any point of the experimental hall. The upper part was additionally fixed to existing COMPASS structures. The prototype is readout by four sets of FE cards (analog and digital, 64 channels each), so a total of 256 channels are readout via 4 Hot-Link ports.

9.2 Major goals of the 2004 test

In details, the list of tasks can be presented as the following:

- To test the newly produced Mini Drift Tubes delivered from Dubna. This is the first bunch of tubes with the 0.44mm thick aluminum profile;
- To measure the efficiency curves with the different thresholds, time distributions to be studied;
- To test the grounding scheme during the beam test as an essential point for noise reduction and good detector performance. With the RW FSP we plan to learn a lot about the detector and the front-end electronics behavior in the real environment to optimize the grounding and electromagnetic screening scheme;
- Measurements of the occupancy of the RW FSP detector, especially in the preshower operation mode, are also very essential (steel/lead plates inserted in the RW FSP structure). We can also measure the actual accuracy at the maximal rate per tube. The length of the tubes close to the nominal is important parameter for measurement of the occupancy;
- The wire capacity is obviously proportional to the tube length, so only with RW FSP we can perform measurements of the minimal achievable threshold and, then, the spatial accuracy of the detector in the real COMPASS environment.

9.3 Laboratory (COMPASS Clean area) test with cosmic muons

9.3.1 Detector configuration and mechanics

During the test in the COMPASS clean area the whole setup of the RW FSP was mounted horizontally on a special metal frame. The prototype consists of eight MDT layers, four X and four Y, grouped in so-called biplanes. The wire layers in each projection have 5mm staggering for better 'left-right ambiguity' resolution in drift mode. The distance between the centers of two layers of MDTs in a biplane is $54.3mm$. The distance between two biplanes is $182mm$ in one coordinate.

A picture taken during the laboratory (COMPASS Clean Area) test one can see in Fig.45.

The MDT detectors of RW FSP passed through two steps of a test procedure - first, after they were assembled in Dubna and, then when they arrived in CERN. In JINR(Dubna) all assembled MDTs were tested on several stands [78]: for wire tension, for signal homogeneity (X-ray scanning) and for high voltage (training/conditioning with the test gas mixture is performed if necessary). Also, several additional tests were made: for gas tightness as well as for inverse high voltage training/conditioning (when negative HV is connected to a wire) in air; the last test is done, if some wire exhibits a higher noise level, than usual. Typical results of such procedures may be found in ref. [79]. After delivery of the RW FSP detectors to CERN, they passed through restricted set of acceptance tests such as: checks for wire-to-cathode capacitance, a high voltage pretest with the working gas mixture and inverse high voltage training, if needed, to clean-up noisy wires. All MDT's have shown normal behavior and were mounted on the support frames.

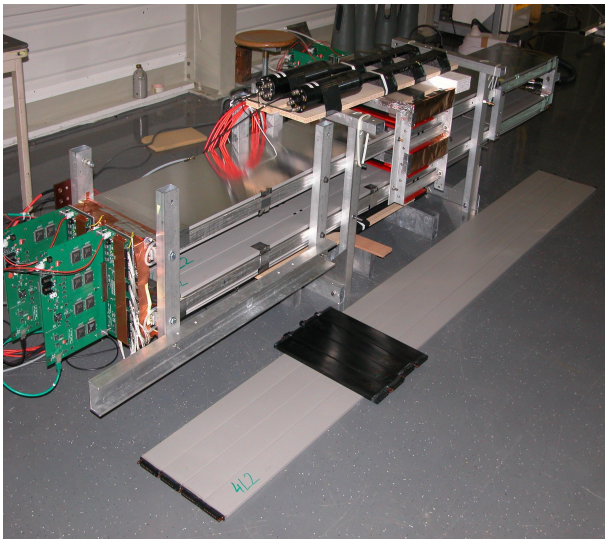

Figure 45: *The RW FSP in the COMPASS Clean Area.*

To produce the trigger on the cosmic muons three scintillation counters were installed: two narrow ones on the upper side of the metal structure supporting the setup, parallel to the longer tubes (X-plane), and a wide one at the bottom. The physical trigger was the coincidence between one of the counters on the top of the RW FSP with the one at the bottom.

To calibrate the electronics (MAD4) in a proper way several problems were resolved.

The analog readout board require a careful calibration of the applied threshold voltages for a proper operation. This is mainly due to the large voltage offset between each channel of the DAC chips used to regulate the threshold, while the MAD4 chips usually exhibit a very good uniformity of the response [74]. The calibration of thresholds has been performed in the following way:

- The same value of the threshold in DAC digits was loaded for all MAD4. Then, with a multimeter directly connected to the FE board, the actual voltage was measured. This was done for different threshold values.

- On the basis of the information collected by the method described above for all channels the relation (digital value/actual value) was calculated (Fig. 46). Knowing that the digital value - to - actual voltage relation is linear, the coefficients A and B were calculated $mV = A * digit + B$. The coefficient A was found to be with high precision the same for all channels.

- Knowing the relation between the voltage in mV, set on the MAD, and the threshold in fC [74], a table of digital values to be set on each different channel for achieving the requested threshold was created.

9.3.2 Organization of the data analysis

Then, a complete test and setup of the readout electronics was performed. The scheme of the readout is shown on the Fig. 47.

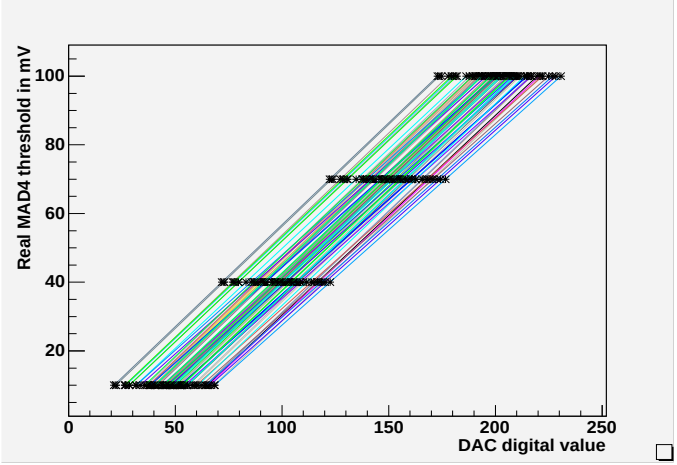

Figure 46: *MAD4 calibration curves.*

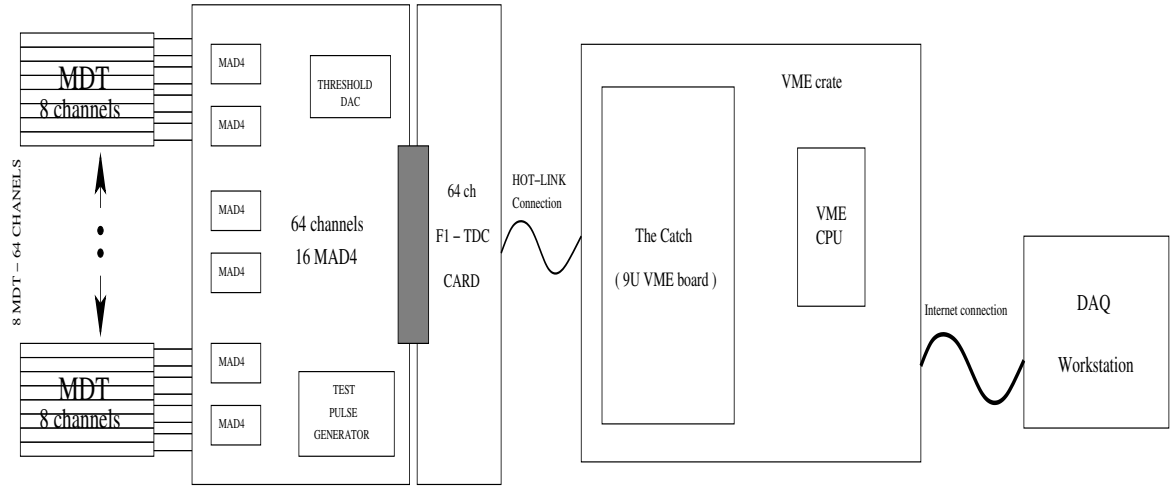

Figure 47: *RW FSP readout organization during the Clean area test.*

The test of the RW FSP in the Clean area was performed in several steps:

The first task accomplished during the test was a check of the screening from the electromagnetic noise. As we have seen, if no additional screening was installed, there were quite a high number of noisy channels. After additional screening and grounding of the readout cables connecting the MDT's outputs and the AFE input connectors were mounted the number of noisy channels was reduced to a negligible level. Having resolved the noise issue it became possible to obtain the hit profiles and drift time spectra from all the planes Fig.48.

From that figure we can clearly see the position of the trigger counters over the upper biplane. After that, a large amount of data for determination of the working parameters (thresholds and high voltages) were taken. From that data the efficiency curves were calculated. The efficiency plateau is limited from the higher voltage side by the sharp increase of both, dark currents through MDTs and noise level. As one can see from Fig.49, the appropriate values for the voltage and threshold are $2050V$ and $15mV$(approx. $4fC$),

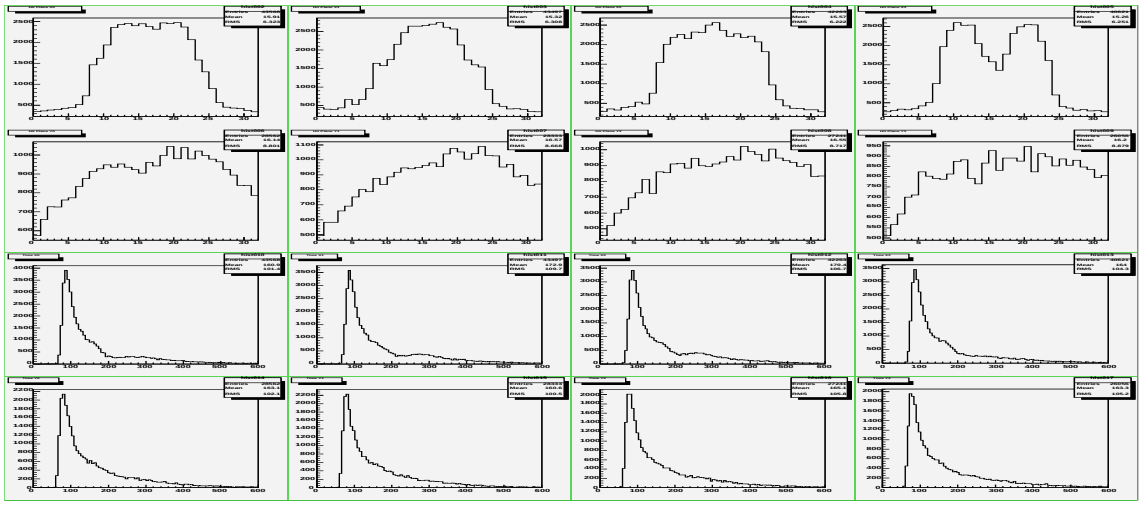

Figure 48: *RW FSP cosmic muon profiles and drift time distributions. The upper row shows the four X planes(from the lower to the upper one), the second one shows the four Y planes and the lower two show the drift time distributions with respect to the planes. Measure with Ar/CO_2 (70%/30%) gas mixture.*

respectively. Fig.50 gives a typical hit sample for the cosmic track event.

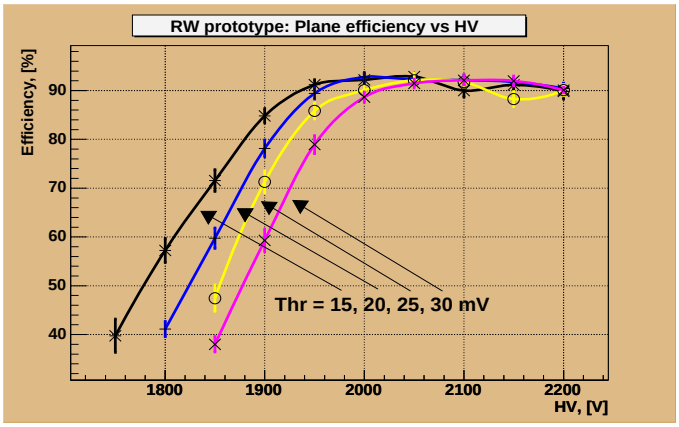

Figure 49: *RW FSP efficiency curves.*

When the working point was determined, the measurement of the real spatial accuracy of the detector was performed. The procedure consisted of the following steps:

- From the drift time spectra, the $R(t)$ distribution was extracted. Having no precise trackers surrounding the FSP, the $R(t)$ relation was simply derived from the integral of the time jitter distribution, properly normalized to the MDT cell size.
- First, a cut on the hit multiplicities was applied: events having only four hits (one in each layer) in the X or Y projection were selected.
- Second, a cut was imposed on the orthogonality of tracks to the plane of the detector. Only small-angle tracks were analyzed.
- Then, from all four fired wires and from the time information from the $R(t)$ relation the possible coordinates (two, one on each side of the wire) of the track in each tube were calculated.
- Having four tubes involved, there were 16 possible track combinations, which were examined.
- From 16 possible combinations, the one with the best χ^2 value was selected (by linear fit).
- The space accuracy was calculated as r.m.s. of residuals distribution - the difference $(R - r)$ where R is the estimated distance from wire of the track (found from the $R(t)$ relation on the basis of the difference in the time between the trigger and the hit) and r is the distance that entered in to the fit procedure.

This test shows that the expected spatial accuracy of about $0.5mm$ is confirmed for both planes. The last step in the analysis concerned an estimate of the drift velocity. From the cell size of the MDT and the position of the visible bump to the right of the peak in the time distribution, which we assume is due to the photoelectric effect of the photons, escaping from the avalanches created by electrons around the wire, and knocking out electrons from the aluminum cathode of the tube, that in turn drift and produce a signal (the so-called "afterpulse", Fig.48), an average value of 20 $nsec/mm$ was obtained for the inverse drift velocity. This is in good agreement with the properties of the used gas: $Ar(70\%) + CO_2(30\%)$.

9.3.3 Major results of the test

The major results of the test are the following:

- A very low threshold value was achieved, while the system operates in a stable way ($\sim 15mV$ roughly corresponding to 4 fC).
- The profiles induced by the cosmic muons are seen very clearly without noisy channels, and, also, the time spectra look like it was expected.
- The efficiency curves for different high voltages and thresholds were measured (see Fig.49), the plateau width was found to be rather large - not less than 200 Volt.

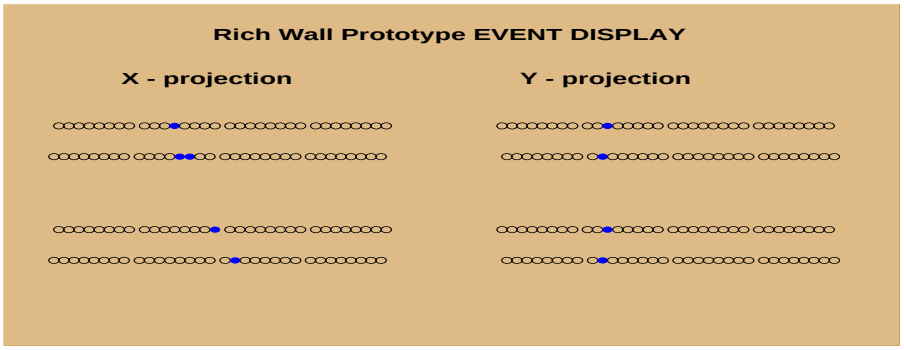

Figure 50: *RW FSP event display.*

- The coordinate accuracy per plane was found to be good enough, about $0.5mm$ r.m.s.

9.4 Hadron beam test

During the 2004 pilot hadron run a beam of 190 GeV/c negatively charged hadrons has been used. The beam was mainly composed of π^-, K^- and $\overline{p}$ in the proportion 0.950 / 0.045 / 0.005. The additional small contaminations of μ^- from the π^- decay and of e^- have not been estimated yet.

The beam has typically a cross section with the r.m.s. of $3 \times 4mm^2$ at the COMPASS target, a typical divergence of 60 μrad in the bending plane and a momentum spread of 0.7%. The beam intensity was $5 \cdot 10^6 hadrons/spill$ and was determined by the maximum radiation dose tolerable for the ECAL2 calorimeter.

9.4.1 RW FSP integration into the COMPASS spectrometer

The RW FSP was installed in the COMPASS experimental hall close to the Rich Wall nominal position right behind the RICH 1 detector. During the first part of the test with a normal intensity beam the RW FSP was mounted at the distance of 9645 mm downstream the target and the distance between the beam and the X-wire closest to it was 1553 mm. Then, for the test with higher intensity beam the prototype was moved closer to the beam axis to the position 9675 mm downstream the target and 1003 mm outside the beam.

In Fig.51 one can see a picture of the RW FSP installed in the experimental hall right behind the RICH 1 detector.

9.4.2 RW FSP integration in the COMPASS Data Acquisition

The scheme of the readout is shown in Fig.52.

During the test of the RW FSP in the COMPASS setup the readout of the digital cards was done through a direct connection to the catch. It was possible due to the small number of channels read (256 channels), which allowed to avoid the usage of the multiplexer

Figure 51: *The RW FSP in the COMPASS set-up.*

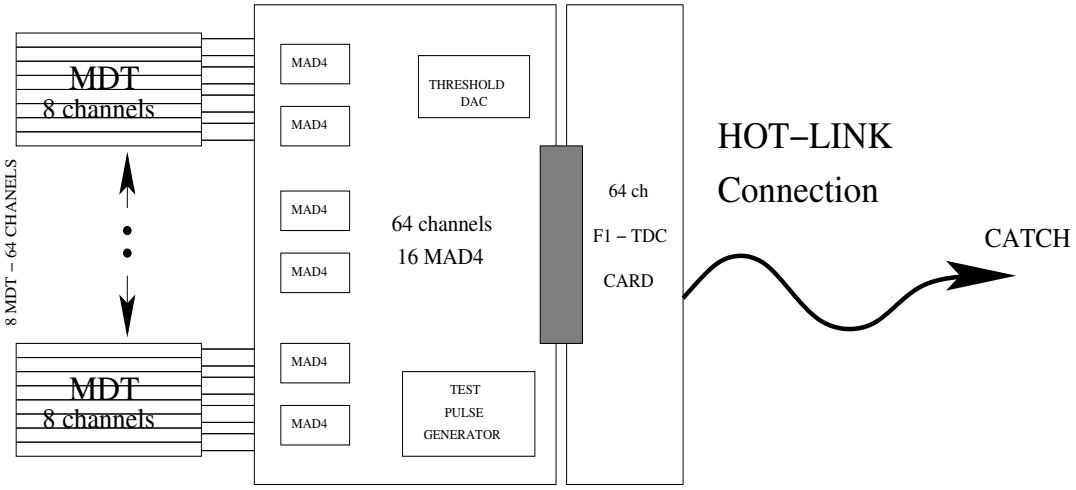

Figure 52: *RW FSP readout organization during the test in the beam.*

envisaged for the Rich Wall detector. To be able to work with the data from RW FSP inserted in the data stream of the COMPASS experiment some change of the monitoring software was needed. First the COOOL (COMPASS Object Oriented Online) program was modified to display correctly the relevant monitoring data. Then, the mapping file was created and, then, added to the official COMPASS software. This mapping file enables the COOOL and CORAL (COMPASS Reconstruction and AnaLysis) programs to understand correctly the RW FSP data in the data stream/file. After that, all threshold values were written in the standard COMPASS database. That was required for the correct (synchronous) initialization and operation of the RW FSP in the normal data taking regime of the COMPASS experiment.

9.4.3 Major results of the test

A successful software and hardware implementation of the RW FSP in the COMPASS experimental environment was performed. The RW FSP demonstrated very stable operation in the real COMPASS environment with the nominal working parameters (thresholds and HV).

9.4.4 RW FSP operation as a preshower

As it was mentioned earlier, the operation of the Rich Wall as a preshower for the $ECAL1$ will be very important. This will significantly improve the spatial resolution of $ECAL1$. The test of this preshower mode of operation was performed by the half Y-aperture of the RW FSP covered with a steel/lead convertor. The hit profiles (Fig.53) clearly exhibits the strong effect of the convertor manifested as a multiplicity increase by a factor of two in the region covered by the convertor. The upper and the lower rows in the hit profiles show the four X planes and the four Y planes, respectively. We can clearly see the convertor position by the rise in the hit profiles on the Y planes. The slope in the hit profiles on the X planes is due to the fact that the beam position is on the right corresponding to those images and we see the decreasing halo.

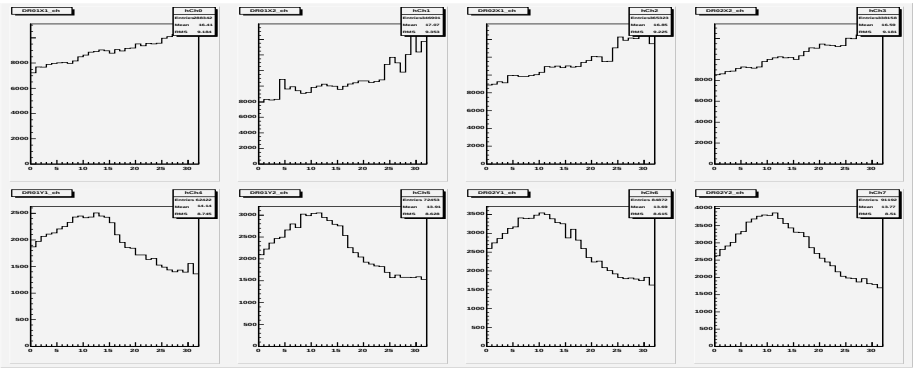

Figure 53: *The RW FSP hit profiles during the hadron beam exposition.*

The double hit resolution (Fig.54), being a very important parameter for correct evaluation of the number of charged particles in the Rich Wall detector volume, that, in turn, gives the possibility for better evaluation of the energy lost by the electromagnetic shower there in [76], was also measured. It was done by selecting the events, when two hits were registered on one or more wire, and by computing the time difference between them (the time of the second hit minus the time of the first hit).

The plot in (Fig.54) shows the time difference between two hits occurring in the same drift cell during the same event summed up over one MDT tube (8 wires) of the Y-plane. The minimal value was found to be around $50ns$. It results from contribution of two sources - the MDT detector pulse shape and the MAD4 clipping time (40 ns). The measured value of the best achievable double hit resolution in Rich Wall system is 50 ns.

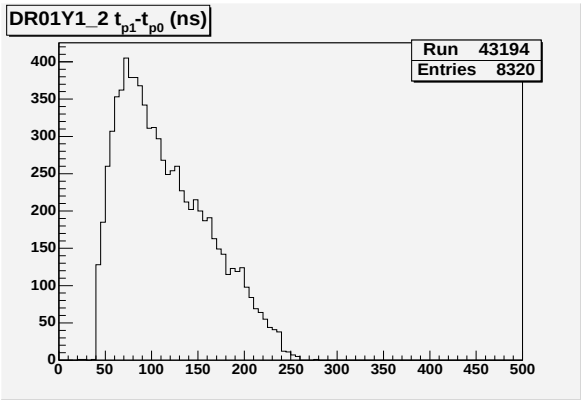

Figure 54: *The RW FSP double hit resolution (in ns).*

9.4.5 RW FSP single plane spatial accuracy

The data obtained with the RW FSP provided the possibility to check once more the coordinate accuracy of the detector in the real experimental conditions. This time, the procedure was practically the same with only one additional approximation that the $R(t)$ relation was constant and equal to $5.17mm/110ns = 0.047mm/ns$ for the whole volume of each single MDT cell. This approximation was introduced for simplicity and due to the fact that even with such rough approach we get results in the required interval. Further, when the information from trackers will be analyzed a more correct method will be used for $R(t)$ calculation. The value 5.17 mm comes from MC simulation. It was demonstrated that in our experimental conditions with a particle flux practically perpendicular to the detector plane at distances larger than 5.17 mm there occur only approximately 3 ionization pairs (in $Ar(70\%)CO_2(30\%)$ we have $\sim$ 30 pairs/cm). Moreover, the RW FSP is not sensitive to events in which less than 3 ion pairs were created. The resulting residuals distributions are shown in Fig.55.

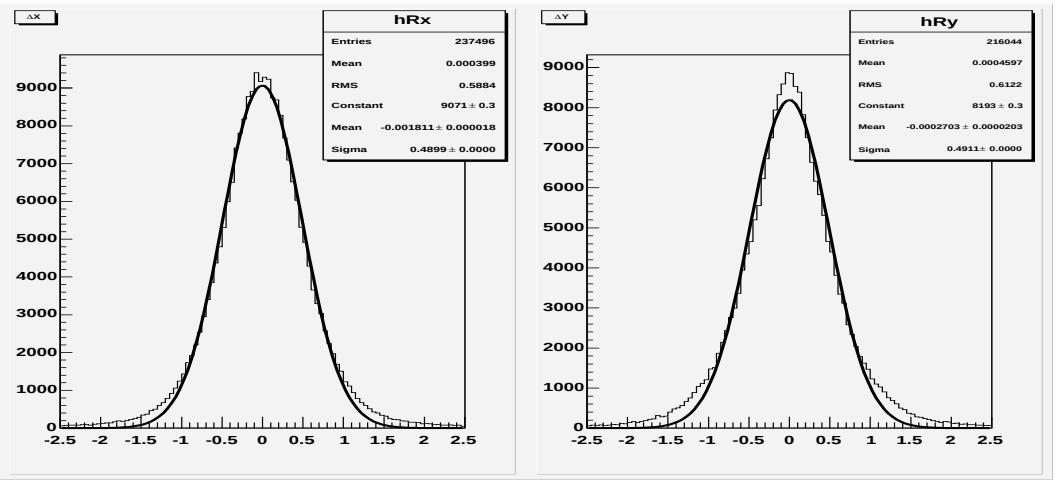

Figure 55: *Spatial accuracy with normal beam intensity.*

The left plot in Fig.55 corresponds to the cumulative spatial accuracy for the X plane(with a sigma of $\sim 0.49mm$) and the right one to the Y plane(with a sigma of $\sim 0.49mm$).

9.4.6 High intensity test results

During the last night of the hadron beam running period, two high-intensity (10^8 hadrons/spill) runs were taken. A very important result of the test concerned the spatial accuracy with the high-intensity hadron beam. One can see (Fig.56) that during the high-intensity beam run we practically had the same value.

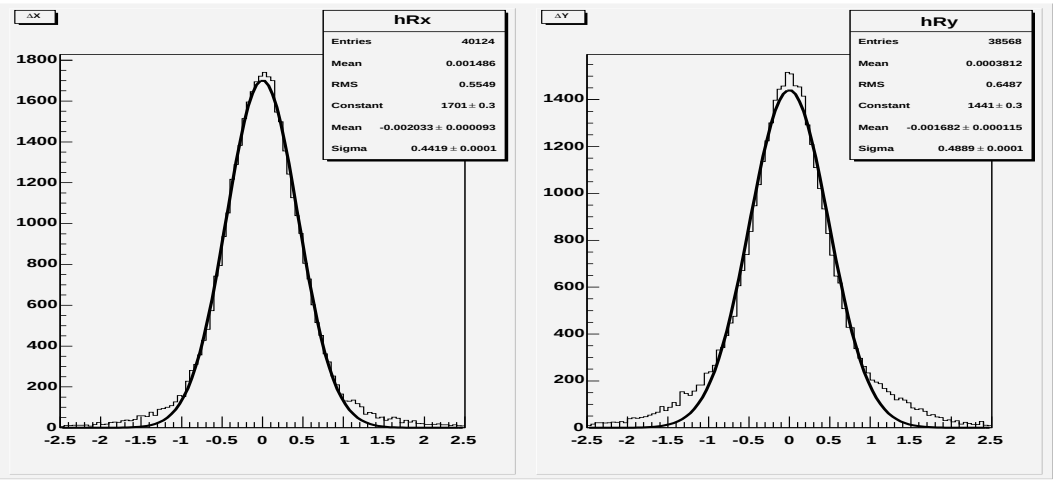

Figure 56: *Spatial accuracy with the high-intensity beam.*

The left plot of the Fig.56 corresponds to the cumulative spatial accuracy for the X plane(with a sigma of $\sim 0.44mm$) and the right one to the Y plane(with a sigma of $\sim 0.49mm$). So, no space charge problems connected to the high beam intensity were observed. It is extremely important that we are able to work stably at very high rates. It is also important that the estimated value of the occupancy is acceptable (not more than few percent).

Single plane rates measured during the hadron beam exposition are presented in Fig.57.

The upper row of the Fig.57 shows the four X planes and the lower one the four Y planes. The units of the *y-axis* are kHz. The dashed line corresponds to normal intensity rates and the solid one to the high intensity situation. We can clearly see the increase in the hit rates.

Another important practical aspect of Rich Wall performance, especially as preshower when particles multiplication processes take place, concerns the ageing effects. The observed high voltage currents through MDTs during high intensity hadron run do not impose such a limitation, fortunately. This conclusion is made using the results of ageing effects measurements made for MW1 system (Ar/CO_2 gas mixture and ABS plastic envelope) and for RW MDTs (Noryl plastic and Ar/CO_2). For both the ageing effects were not observed up to 1 C/cm of accumulated charge on a wire.

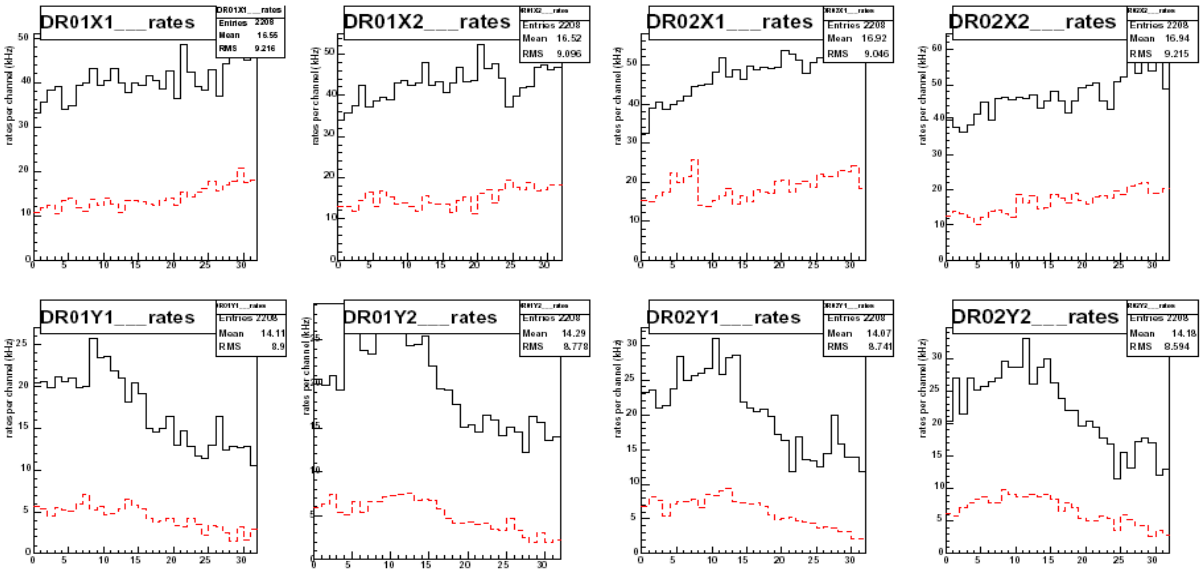

Figure 57: *The RW FSP rates measured during hadron beam exposition.*

9.5 Conclusions of the 2004 test

During the test of the RW FSP in both the Clean Area and the experimental hall all the goals of the test were successfully achieved. One can see that all the MDTs with the $0.44mm$ thick aluminum profile performed exceptionally well. All the electronics worked without problems, even without additional screening apart from the screening of the signal cables. The RW FSP was completely integrated into the COMPASS setup like any other detector. It behaved in a very stable way in the real COMPASS environment. All basic parameters of the RW FSP were measured, and the results were very close to our expectations. Working with those parameters in the COMPASS setup the RW FSP showed excellent results also in the high-intensity beam conditions, even in the preshower mode with a low threshold (of $4fC$) without any degradation of the spatial accuracy.

9.6 Goals of the 2005 test

In particular we were interested in the following tasks:

- To improve the shielding in order to reduce the noise rate, which is necessary for good detector performance;
- To compare results with Ar/CO_2, obtained in 2005 with results from the FSP tests in 2004. This means that the muon hit profiles, drift time distributions and efficiency curves should be measured for various high voltages and thresholds. At the working point the spatial accuracy was measured;
- To study the behavior of the detector with the gas mixture $Ar/CO_2/CF_4$ by measuring hit profiles, drift time distributions, efficiency and spatial accuracy. The hit rates are expected to be higher in preshower mode operation of RW. This gas is attractive because of its cleaning up features and higher drift velocity with respect to Ar/CO_2, which might be important in conditions of rather high particle rates.

In 2004 the RW FSP was successfully tested both with cosmics in the Clean Area and in the COMPASS set–up with a hadron beam. The only used gas mixture was Ar/CO_2.

9.7 Laboratory/COMPASS Clean area test with cosmics

9.7.1 Set–up for the RW FSP test

9.7.2 Description of the measurements with two gas mixtures

During 2005 the set–up was the same as used in the test in 2004. Only the thresholds were checked again with a voltmeter on the F.E. boards.

There were several measurements to be completed during the 2005 test:

- Noise rate with random trigger;
- Muon hit profiles and drift time distributions with cosmic trigger for two different gas mixtures (Ar/CO_2 and $Ar/CO_2/CF_4$);
- Efficiency measurements for different thresholds and various high voltages for two different gas mixtures;
- Calculation of R(t) and measurement of spatial accuracy at the working point for two different gas mixtures.

9.7.3 Noise rate

Before starting to operate the FSP with cosmics the noise rate was reduced. The random trigger was used to do this. The shielding was already improved during the test in 2004, but there were still some noisy channels. The first improvement was achieved by putting copper foil around the signal wires of all planes. The noise rate was reduced by a factor of 3–5. It was seen in the 2004 FSP test that outer planes behave differently from inner

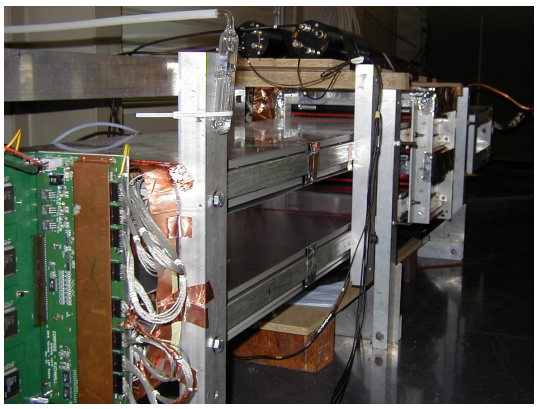

Figure 58: *RW FSP with extra aluminum plates between biplanes.*

ones. So we mounted extra aluminum plates on the inner planes of the X–direction, as it was done for the external ones. The FSP with two extra aluminum plates can be seen in Fig.58. These plates reduced the noise rate significantly. Then we fixed the plates with copper tape. This reduced the noise rate again. Finally a noise rate less then 3kHz

was achieved in all planes with the very low threshold of 10mV (≈ 3fC). The minimal threshold in 2004 was 15mV (≈ 4fC).

9.7.4 Measurements with Ar/CO_2 (70%/30%)

First, the hit profiles and drift time spectra were measured (see Fig.59 and Fig.60) to check the reproducibility of results of the previous year 2004.

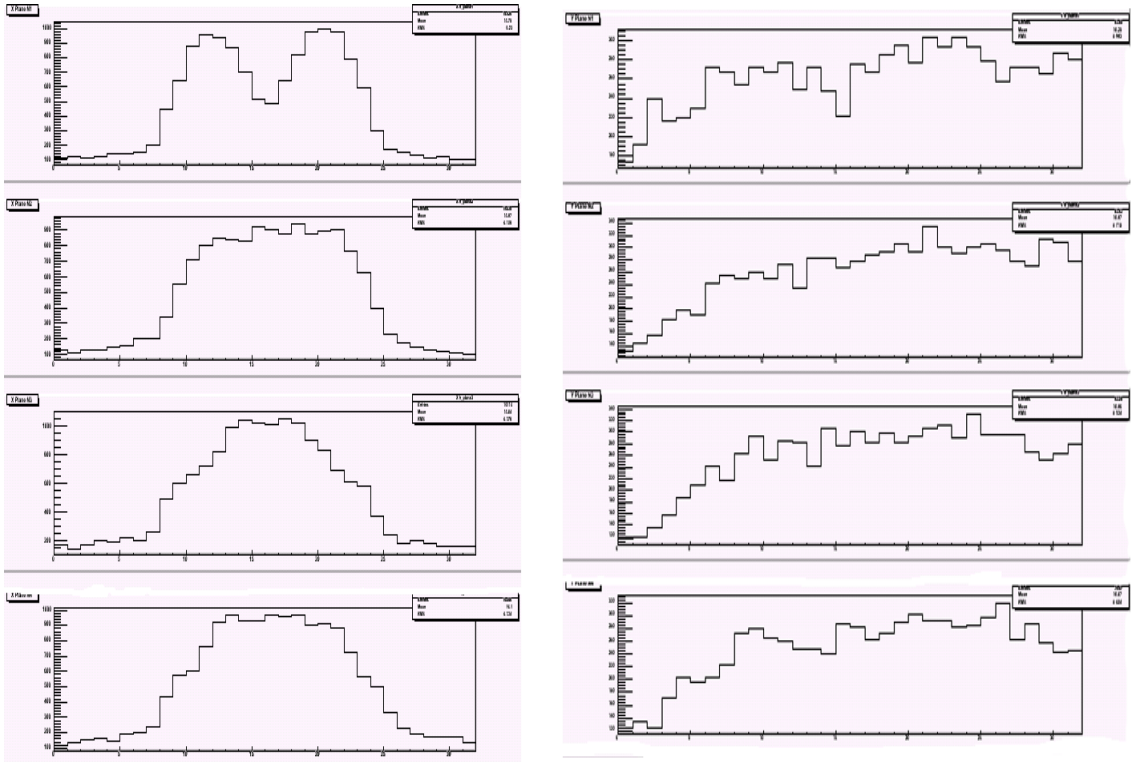

Figure 59: *RW FSP cosmic muon hit profiles of X–planes (left) and Y–planes (right) (from upper to lower planes, x–axis: wires, y–axis: number of hits).*

The position of the trigger counters on the top of the prototype can be clearly seen in the muon hit profiles of the X–planes (Fig.59). The drift time distributions (Fig.60) show that all planes behave equally. The width of the spectra is about 150 ns. It is interesting to mention that some MDTs exhibit "afterpulsing" effect which is especially pronounced at high rates (see see Fig.61, where the drift time spectra taken during the high intensity hadronic run in 2004 are shown). We could associate it with the features of particular MDT's aluminum cathode - its quality as a photocathode may in principle vary from one tube to another. This effect being not dangerous for the RW application requires additional study.

For measuring the efficiency curves large amount of data for various thresholds was taken. The efficiency was calculated using 3 and 4 hit events. A 4 hit event is an event with a hit in all 4 layers in X–planes or Y–planes. Then a cut on the orthogonality of tracks to the detectors plane was imposed. Only small angle tracks were accepted.

The event display of a typical 4 hit event from a cosmic muon traversing the detec-

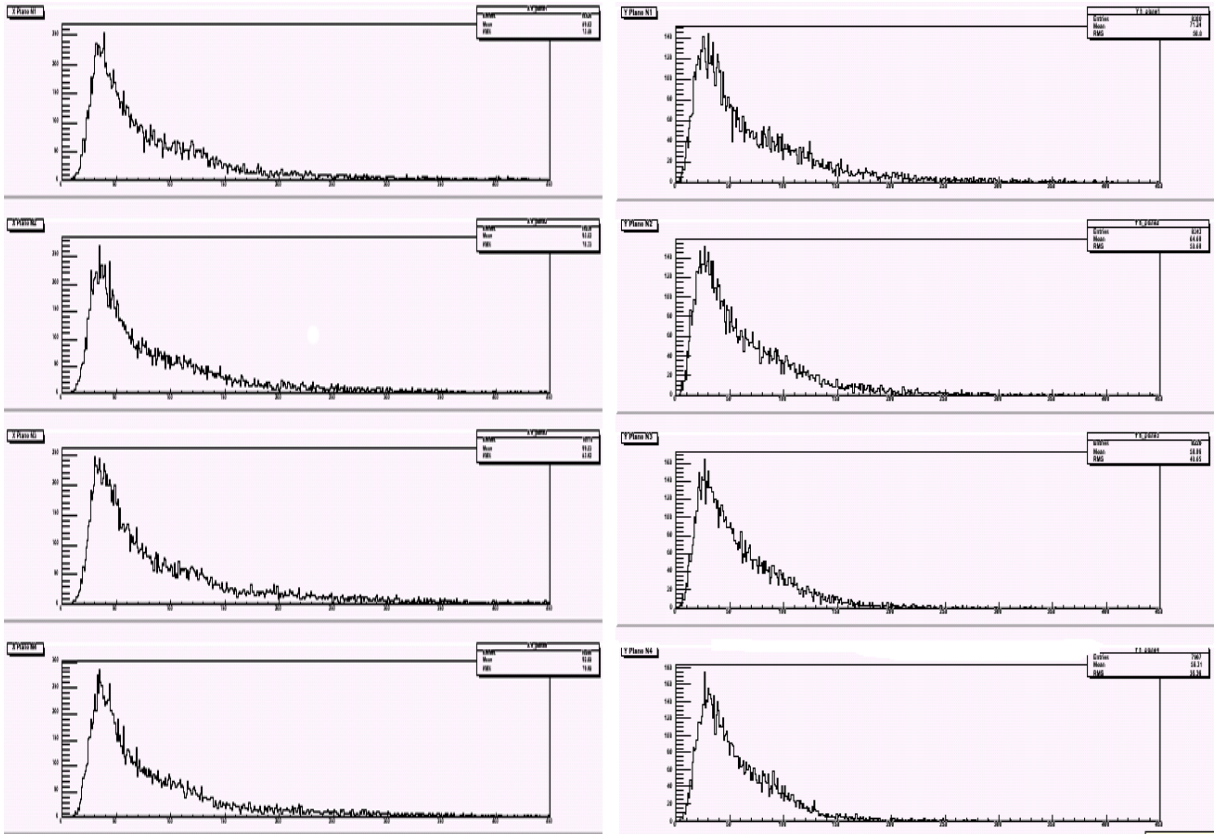

Figure 60: *RW FSP drift time distributions of X–planes (left) and Y–planes (right) from test in 2005 (from upper to lower planes, x–axis: time in nsec, y–axis: number of hits).*

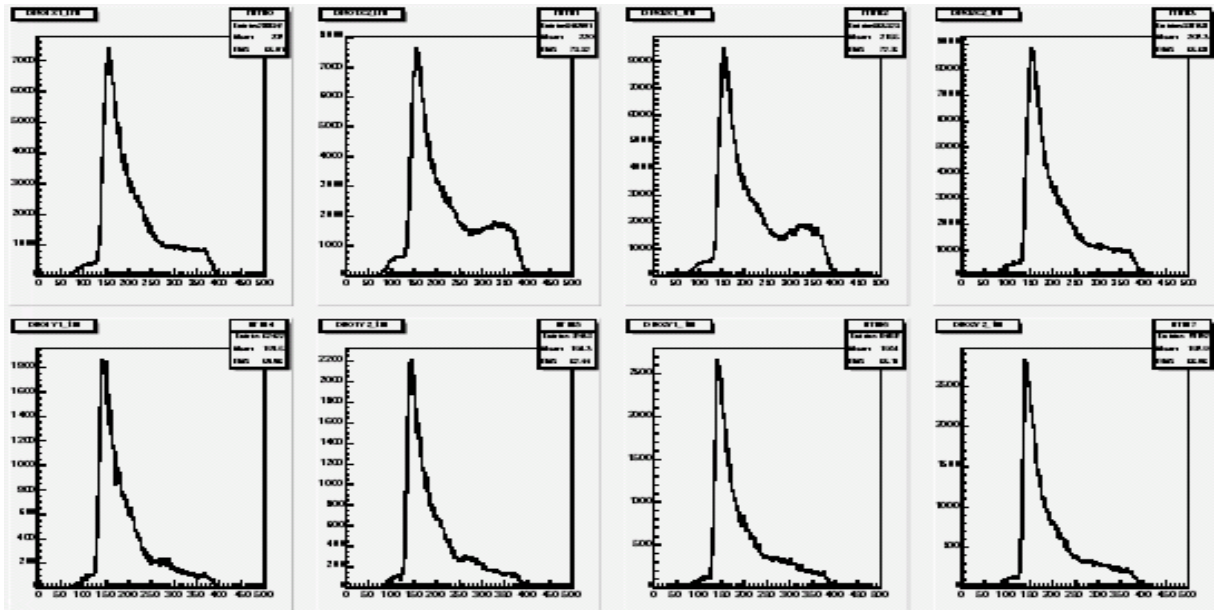

Figure 61: *Drift time distributions from test in 2004 (first row: X–direction, second row: Y–direction, x–axis: time in nsec, y–axis: number of hits).*

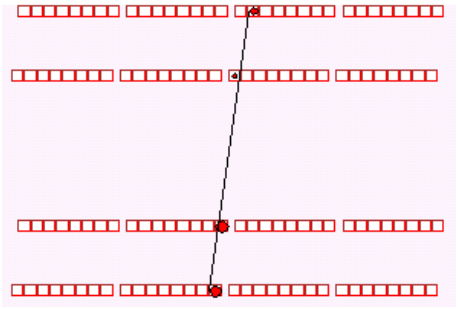

Figure 62: *RW FSP event display, 4 hit event.*

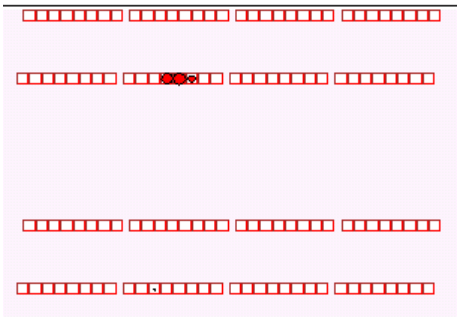

Figure 63: *RW FSP event display, noise.*

tor is shown in Fig. 62. In Fig. 63 one can see a noise event.

The calculated efficiency curves are shown in Fig.64. With the efficiency curves the

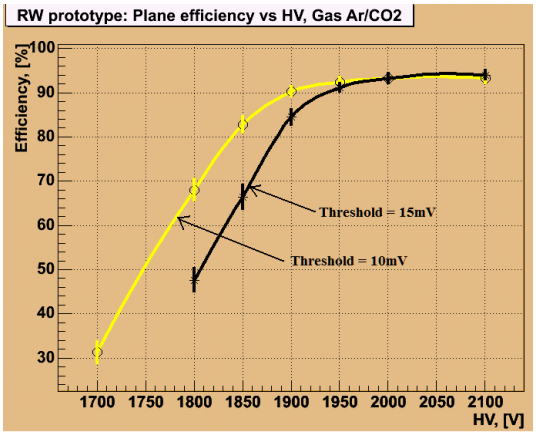

Figure 64: *RW FSP efficiency curves with gas* Ar/CO_2

working point was set to threshold 15mV $\approx 4fC$ and high voltage 2000V. The high voltage value was chosen at the beginning of the plateau in order to work with as low as possible collected charge, that helps to minimize ageing.

Then a large amount of data was taken in order to calculate the spatial accuracy. The spatial accuracy was obtained in the following way:

- The R(t) distribution was calculated from the drift time distribution. The drift spectrum was integrated and then fitted in the range from the wire position (0mm) to the maximum distance in the corners of MDTs (6.7mm). The electric field in the corners of the tubes differs from the electric field in the middle of the tubes. This causes a different drift velocity for electrons, and leads to a kink in the R(t) relation, see Fig.65.

- 4 hit events were selected, which have only small angle tracks.

- Two possible coordinates for each plane (two, one on each side of the wire) were calculated. For this purpose the time information of the R(t) relation and the coordinate of the fired wire were used.

- Thus one got 16 possible hit combinations for a muon track passing through four tubes.

- Then the combination out of 16 with the best χ^2 value was selected (by a linear fit).

- Finally the spatial accuracy was calculated as r.m.s. of residuals distribution, which is the difference (R – r) where R is the calculated coordinate, obtained from the R(t) relation on the basis of the time difference between trigger and hit, and r is the coordinate obtained from the fit procedure.

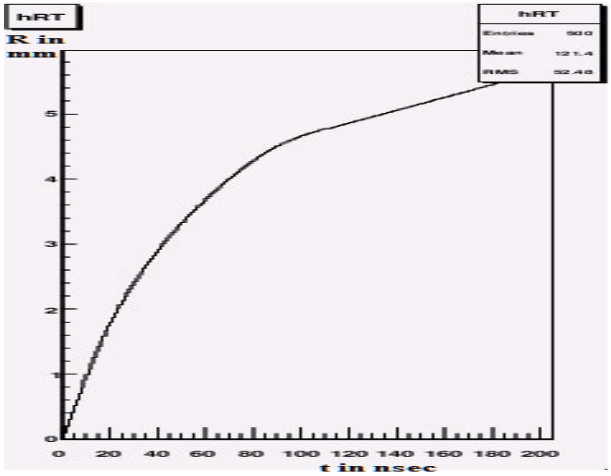

Figure 65: *R(t) relation.*

The achieved spatial accuracy for the X1 plane can be seen in Fig.66. The distribution was fitted with a Gaussian. All other X and Y–planes have similar values around 0.4 mm. The calculated inverse drift velocity is $\approx$ 20ns/mm. This is in good agreement with the properties of the used gas mixture and the results of the 2004 FSP test.

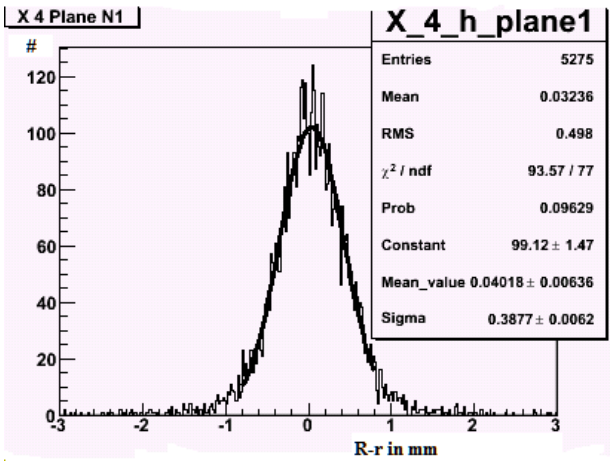

Figure 66: *Spatial accuracy of plane X1, uppermost plane in X-direction.*

9.7.5 Measurements with $Ar/CO_2/CF_4$ (74%/6%/20%)

The same measurements as with Ar/CO_2 gas mixture were also done with $Ar/CO_2/CF_4$. First, the noise rate was checked and it was again very low. Then the hit profiles and drift time spectra were measured, see Fig.67 and Fig.68. The scintillation counters on

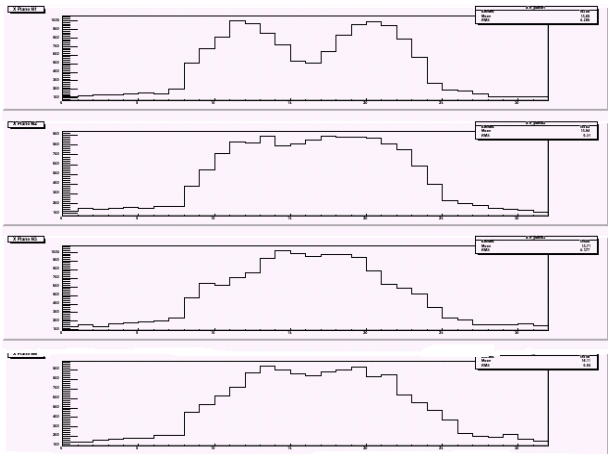

Figure 67: *RW FSP cosmic muon hit profiles of X-planes (from upper to lower planes, x–axis wires, y–axis number of hits).*

the top of the FSP can be seen again in the first muon hit profile (Fig.67). All profiles look as expected.

The drift time distributions (Fig.68) are narrower than with Ar/CO_2 (see 9.7.4). The width of the drift time distributions is $\approx$ 100ns. As one can observe all planes behave equally.
Then data to calculate the efficiency curves were taken, see Fig.69. The plateau width is larger than 150V. It was even possible to stably run the FSP with a maximum high voltage of 2375V.
At the end of the test, data at the working point (threshold 15mV $\approx 4fC$ and high

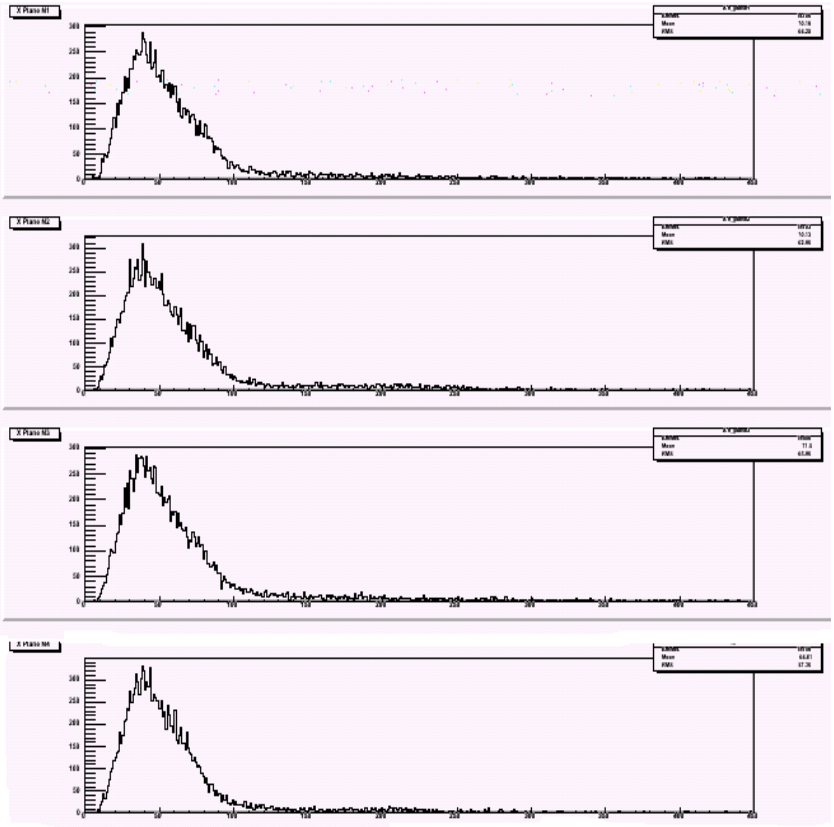

Figure 68: *RW FSP drift time distributions of X-planes (from upper to lower planes, x–axis time in nsec, y–axis number of hits).*

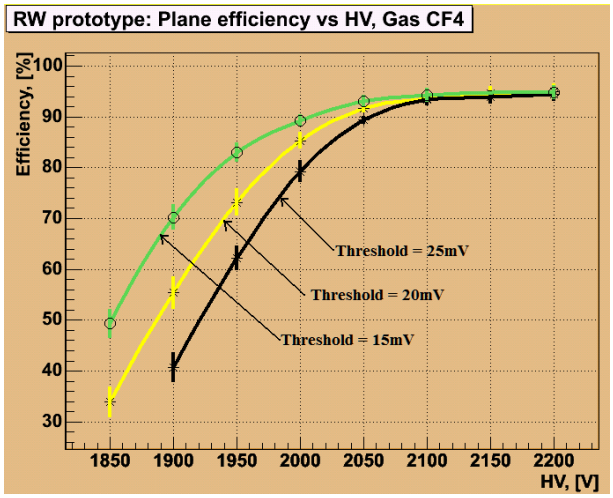

Figure 69: *RW FSP efficiency curves with gas* $Ar/CO_2/CF_4$.

voltage 2100V) to calculate the spatial accuracy were taken. The calculated R(t) relation is shown in Fig.70. The achieved spatial accuracy is around 0.4 mm, see Fig.71 for the X1 plane. The calculated inverse drift velocity is $\approx 14.5 nsec/mm$. This is in good agreement with the properties of the used gas.

9.8 Results of the test

9.8.1 Major results of the test with gas mixture Ar/CO_2

The major results of the laboratory RW FSP test in 2005 are the following:

- The shielding was much improved. The prototype reliably operates with the very low threshold of 10mV $\approx 3fC$;
- The cosmic muon hit profiles were seen very clearly. Time jitter distributions looked close to expected ones. All planes behave equally;
- Efficiency curves were measured for various high voltages and threshold values;
- A spatial accuracy of $\approx 0.4mm$ was achieved. The spatial accuracy might be improved by better alignment. The calculated inverse drift velocity is $\approx 20nsec/mm$.

The efficiency curve and spatial accuracy measurements are in good agreement with 2004 ones.

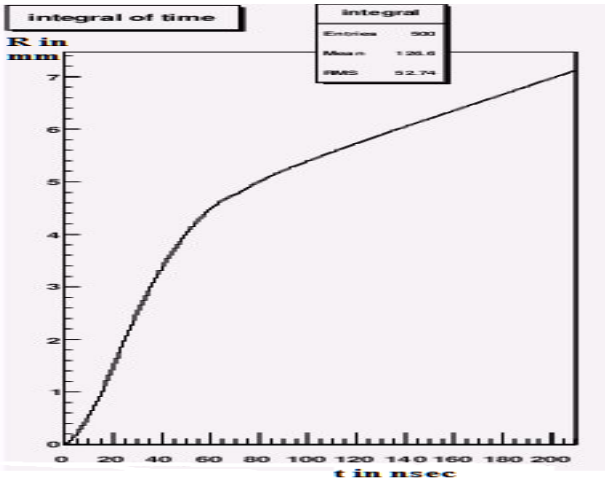

Figure 70: *The $R(t)$ relation.*

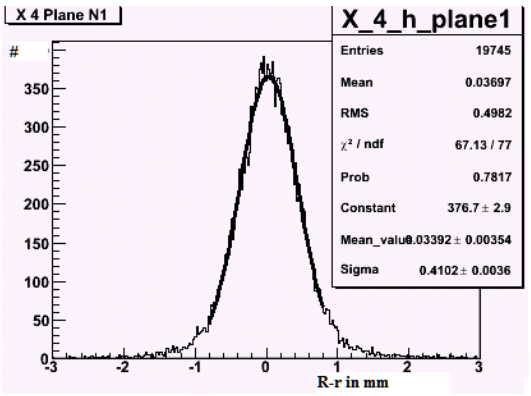

Figure 71: *Spatial accuracy of plane X1, uppermost plane in X-direction.*

9.8.2 Major results of the test with gas mixture $Ar/CO_2/CF_4$

The major results with the gas mixture $Ar/CO_2/CF_4$ are the following :

- The prototype can be operated with a low threshold of $\approx$ 3–4fC;
- The width and shape of the drift time spectra and muon hit profiles are close to the expected ones;
- The measured efficiency curves manifest the expected behavior. The plateau width was found to be larger than 150V;
- The measured spatial accuracy of $\approx 0.4mm$ is good enough.

9.9 Conclusions of the 2005 test

The laboratory test of the RW FSP was successfully performed. The test results of 2004 with the gas mixture Ar/CO_2 are in good agreement with that of 2005. The lower values of the electronics threshold were achieved by improving the screening and grounding of the prototype. The detector behavior is better understood now. The measurements with the gas mixture $Ar/CO_2/CF_4$ provide good result as well: the detector operation is stable with a very low threshold value ($\approx$ 3–4fC) and efficiency is high at rather low high voltage (2100 V).

10 Rich Wall detector operation during the 2006 data taking

After the successful tests of the full size prototype of the Rich Wall detector in the years 2004 and 2005 the decision was taken to install the Rich Wall detector in the COMPASS experimental hall and to include it in the spectrometer setup.

10.1 Assembly of the Rich Wall detector

10.1.1 Clean area assembly

The first stage of the assembling and testing of the detector took place in the COMPASSs experiments clean area. Here the following tests of MDTs took place: high voltage, gas tightness and wire tension. Also the shape and planarity of support frames (see Figs. 37, 72) were examined again (after transportation from Dubna).

Figure 72: *Clean area, storage place for MDTs and small aluminum support frames are shown.*

Those MDTs which passed successfully the test procedures were mounted onto the frames and transported to the COMPASS experimental hall for the final assembly into the Rich Wall detector.

10.1.2 Mounting and readout electronics installation in the COMPASS experimental hall

The second stage of mechanical assembly consisted in testing the RW suspension system (seen as cross-bars on Fig. 36) by 8 tonn weight (25% in excess of a nominal one). After that the suspension was mounted in the hall on the concrete blocks, in so-called 'park' position for further integration of the RW sub-modules.

The frames with MDTs were assembled in sub-modules by hanging onto the suspension cross-bar one by one till the final configuration of RW module was achieved, see Fig. 73. After that all gas pipe interconnections were made and HV and signal wiring has started. The RW was connected to a temporary gas system - $Ar/CO_2(70\%/30\%)$ - and high voltage tests have started piece by piece depending on the gas exchange ratio

Figure 73: *Rich Wall in "park" position, without FE electronics.*

(required minimum was set to 5 volumes). The convertor plates were mounted in parallel with this test process.

After a positive outcome of the high voltage test, that has demonstrated that the movement from the clean area to the experimental hall did not created any damage to the MDTs and they are all ready for operation, the analog FE boards installation was started. Due to a very delicate and sometime heavily accessible construction of the Rich Wall readout this task took much time requiring a very careful installation and pinning(each wire being readout by a separate cable required 4032 pins to be plugged by hand in the right positions).

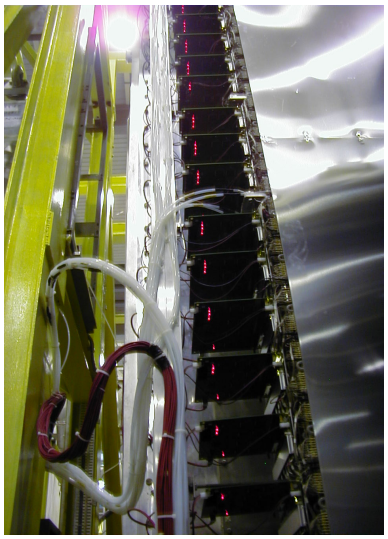

Figure 74: *Rich Wall in work position, with FE electronics.*

After the FE boards mounting was finished one additional test for the rigidity of the support structure under the full weight of around 7 tonn was made and showed no problem. The detector was prepared to be moved to its work position. The movement to

the work position was performed by the crane of the experimental hall, so that no major dismounting was required (apart of some FE boards that could have been damaged if not dismounted). The Rich Wall detector with fully installed FE cards, gas pipes and HV cables is shown on Figs. 74, 75.

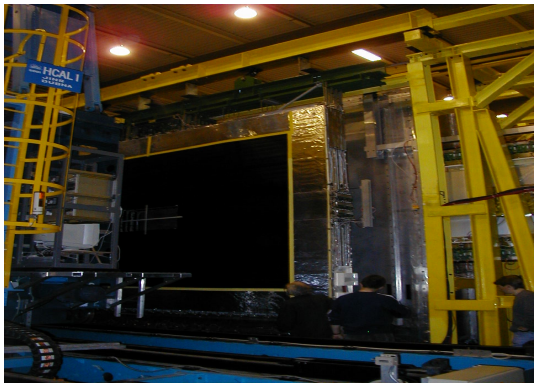

Figure 75: *Rich Wall at work position.*

The detector was installed at its nominal position ≈ 10m downstream the target, just behind the RICH 1 and just in front of the electromagnetic calorimeter for which it will act as a preshower.

10.2 Insertion in the online monitoring

For being able to check the operation of a detector in COMPASS experiment during the data taking it should be added to the monitoring software framework. The basic steps were known from the experience with the full size prototype during the 2004 test in the experimental hall. But for the whole detector implementation an update was required for the mappings and for the classes describing the Rich Wall detector, that was much bigger than the prototype in the COOOL software. After this was done all the online information became available(see Fig. 76). We can clearly see that the hit profile is as one would expect given that the beam axis is at the center of the detector.

Having the monitoring data available it was possible to carry out another procedure for a correct data treatment. That is to set the correct calibration for the $T0$ value. The $T0$ is basically the reply time of the spectrometer trigger system to a triggering coincidence as seen by the detectors front-end electronics. So it is the time difference between the moment when the event effectively happened and the instant when the information that the event should be stored(send out to the DAQ) arrive to the detector electronics from the trigger system logic(see Fig.77).

The $T0$ parameter can be found from the hit time distributions of the detector (see Fig. 78). The distribution can be broaden by the readout window increasing and shifted by the adjustment of the LATENCY parameter of the front-end electronic. When the rising front of the hit time distribution becomes visible a fit may be applied in order to determine the beginning of the front that will give us the required for the reconstruction $T0$ parameter.

Another new task consisted in the modification of the decoding of the raw data. The detector in its final configuration was readout through the multiplexers, that were

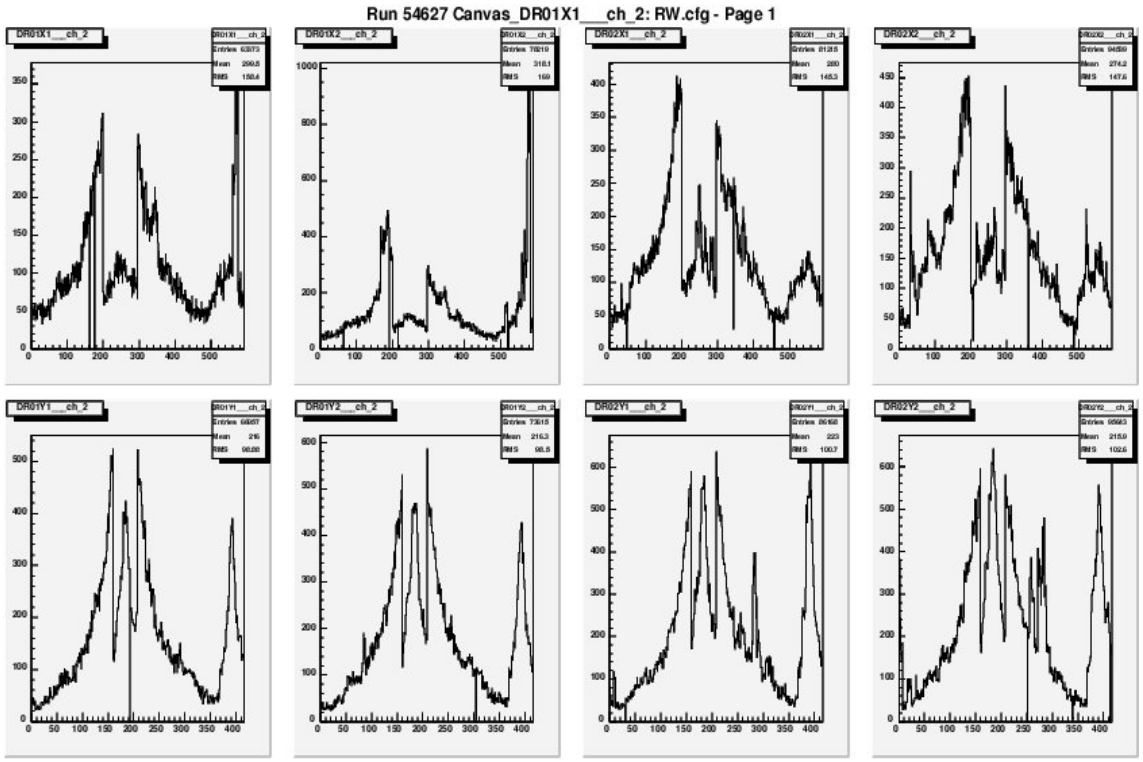

Figure 76: *Example of a hit profile from 2006 data taking.*

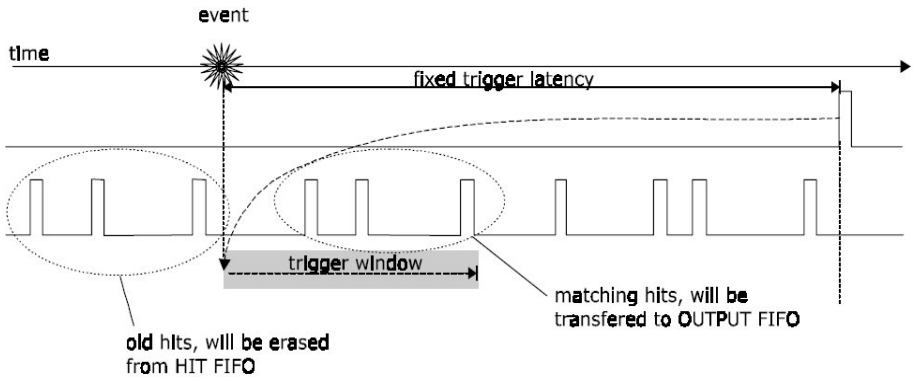

Figure 77: *Trigger matching scheme.*

not used during the prototype tests and had a different raw data format, new to the COMPASS decoding software. After the decoding was fixed all the error data words were added to the MerphyTV(the software that gives us in the online monitoring the information about the observed errors in the different detectors raw data flow). This helped to perform fast enough the initial debugging and to individuate some issues with the timing observed in the 2006 run on the Rich Wall detector.

10.3 Data reconstruction in CORAL

In the COMPASS experiment the main tool for the offline analysis of the collected data is the CORAL software. The CORAL is a flexible C++ software where each equipment is

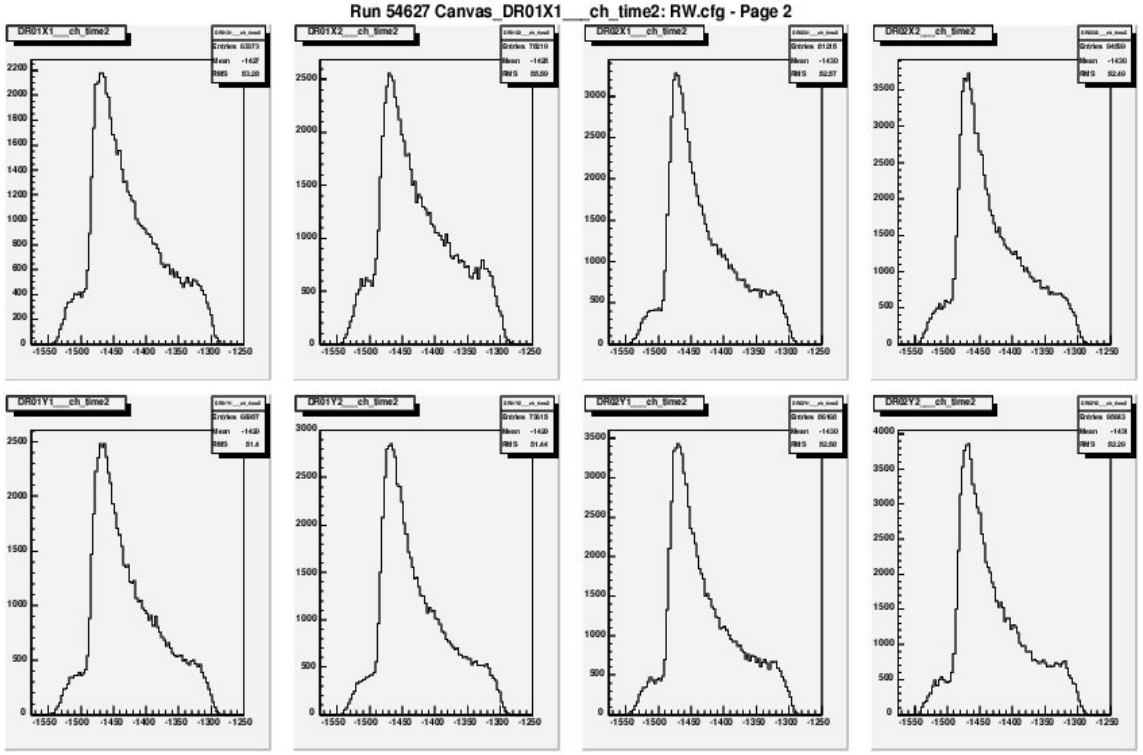

Figure 78: *Example of hit time distributions from COOOL online monitoring.*

represented by its own class, so the main work consisted in creating this class in a conform way, so that it could be implemented without any changes to the main framework. For each tracking detector the main steps of a hit reconstruction in CORAL are:

- Creation of data digits. At this stage the raw data that has arrived from the detector and was stored by the DAQ is treated and decoded to reduce it to the form of the fired detector wire and the corresponding time mark of the event.

- Correction of registered event time to the signal propagation time. The need of this operation is due to the fact that our detector is working in the drift time measurement mode and we need to know the exact drift time. Having up to 5 meters long wires we cannot anymore neglect the signal propagation issue because two events that would have happen on the different extremities of the wire "simultaneously" would not have the same registered drift time as should but with the difference of $v_{prop} \cdot l_{wire}$. That in the case of the Rich Wall detector could be $v_{prop} \cdot l_{wire} = 3ns/m \cdot 5m = 15ns$ and having the measured drift speed in the gas mixture of $\approx 20\frac{ns}{mm}$ we obtain an uncertainty of $0.75mm$. Taking in account this peculiarity all our events are corrected by the appropriate time depending on their position along the hitted wire.

- Creation of the clusters. The clusters are the objects associated to any hit that then are processed in all the track reconstruction procedures. Those objects are created on the basis of the digits with the corrected time and an additional check on the left/right up/down ambiguity of the track with respect to the hitted detector wire.

The information about the wire number is not present in the cluster object instead the cluster store the coordinate of the hitted wire and the z position of the detector plane in the COMPASS laboratory frame as references.

The chain of the data processing for the Rich Wall detector is illustrated by the Fig. 79, that shows the different steps of the reconstruction for the Rich Wall data. One of the points to check correctness of the data reconstruction is to look at the reconstructed positions of the wires in the COMPASS laboratory reference frame(see Fig. 79c). Also from in the Fig. 79c we clearly see the additional tube by tube spacing. This means that the internal structure of the detector is reconstructed as it should be. Also one needs to check the extremities coordinates of the reconstructed hit profile in the COMPASS laboratory reference system. This is necessary because the position of the detector is taken from special mapping files, that are created according to a special geometrical survey procedure carried out in the experimental hall.

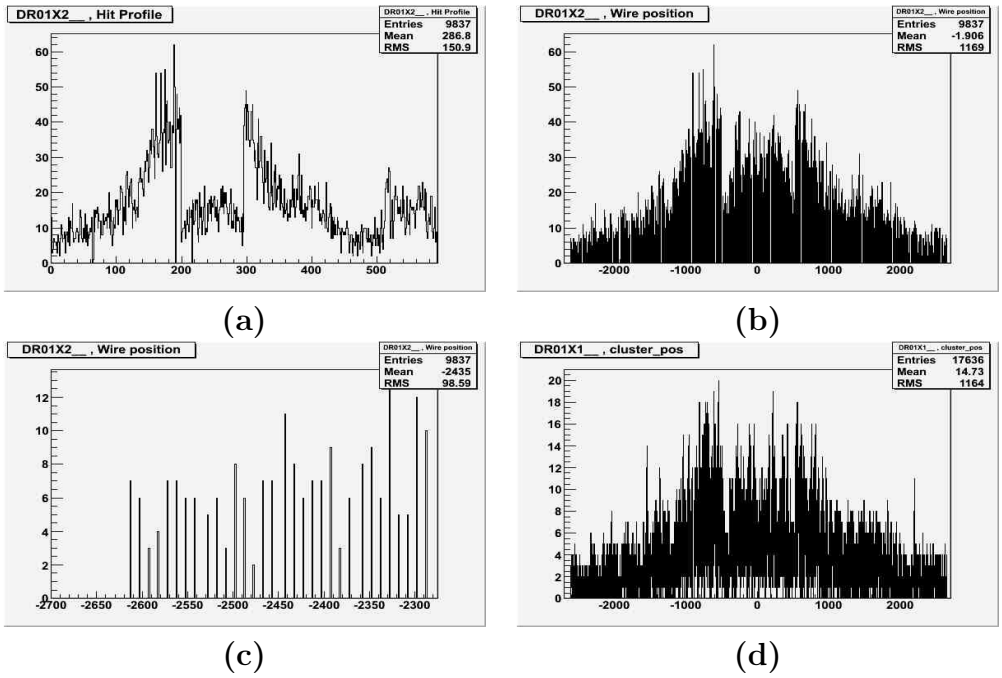

Figure 79: (a) Show the hit profile. (b) The wire position reconstruction. (c) Wire by wire profile. (d) The reconstructed clusters positions.

10.4 2006 data taking preliminary results

During the 2006 data taking the Rich Wall detector was operated at a high voltage of $2050V$, that was chosen on the basis of the results from the tests of the Rich Wall full size prototype and as a compromise between possible ageing danger and the possibility for setting higher thresholds to reduce eventual noise issues. The thresholds according to the results of the RW FSP tests were set to 5fC on the main part of the detector and to 6fC on the few most noisy channels. Both thresholds are still in the region of high efficiency plateau (Fig. 49) for the chosen operational voltage. We saw that even in a

very noisy environment of the experimental hall only a few noisy channels were present and a low enough threshold was possible (see Fig. 80).

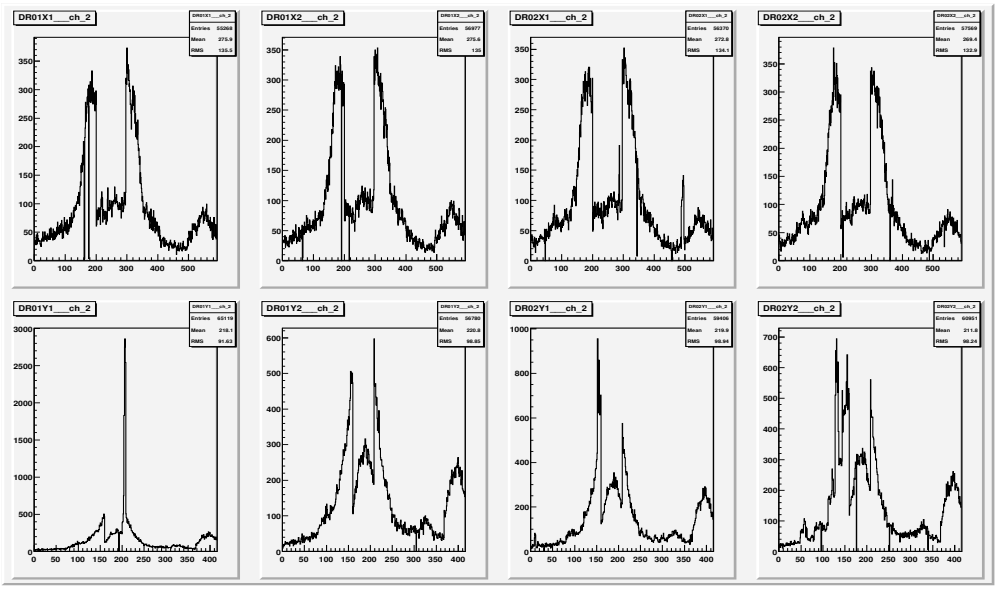

Figure 80: *Example of COOOL online monitoring with well visible dead channels.*

From the small amount of the analyzed yet 2006 data it is difficult to make a final definitive statement on the Rich Wall performances, but all the preliminary checks show that the efficiency and spatial accuracy values defined in the project proposal of the Rich Wall detector [73] were reached (see Fig. 81).

Basing ourselves on the experience of operation of the Rich Wall detector during the 2006 data taking period we can conclude that the project was successfully realized. Presently the detector demonstrates stable operation and all the eventually appeared issues were understood in a brief time.

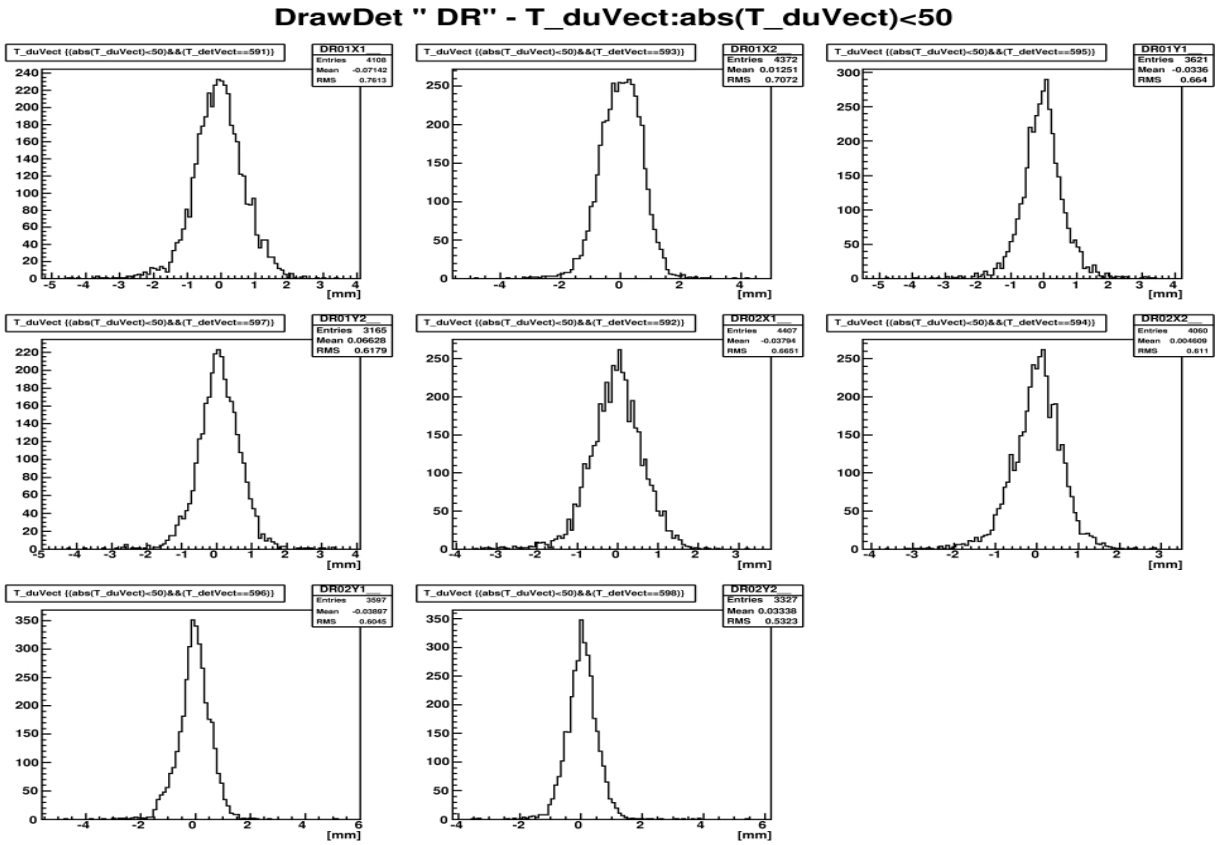

Figure 81: *Rich Wall spatial accuracy, preliminary results for different parts of RW vary within 5 to 7,5 mm in r.m.s.*

11 Development of a Multiplexer for the Rich Wall detector readout

11.1 Purpose

To provide the readout of the Rich Wall detector it was decided to implement a data multiplexer in the front-end readout chain. This was done to give the possibility to readout all the channels in spite of a small number of available Hot-Link connections of the Catch. Moreover, it was convenient from the point of view of the future development and resource economy. The simplified scheme of the operation of the developed multiplexer is presented on the Fig. 82.

We see that through one multiplexer we can connect 8 FE boards to a single Catch Hot-Link input. Also from the Fig. 82 we see that the multiplexer should be realized in a transparent form from the point of view of the data flow between the Catch and the FE boards. This is needed to guarantee an equivalence of this readout scheme to the previously used one with the direct Catch to FE board Hot-Link connection. But in the same time the multiplexer itself should analyze the data going from the Catch to the FE boards and in the opposite direction. It is necessary to provide the synchronization of the front-end and to find possible data inconsistencies. We can see that by the implementation of this data multiplexer an economy of 3 Catche modules was achieved, worth mentioning

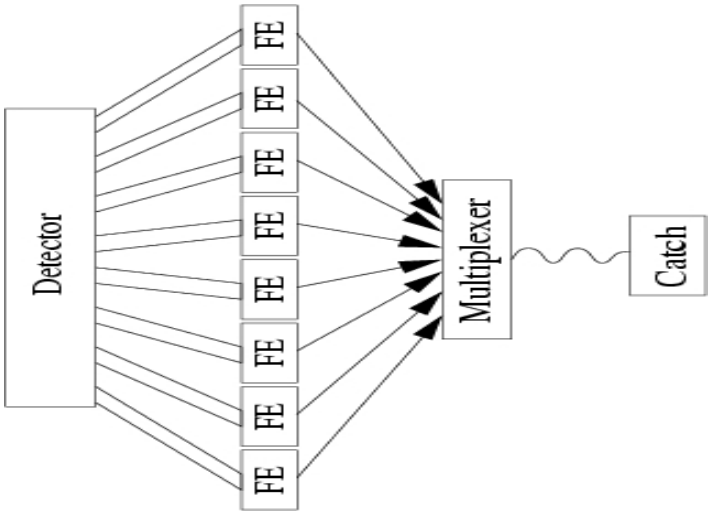

Figure 82: *Scheme of the Rich Wall readout with the multiplexer.*

that if a readout without the multiplexer would be installed in COMPASS this would have required a considerable work due to the absence of any free slots for the three eventual Catche modules at the Rich Wall detector installation position in the COMPASS spectrometer experimental hall.

It was decided to use for the data multiplexer development an already available and proven in the COMPASS experiment multifunctional digital board created around the Xilinx FPGA chip, the HotGeSiCA(see Fig. 83) board.

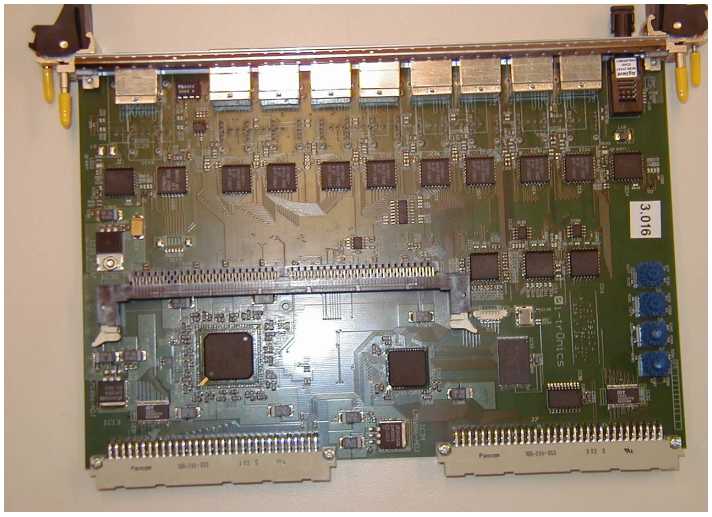

Figure 83: *The HotGeSiCA board.*

The main requests for the multiplexer were:

- A very robust to failure design. Any failure of the logic could lead to an error generation and to an eventual crash of the whole DAQ chain of the entire experiment.
- Reliable for the future without any hardware updates. It was mandatory to achieve a stable operation at trigger rates of 100 kHz, this is requirement for all DAQ pieces

that is mentioned in the COMPASS proposal [1].

- Easy introduction of this new hardware in the COMPASSs DAQ scheme. This was an important issue due to a very short development time line and to the fact that all the rest of the readout chain was defined earlier and no major work on it was possible anymore.

11.2 Description of the digital board

This board is based on the GeSiCA readout driver. The GeSiCA is an acronym for GEm and SIlicon Control and Acquisition module. Initially the module was designed as a readout module of the GEM and silicon detectors.

The tasks of the GeSiCA module are to distribute the reset signals, the TCS (Trigger Control Signal) and the clock to the front-end cards, to collect the data from the front-end cards and to transfer these data to the readout buffer PCs via a S-Link interface. In addition it provides a slow bidirectional interface for the configuration of the front-end cards.

The GeSiCA is a 9U VME module which has a set of interfaces: the VME interface, four front-end interfaces, a S-Link interface and the TCS-receiver interface. The front-end interface is a serial optical link with a speed of 40Mbit/s from the GeSiCA to the front-end card and 400 Mbit/s backward. The custom protocol provides two independent data channels over this optical link. Via the first channel the front-end card receives the trigger signal and sends back the corresponding data from the detector. The second channel is used for programming the front-end card, for loading firmware, setting thresholds and verifying the status. The second channel is an optical implementation of the I2C protocol. The I2C master is implemented in the GeSiCA FPGA and it is controlled by a user program via the VME interface. The TCS receiver is attached to the P2 connector and provides the TCS clock, the trigger signal and the event identification information. During the data acquisition the GeSiCA receives data from four front-end cards in parallel. The serial data are parallelized, checked for consistency and put into the FIFO memories. Every event data block is marked by a header and a trailer. The outputs of the four FIFO memories are connected to the merger via a common bus. For every event the merger creates an S-Link header, which consists of the TCS event identifier, the GeSiCA ID and the block size. The merger sequentially sends the S-Link header and then four data blocks via the S-Link card to the readout buffer machine. The total bandwidth of the four front-end interfaces is equal to the bandwidth of the S-Link interface. Such balanced design minimizes the internal buffer sizes and excludes any data losses inside the GeSiCA.

The HotGeSiCA has the same functionality as the GeSiCA module, however it has new features. First of all it is a 6U VME module. The TCS receiver is integrated inside the module and does not occupy the P2 connector. Instead the P2 connector is used for the S-Link card. The number of the front-end interfaces was increased to eight together with increasing the internal FIFO memory up to 512 MByte. During production the HotGeSiCA module can be equipped either with optical front-end interfaces or copper connectors depending on the type of the front-end electronics to be attached to the module.

11.3 Electronics test

The testing of the HotGeSiCA board electronic part took place on a test stand where conditions close to the experimental one were created. We needed to test that all the TCS(Trigger Control Signal) were transmitted and that all the communication between the Catch and the FE board was synchronous to the respective clocks. All those tasks were performed with the use of an oscillograph to evaluate delays and the synchronization of the signals. It was very important to keep everything synchronized to the 40 MHz(38.88 MHz) clock that is the main reference clock of the COMPASS experiment. Moreover a part of the developed for the FPGA chip firmware needed to be tested with the oscillograph. The reason for this was that the firmware logic provided control sequences(Reset, Syncreset, Begin of spill, End of spill signals) for the connected FE boards. Those control sequences were sent from the Catch to the Multiplexer board where they were decoded, worked out then coded again to be sent to the FE boards by a serial data line synchronously to a 10 MHz clock (Instead of the 40 MHz). All those tests were performed and the results meet our expectations. Moreover, it was found that due to the fact that it was the first bunch of HotGeSiCA boards with copper connectors instead of the optical front-end interface, some problems with the board printed circuit were found and corrected.

11.4 General line of the firmware development

The main task resulted to develop a completely new firmware for the Xilinx FPGA chip of the HotGeSiCA board. That FPGA firmware needs to incorporate all the treatment of the data, triggers, and other service signals that are arriving from the Catch. All of them need to be multiplexed and sent to the correct FE boards. In contrary, data flow that arrives from the front-end boards after an error check and the multiplexing needs to be send out back to the Catch. To fulfill the task a highly pipelined logical architecture was designed and implemented in the FPGA chip. Main ideology of the multiplexer logic responsible for the main data flux in the direction to the Catch is shown on the Fig. 84.

We see that for decoupling different signals and for providing a good data processing performance one needs to use logical parts synchronized to different reference clocks. On the Fig. 84 one may see that all the data arriving through Hot-Links from the FE boards to the Multiplexer are first treated by the individual for each Hot-Link input logical module that check its quality and then is put to the asynchronous FIFO. All these pieces works synchronously to the clock of the respective Hot-Link and are independent. The asynchronous FIFO is working as a reference clock decoupling element. Having all the data stored in the asynchronous FIFO we can then use any reference clock to read it out.

We use a pipelined reading logical module the READER that enhances the speed of the data extraction from the FIFO (in the case of heavy data flow from the port) to a different reference clock region and performs the merging of the 10 bit data words arriving from the Hot-Link reading logical block to the 30 bit data words where the original 24 bit data of the front-end electronics and the internal to the multiplexer logic information are contained.

Being now sure about each individual 30 bit data word correctness we need to analyze the data flow as a whole to check its consistency. This is done in a logical block called the FORMATTER that takes the 30 bit data arriving from the READER block, performs all the needed consistency checks, add some service information to each data word and

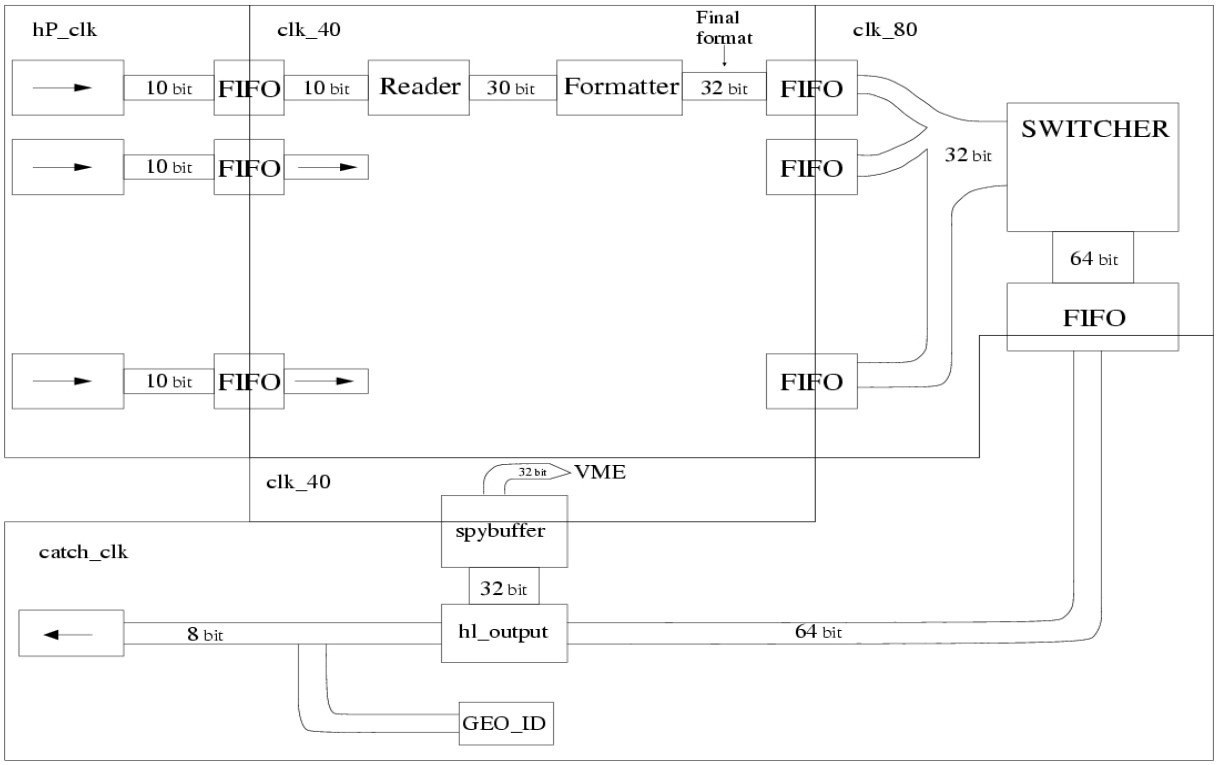

Figure 84: *The HotGeSiCA board logic implementation.*

then sends the resulting 32 bit data further into an another asynchronous FIFO. Those operations are done in a logical domain that uses the internal 40 MHz reference clock that is generated on the HotGeSiCa board itself and is distributed around the FPGA chip.

One of the difficulties of any multiplexing device is that it needs to perform the multiplexing of the data from different sources without loosing time on the operation itself, on the sources switching and in our case, having the eight times lower output bandwidth than the input one. The resulting from those difficulties conclusion is that it should absolutely be able to store some amount of the data internally and have the logical part that is running the multiplexing algorithm working at higher than the incoming data reference clock frequencies. So, the implementation of a logical part working at 80 MHz instead of the standard for the rest of the FPGA chip 40 MHz reference clock frequency was chosen. This choice was a compromise between the technical restriction of the chip and availability of the programmable logic units in it. More precisely the compromise in the firmware for a FPGA chip relies on the fact that lower is the clock frequency on a logical module, weaker are the restrictions on the signal pass lengths during the internal gates optimization of the chip, higher is the packing density of the logics that could be achieved. From the Fig. 84 we see that the need for a faster clock is obvious if we want to maintain the data flux at its maximum because the data from the 8 inputs needs to be put to the main FIFO, and for this operation we need to read the data in a sequential port by port fashion but the data is arriving to the ports in a parallel way, so during the reading of the data from the first input data flux(first Hot-Link for example) the FIFOs of other ports will start filling. Such a situation could become dangerous in the

case of a heavy data flow from the sources coupled to a short delay between the triggers, this will fill out the small input buffers before we empty out them by reading the data out and sending it to the main deep FIFO buffer. All the readout of the data from the different input ports FIFOs, switching between input ports data fluxes, treatment of the data and its transferring to the main FIFO is done by the SWITCHER logical block. In the present implementation it is working synchronously to a 80 MHz reference clock and is writing the data to the main FIFO buffer in a 64 bit format that is made by putting two 32 bit data words together. The 64 bit format was chosen for eventual future developments, because it is the standard data word dimension for the external memory driver, that could be implemented. The main FIFO has a 2048 depth for 64 bit data words (that is ≈16.4 KB), this is large enough knowing that the average data word count per multiplexer is small (see Fig. 89). In the future it is possible to extend this memory by adding external DIMM memory of 512MB. The last big logical part constituting the global multiplexer's logic is the part responsible for the data extraction from the main 64 bit FIFO buffer and for its sending to the Catch or to the SpyBuffer, depending on the type of the readout that is used. To send the data to the Catch it is needed to be reformatted to the 8 bit data format that corresponds to the Hot-Link capacity (plus two service bits). Apart of the reformatting of data any event as a whole gets two additional data words generated by the multiplexer, that are the event header and the event trailer of the specific to the COMPASS DAQ format. In the event header and the event trailer data words the information about the Geografical address (an individual GeoID is attributed to each multiplexer to give the possibility to distinguish in the data flow their respective data flows) of the multiplexer and the event number are stored, so that further in the data acquisition chain it is possible to check the consistency of the data confronting the event numbers. All those operations are performed synchronously to the 40 MHz reference clock that comes from the Catch via the Hot-Link, and all the data are sent out synchronously to it. That functionality is provided by the logical blocks "hl_reader" and "spybuffer"(the spybuffer has its own small asynchronous FIFO and is responsible for sending the output data to the VME bus).

11.5 Serial data transfer implementation

From the beginning it was decided to make the multiplexer transparent to the serial data flow from the Catch to the FE boards. But the difficulty arises from the fact that the multiplexer should not simply send the serial data (FE boards initialization data, for example) arriving from the Catch to all the 8 connected FE boards, but should send it only to one of them where the data are directed to. Due to this it is not anymore possible to send data without making an analysis of what data it is. It was decided to define several specific to the multiplexer commands shown on the Fig. 85, that can give us the possibility to control its operation.

The basic difference of those commands from the normal serial data is that it does not have the standard starting bit sequence but has instead "111" pattern. The rest of the command is its index and an eight bit patter indicating to which ports of the multiplexer the command should be applied. With this implementation we can control all the connected FE boards separately for loading their parameters. The three presently used serial commands give us the following possibility:

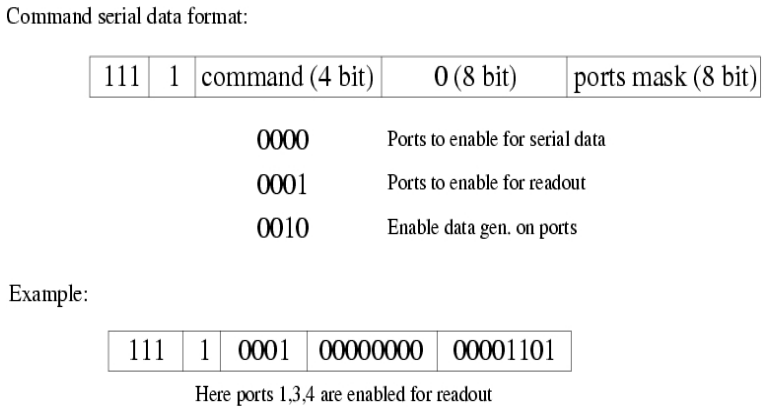

Figure 85: *Serial data words.*

- To initialize the front-end boards in a consecutive way. It is done in the following way: we enable one port for transmitting the serial data(command "0000" and mask with only one enable bit), send the initialization data from the Catch, then habilitating another port we send its initialization information from the Catch and so on.
- To work with an incomplete multiplexer loading. This is needed when one or more ports of the multiplexer are not used in the data tacking. This is very important for the operation flexibility, for eventual problems with the front-end boards and for debugging. All the modification of the internal multiplexing logic of the FPGA chip are done automaticly (switching on/off of the input data sources) at the arrival of the serial command.
- We can also generate a certain pattern of the incoming data internally. An internal data generator is implemented in the firmware of the FPGA chip, so we can use it for the debugging purposes of each individual input port even during the normal operation of all the other input ports.

In the future if needed more serial commands could be implemented.

11.6 Output data format

From the default request of using the data formats already present in COMPASS experiment it was decided to use 32 bit ADC data format, that gives us the possibility to add to the 24 bit front-end board's data some necessary additional information. This information is needed to specify the port of the multiplexer where the data is coming from, the geographic address of the multiplexer, to distinguish between them and the event number to check the consistency of the data. The data words present in the multiplexer output format are shown on the Fig. 86.

The defined data words are arranged in a data sequence that is presented on the Fig. 87, where the structure of one events data is shown in the way it is sent out from the multiplexer to the Catch.

The Fig. 87 presents the data sequence as it would be seen by the Catch in the case of the maximal configuration, that means 8 ports per multiplexer are active and all the

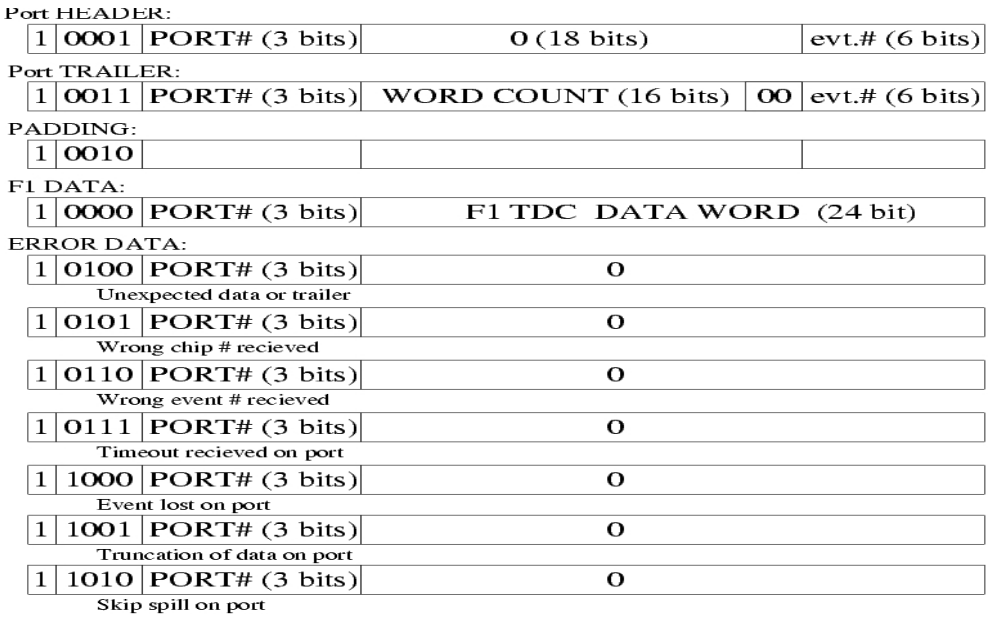

Figure 86: *Multiplexers output data format.*

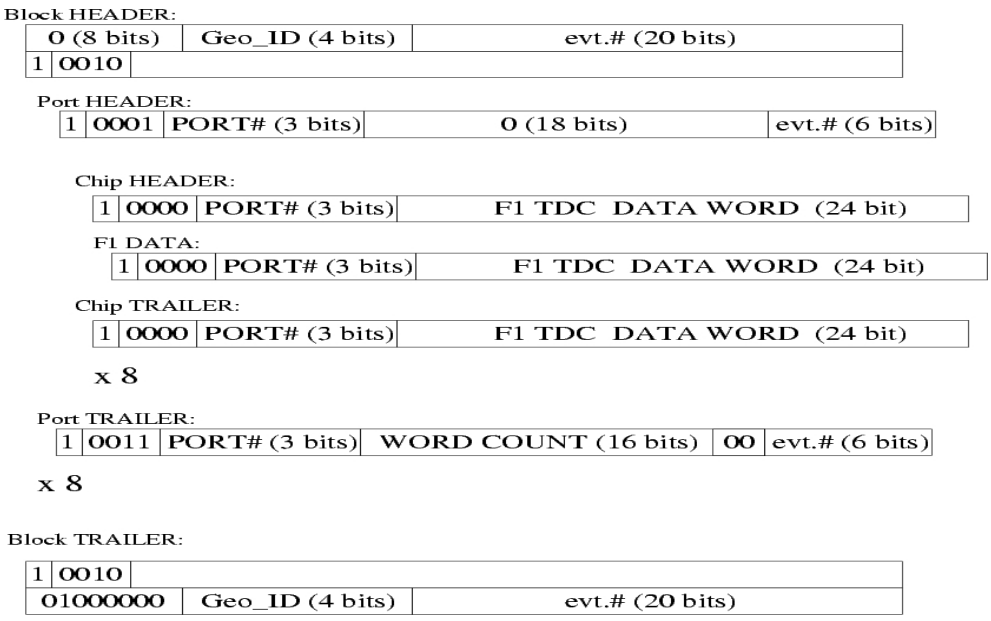

Figure 87: *The output data sequence.*

8 multiplexers used to readout the Rich Wall detector are included in the readout, this is the reason for the 8× signs on the figure. The PADDING data word is a peculiar of our internal logical realization of the multiplexers firmware. It is due to the fact that we have one internal transformation from the 32 bit data words to the 64 bit data words format and this implies a complication that is due to the possibility of an odd 32 bit data words number. In such a case we had two possibilities. To check if one 64 bit data word is composed of 32 bit data words belonging to one or different events. This would have required much additional logic working at high clock rate and was difficult to implement. A second possibility was adopted, the check on the 32 bit data words number in each

event is performed and in the case the data word number is odd a dummy data word called PADDING is added to complete the last 64 bit data word of the event.

Obviously to have the possibility, if necessary, to reduce the whole data flow from the multiplexer, an option to truncate from the output data the PADDING data words was also implemented. We can also truncate the Port HEADER and TRAILER data words, because this information is excessive and is by definition already included in the 32 bit data word header created in the FORMATTER. Same can be applied to the chip HEADER and TRAILER that comes from the front-end boards, as all the information present in them is included in the 24 bit data itself.

Summarizing we have a flexible data flux dimension that gives us the possibility to do an easy debugging and to reduce the data flux to the minimum, if needed. All this is done only through software control, there is no need of an intervention to the hardware.

11.7 Simulation

The testing from scratch on the real data of the logical functioning of an FPGA firmware is very difficult. Special tools exist so that one can simulate the logical operation, trying to create all the different situations that are expected during the real data taking. This simplifies the development work and shortens the testing times. Unfortunately not always even such situation tools as Simulink and ModelSim can provide a fully "real" results on a big logical design. On Fig. 88 one can see an example of a simulation, that shows the logical functioning of the firmware after the arrival of a trigger to the logic.

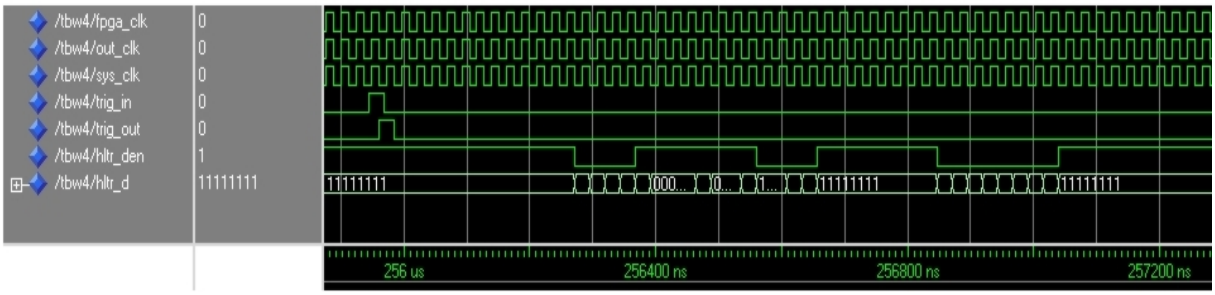

Figure 88: *An example of the FPGA logic implementation simulation*

On the Fig. 88 for simplicity reasons the signal time propagation internal to the FPGA chip was not taken into account during the simulation.

11.8 Operation during the 2006 data taking

After the development and testing phazes the firmware was used during the 2006 COMPASS data taking. All the implemented logic performed as expected. Only one issue appeared, the highly buffered scheme of the multiplexers firmware logic, creates a large delay of the first data word sent to the Catch after the trigger arrival. The observed and simulated times are of the order of 5-7 μs (see Fig. 88). In some cases where the event size (see Fig. 89) is large due to a present Catch restriction of 12 mks on the maximal time length after the trigger arrival that can be used to send out the data, we observed the truncation of the multiplexers data(1-3%). This issue will be solved for the 2007 data

taking period by the introduction of some changes in the DAQ scheme that will cancel the present restriction on the data sending time.

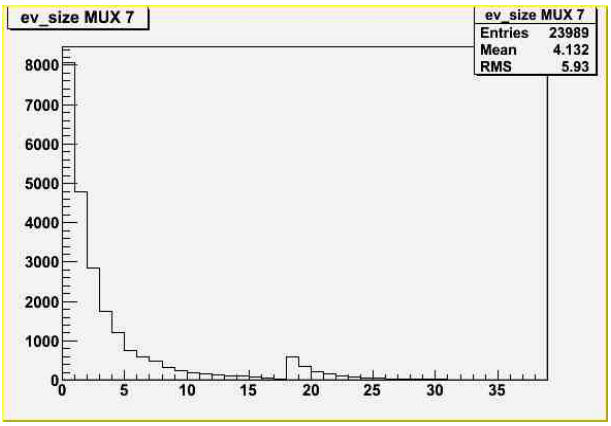

Figure 89: *Data flux through a multiplexer. In "useful" data words per trigger.*

12 Conclusions

A complete analysis of the transversely polarized Λ hyperon decay was performed on the whole 2002-2004 COMPASS experimental data sample. For the first time the 2004 data sample was included in the transverse polarization extraction analysis, that has increased the statistics almost twofold compared to the initial one of the years 2002-2003. A complete cross-check of the result of the analysis was done by an independent group that has confirmed the accuracy of our measurement. Furthermore an estimation of the systematic error was performed using different methods and it was found that at present state the systematic error contribution to our result is smaller than the statistical one. Presently the measured values of the Λ polarization are compatible with zero in all the accessible x range. The mean value averaged over the whole x range is found to be

$$P_\Lambda^T = -6 \pm 7\% \tag{81}$$

The result must be compared to the theoretical prediction of Eq. 80 where 1% upper estimate was given.

The complete procedure for the testing, integration and commissioning of the new Rich Wall detector in the COMPASS spectrometer was elaborated and performed. The tests of the RW prototype were performed during the years 2004 and 2005. They included an extensive testing of the new front-end electronics compatibility with the detector hardware and a detailed study of the operational performance with different gas mixtures. A complete test of the RW prototype detector in the real COMPASS environment during 2004 year RUN was performed. The prototype was successfully integrated in the COMPASS DAQ and monitoring systems. During the 2006 a new VME-based module, called the Hot-Link Multiplexer, was developed, tested, and commissioned. This module allows us to finalize the DAQ chain of the Rich Wall detector. During the 2006 data taking a complete description of the Rich Wall detector was included in the COMPASS data reconstruction software that gave the possibility to analyze the available data. On the basis of the preliminary 2006 RUN data analysis the expected performance of the Rich Wall detector was confirmed. A spatial resolution of 0.5-0.7 mm in r.m.s. was achieved (without an internal alignment). Just a few $(0.5\% - 0.7\%)$ noisy or dead channels were observed. Also a very low (about 2%) error rate in the readout of the Rich Wall via the multiplexer was observed and all the reasons that caused it were understood. Thus, in spite of very tight schedule the RW detector project was successfully accomplished.

13 Acknowledgment

First greeting I would like to address to my supervisor Prof. Daniele Panzieri who was always available to any question, supported the work at all stages and at any necessity also he was an absolutely open a sincere person. This circumstances gave me the possibility to fulfill all the planned work. I would like to thank Dott. Andrea Ferrero for a considerable contribution in the thesis preparation, for the constant support during the work and for a very friendly personal approach. Also I would like to exprime my gratitude to the colleagues from the Dubna group and to Dott. O. Denisov, our discussions were extremely useful for my better understanding of the Rich Wall detector thematic. A big "thank you" to my colleagues Dott. A. Prokudin and Prof. A. Kotzinian that helped me with their profound knowledge of the transverse Λ^0 polarization subject that I was studying. Concluding, many thanks to the whole Torino group they made my work on the thesis and the stay at Torino a very pleasant experience.

Apart of that I exprime my greatest gratitude to my family, all of them supported me throughout all this experience and this support was absolutely indispensable.

References

[1] COMPASS, A Proposal for a COmmon Muon and Proton Apparatus for Structure and Spectroscopy, CERN/SPSLC 96-14, SPSLC/P297, 1996.

[2] C. G. . Callan and D. J. Gross, Phys. Rev. Lett. **22** (1969) 156.

[3] J. D. Bjorken, Phys. Rev. **148** (1966) 1467.

[4] E.W. Hughes and R. Voss, Annu. Rev. Nucl. Part. Sci. 49 (1999),303.

[5] J. R. Ellis and R. L. Jaffe, Phys. Rev. D **9** (1974) 1444 [Erratum-ibid. D **10** (1974) 1669].

[6] R. D. Carlitz, J. C. Collins and A. H. Mueller, Phys. Lett. B **214** (1988) 229.

[7] P. G. Ratcliffe, Phys. Lett. B **365** (1996) 383 [arXiv:hep-ph/9509237].

[8] P. G. Ratcliffe, arXiv:hep-ph/9710458.

[9] J. Ashman *et al.* [European Muon Collaboration], Phys. Lett. B **206** (1988) 364.

[10] J. R. Ellis and M. Karliner, Phys. Lett. B **341** (1995) 397 [arXiv:hep-ph/9407287].

[11] M. Anselmino, B. L. Ioffe and E. Leader, Sov. J. Nucl. Phys. **49** (1989) 136 [Yad. Fiz. **49** (1989) 214].

[12] F. Bradamante, contribution to SPIN2000 conference.

[13] D. H. Perkins. "Introduction to High Energy Physics." Addison Wesley, 3rd edition, 1987.

[14] J. Soffer. "Is the riddle of the hyperon polarizations solved?" In *Hyperon '99*: Hyperon Physics Symposium, Batavia, Illinois, USA, September 1999.

[15] G. Bunce et al. "Λ hyperon polarization in inclusive production by 300 GeV protons on beryllium." *Phys. Rev. Lett. 36*, 1113-1116 (1976).

[16] K. J. Heller et al. "Polarization of Λ and $\bar{\Lambda}$ produced by 400 GeV protons." *Phys. Rev. Lett.* 41, 607 (1978).

[17] B. Lundberg et al. "Polarization in inclusive Λ and $\bar{\Lambda}$ production at large p_T." *Phys. Rev.* D40, 3557-3567 (1989).

[18] E. J. Ramberg et al. "Polarization of Λ and $\bar{\Lambda}$ produced by 800 GeV protons." *Phys. Lett.* B338, 403-408 (1994).

[19] S. Erhan et al. "Λ polarization in proton-proton interactions at $\sqrt{s} = 53$ and 62 GeV." *Phys. Lett.* B82, 301 (1979).

[20] A. M. Smith et al. "Λ polarization in proton-proton interactions from $\sqrt{s} = 31$ to 62 GeV." *Phys. Lett.* B185, 209 (1987).

[21] V. Fanti et al. "A measurement of the transverse polarization of Λ-hyperons produced in inelastic pN-reactions at 450 GeV proton energy." *Eur. Phys. J.* C6, 265-269 (1999).

[22] A. Brandt et al. "Measurements of inclusive $\bar{\Lambda}$ production with large x_F at the $Sp\bar{p}S$ collider." *Nucl. Phys.* B519, 3-18 (1998).

[23] A. Morelos et al. "Polarization of Σ^+ and Σ^- hyperons produced by 800 GeV/c protons." *Phys. Rev. Lett.* 71, 2172-2175 (1993).

[24] P. M. Ho et al. "Measurement of the polarization and magnetic moment of Ξ^+ anti-hyperons produced by 800 GeV/c protons." *Phys. Rev.* D44, 3402-3418 (1991).

[25] S. A. Gourlay et al. "Polarization of Λ's and $\bar{\Lambda}$'s in pp, $\bar{p}p$, and K^-p interactions at 176 GeV/c." *Phys. Rev. Lett.* 56, 2244-2247 (1986).

[26] A. N. Aleev et al. "The measurement of the transverse polarization of Λ hyperons produced in nC reactions in the EXCHARM experiment." *Eur. Phys. J.* C13, 427-432 (2000).

[27] T. Henkes et al. "Further evidence for pomeron-quark interactions: Observation of large Λ polarization in $pp \to (\Lambda K^+)p$." *Phys. Lett.* B283, 155-160 (1992).

[28] A. Bravar. "Experimental overview of spin effects in hadronic interactions at high energies." In *13th International Symposium on High-Energy Spin Physics (SPIN 98)*, Protvino, Russia, September 1998.

[29] S. U. Chung, R. L. Eisner, S. D. Protopopescu, and R. D. Field. "Polarization study of inclusive Λ production in K^-p interactions." *Phys. Rev.* D11, 1010 (1975).

[30] H. Abramowicz et al. "Λ polarization in the reaction $K^- p \to \Lambda$ + anything at 14.3 GeV/c." *Nucl. Phys.* B105, 222 (1976).

[31] I. V. Ajinenko et al. "Inclusive Λ polarization in $K^+ p$ interactions at 32 and 70 GeV/c." *Phys. Lett.* B121, 183 (1983).

[32] M. I. Adamovich et al. "A measurement of Λ polarization in inclusive production by Σ^- of 340 GeV/c in C and Cu targets." *Eur. Phys. J.* C32, 221-228 (2004).

[33] D. M. Woods et al. "Polarization of Ξ^- and Ω^- hyperons produced from neutral beams." *Phys. Rev.* D54, 6610-6619 (1996).

[34] M. I. Adamovich et al. "A measurement of Ξ^- polarization in inclusive production by Σ^- of 340 GeV/c in C and Cu targets." *Eur. Phys. J.* C36, 315-321 (2004).

[35] J. Bensinger et al. "Measurement of decay parameters and polarization in inclusive Ξ^- production from $K^- p$ interactions." *Nucl. Phys.* B252, 561-577 (1985).

[36] J. Bensinger et al. "Inclusive Λ production and polarization in 16 GeV/c $\pi^- p$ interactions." *Phys. Rev. Lett.* 50, 313-316 (1983).

[37] S. Barlag et al. "A study of the transverse polarization of Λ and $\bar{\Lambda}$ hyperons produced in $\pi^- Cu$ interactions at 230 GeV/c." *Phys. Lett.* B325, 531-535 (1994).

[38] D. Aston et al. "Inclusive production of Λs and $\bar{\Lambda}$s in γp interactions for photon energies between 25 GeV and 70 GeV." *Nucl. Phys.* B195, 189 (1982).

[39] K. Abe et al. "Inclusive photoproduction of neutral strange particles at 20 GeV." *Phys. Rev.* D29, 1877 (1984).

[40] A. Brll. "Transverse polarisation of Λ and $\bar{\Lambda}$ hyperons in quasi-real photon nucleon scattering." Presented at the 15th International Spin Physics Symposium (SPIN02), Brookhaven National Lab, New York, USA, September 2002.

[41] O. Grebenyuk. "Transverse polarization of Λ and $\bar{\Lambda}$ produced inclusively in eN scattering at hermes." At 10th International Workshop on Deep Inelastic Scattering and QCD (DIS 2002), Cracow, Poland, May 2002.

[42] S. L. Belostotski and O. Grebenyuk. "Transverse polarization of Λ hyperons produced inclusively in eN-scattering at hermes." In 9th Workshop on High Energy Spin Physics, Dubna, Russia, August 2001.

[43] Bo Andersson, G. Gustafson, G. Ingelman, and T. Sjostrand. "Parton fragmentation and string dynamics." *Phys. Rept.* 97, 31 (1983).

[44] J. Szwed. "Hyperon polarization at high energies." *Phys. Lett.* B105, 403 (1981).

[45] T. A. DeGrand and H. I. Miettinen. "Models for polarization asymmetry in inclusive hadron production." *Phys. Rev.* D24, 2419-2427 (1981). Erratum ibid. D31:661, 1985.

[46] R. Barni, G. Preparata, and P. G. Ratcliffe. "A simple explanation of hyperon polarization at high p_T." *Phys. Lett.* B296, 251-255 (1992).

[47] J. Soffer and N. A. Trnqvist. "Origin of the polarization for inclusive Λ production in pp collisions." *Phys. Rev. Lett.* 68, 907-910 (1992).

[48] J. Felix. "On theoretical studies of Λ polarization." *Mod. Phys. Lett.* A14, 827-842 (1999).

[49] T. A. DeGrand and H. I. Miettinen. "Quark dynamics of polarization in inclusive hadron production." *Phys. Rev.* D23, 1227-1230 (1981).

[50] T. A. DeGrand, J. Markkanen, and H. I. Miettinen. "Hyperon polarization asymmetry: Polarized beams and Ω^- production." *Phys. Rev.* D32, 2445-2448 (1985).

[51] Y. Yamamoto, K. Kubo, and H. Toki. "Quark recombination model for spin polarization in high energy inclusive hadron reactions." *Prog. Theor. Phys.* 98, 95-128 (1997).

[52] M. Anselmino, D. Boer, U. D'Alesio, and F. Murgia. "Λ polarization from unpolarized quark fragmentation." *Phys. Rev.* D63, 054029 (2001).

[53] M. Anselmino, D. Boer, U. D'Alesio, and F. Murgia. "Λ polarization in unpolarized hadron reactions." *Czech. J. Phys.* 51, A107-A113 (2001).

[54] M. Anselmino, D. Boer, U. D'Alesio, and F. Murgia. "Transverse Λ polarization in unpolarized semi-inclusive DIS." In *9th International Workshop on Deep Inelastic Scattering (DIS 2001)*, Bologna, Italy, April 2001.

[55] M. Anselmino, D. Boer, U. D'Alesio, and F. Murgia. "Transverse Λ polarization in semi-inclusive DIS." *Phys. Rev.* D65, 114014 (2002).

[56] M. Anselmino, D. Boer, U. D'Alesio, and F. Murgia. "Transverse Λ polarization in inclusive processes." *Int. J. Mod. Phys.* A18, 1237-1246 (2003).

[57] P. J. Mulders and R. D. Tangerman. "The complete tree-level result up to order $1/Q$ for polarized deep-inelastic leptoproduction." *Nucl. Phys.* B461, 197-237 (1996). Erratum ibid. B484:538-540, 1997.

[58] J. Collins, *Nucl. Phys.B396 (1993) 161*

[59] [HERMES Collaboration],

[60] J.P. Ralston and D.E. Soper, *Nucl. Phys.B152 (1979) 109*

[61] F. Baldracchini et al., *Fortsch. Phys. 30 (1981) 505*

[62] X. Artru and M. Mekh, *Nucl. Phys. A532 (1991) 351*

[63] R.A. Kunne et al., "Electroproduction of polarized Lambdas" Saclay CEN -LNS-Ph-93-01.

[64] M. Anselmino, "Transversity and Lambda polarization" *proc. of the Work-shop on Future Physics @ COMPASS.* Sept. 26-27, 2002, CERN.

[65] J. Ellis, D. Kharzeev, and A. Kotzinian, Z. Phys. C69 (1996), 467

[66] W. Lu and B. Ma, Phys. Lett. B

[67] M. Anselmino et al., Phys. Lett. B 481 (2000), 253.

[68] R.L. Jaffe, "Polarised Lambdas in the Current Fragmentation Region", Phys. Rev. D 54, 1996

[69] A. Abragam and M. Goldman. "Principles of dynamic nuclear polarisation." Rep. Prog. Phys. 41, 395-467 (1978).

[70] G. K. Mallot. "The spin structure of the nucleon from the SMC Experiments." Habilitationsschrift, Johannes Gutenberg Universitt Mainz, 1996.

[71] N. Takabayashi. "Polarized target for the measurement of the gluon contribution to the nucleon spin in the COMPASS exeriment." Ph.D. thesis, Nagoya University, 2002.

[72] B. Q. Ma, I. Schmidt, J. Soffer and J. J. Yang, Phys. Rev. D **64** (2001) 014017 [Erratum-ibid. D **64** (2001) 099901] [arXiv:hep-ph/0103136].

[73] G.Alexeev, O.Denisov and A.Maggiora, COMPASS note 2002-10.

[74] F. Gonnella and M. Pegoraro "A prototype front-end asic for the read-out of the drift tubes of CMS barrel muon chambers," *fourth workshop on electronics for LHC experiments - LEB98, Rome, 21-25 September 1988*, CERN/LHCC/98-36 pp. 257.

[75] G. Braun, et al. "F1 - an eight channel Time-to-Digital Converter chip for high rate experiments," *PROCEEDINGS of the 5th workshop on electronics for LHC experiments - LEB99, Snowmass, 20-24 September 1999*, CERN/LHCC/99-33.

[76] O.Denisov, S.V.Donskov, A.Ferrero, G.Khaustov, D.Panzieri, COMPASS note 2005-10.

[77] E.Iarocci, Nucl.Instr. and Meth.217 (1983) 30.

[78] Abazov V.M. et al. "Test stands for MDTs." *JINR preprint,P13-2003-198.* Dubna, 2003. (in Russian); also: Instruments and Experimental Technics, vol. 50, no. 1, 47-57, 2007 (in English)

[79] Abazov V.M. et al. "The test results of Mini-Drift Tubes for the Forward Angle Muon System of D0 setup." *JINR preprint,P13-2004-155.* Dubna, 2004. (in Russian); also: Instruments and Experimental Technics, vol. 50, no. 1, 58-68, 2007 (in English)